APPLICATION OF SYNCHROTRON-BASED SPECTROSCOPIC TECHNIQUES XAS AND XFM TOWARDS PROBING THE CELLULAR METALLOME

Jason L. Wedding

School of Physical Sciences

The University of Adelaide

A thesis for the degree of Doctor of Philosophy submitted to

The University of Adelaide

February 2019

Supervised by Professor Hugh H. Harris

THE UNIVERSITY of ADELAIDE

DECLARATION

I certify that this work contains no material which has been accepted for the award of any other degree or diploma in my name, in any university or other tertiary institution and, to the best of my knowledge and belief, contains no material previously published or written by another person, except where due reference has been made in the text. In addition, I certify that no part of this work will, in the future, be used in a submission in my name, for any other degree or diploma in any university or other tertiary institution without the prior approval of the University of Adelaide and where applicable, any partner institution responsible for the joint-award of this degree.

I acknowledge that copyright of published works contained within this thesis resides with the copyright holder(s) of those works.

I also give permission for the digital version of my thesis to be made available on the web, via the University's digital research repository, the Library Search and also through web search engines, unless permission has been granted by the University to restrict access for a period of time.

I acknowledge the support I have received for my research through the provision of an Australian Government Research Training Program Scholarship.

Jason Wedding, 8 February 2019

ACKNOWLEDGEMENTS

Firstly, I cannot show enough gratitude towards Professor Hugh Harris; who not only let me explore synchrotron science which was the blend of physics, chemistry and biology I was looking for but also has been extremely patient throughout the last 8 years. Hugh provided me with not only the guidance and support when my thesis was forced to change direction, but also the time and space I needed in the last couple of years to process what was happening in my life. The turmoil that resulted from numerous personal upheavals meant continued delays and throughout all of this Hugh never lost his patience nor his belief that I would reach this point of completion.

I am grateful to Dr. Ian Musgrave for sharing with me his laboratory as well as the art of cell culture. Without this access and knowledge, none of this research would have come to fruition. Furthermore, the support of many beamline scientists in beamline set-up, data collection and subsequent analysis has been vital to this work and I thank Dr. Stefan Vogt and Barry Lai for sharing their time, skills and knowledge.

I am extremely thankful to the other PhD students I had the pleasure of working alongside, or simply shared an office with, Claire Weekley, Melanie Ceko and Kelly Keeling. Claire's friendly assistance, regardless of how out of the blue my requests came, allowed me to continually learn new skills and stay sane during the long synchrotron trips (especially the trip where not a single sample was analysed). Melanie's presence changed the whole dynamic of the Harris group, bringing an enthusiasm and passion that was truly infectious. Finally Kelly, who was not a part of the Harris group, but was always willing to help me out, be it with access to laboratories or charitably listening to my woes while ever staying positive.

I would also be amiss if not to thank Associate Professor Tara Pukala who acted as my yearly guidance councillor throughout my PhD. Always ready to listen, provide assistance as well as the reassurance that things would work out if I persisted. These words of support, while infrequent, were incredibly helpful in choosing to stay the course and finish this thesis.

Lastly, but perhaps most importantly, I have to thank my family. My parents never failed to encourage me to "just get it done", and it's a certainty that without their support finishing this would never have been a possibility. My sister Nyssa, who has

been my constant companion during my PhD period and whose presence alone has kept me going during the harder times.

I dedicate this thesis to my late grandfather Dean Trowse, who along with my grandmother Rhonda Trowse, were extremely proud of my efforts but unable to be here for its completion. Poppa Deano never once lost faith that this thesis would be completed, would have desperately wanted his own copy, and would have insisted the whole family celebrate the occasion.

TABLE OF CONTENTS

Title Page .....

Declaration ..... **ii**

Acknowledgements ..... **iii**

Table of Contents ..... **v**

Thesis Abstract ..... **x**

Linkage Between Chapters ..... **xii**

Chapter 1. The advantageous use of synchrotron-based techniques, XAS and XFM, in exploring the cellular metallome **1**

1.1 Abstract 2

1.2 Abbreviations 3

1.3 Introduction 4

1.3.1 Synchrotron Facilities – Brief History and Basic Principles 4

1.3.2 Metallomics – Metal Ion Metabolism 5

1.3.2.1 The Metallomics Image Problem 7

1.3.2.2 Sample Preparations 7

1.3.2.3 Technique-introduced Bias 8

1.3.3 A Synchrotron-based Solution 8

1.3.3.1 Principles of XAS 10

1.3.3.2 Principles of XFM 12

1.3.4 Experimental Aims 14

1.4 References 16

Chapter 2. Intracellular distribution and stability of a luminescent rhenium(I) tricarbonyl tetrazolato complex using epifluorescence microscopy in conjunction with X-ray fluorescence imaging **20**

Statements of Authorship 21

Journal Edition Cover 25

Introduction 26

Experimental 27

Synthesis and characterisation 27

Photophysical measurements 28

Cell culture 28

Preparation of Re-I treatment solutions 28

Cell treatment sample preparations 28

Spectroscopic data collection 28

XFM imaging data analysis 28

Results 29

Conclusions 32

Acknowledgements 32

References 32

Chapter 3. Investigation into the intracellular fates, speciation and mode of action of selenium-containing stroke mitigation agents **35**

Statements of Authorship 36

3.1 Abstract 38

3.2 Abbreviations 39

3.3 Introduction 40

3.3.1 Ischaemia 40

3.3.2 Antioxidant defences 41

3.3.3 Therapeutic antioxidants 41

3.3.4 Ebselen 42

3.3.5 Diphenyl diselenide 43

3.3.6 Experimental Aims 43

3.3.7 Synchrotron Techniques 44

3.3.7.1 X-ray absorption spectroscopy 44
3.3.7.2 X-ray fluorescence microscopy 45
3.4 Materials & Methodology 47
3.4.1 Materials 47
3.4.2 Cell culture 47
3.4.3 Treatment solutions 47
3.4.4 Cell fixation solutions 47
3.4.5 Cytotoxicity assays 48
3.4.5.1 Drug alone studies 48
3.4.5.2 Oxidative stress condition studies 48
3.4.6 Sample preparation 49
3.4.7 XAS data collection 49
3.4.8 XAS data analysis 50
3.4.9 XFM data collection 50
3.4.10 XFM data analysis 51
3.5 Results & Discussion 52
3.5.1 Cytotoxicity studies 52
3.5.1.1 Drug alone cytotoxicity studies 52
3.5.1.2 Oxidative Stress Condition Studies 53
3.5.2 Synchrotron Based Studies 57
3.5.2.1 Bis(2-nitrophenyl)diselenide XAS Studies 57
3.5.2.1.1 Bis(2-nitrophenyl)diselenide XANES Studies 57
3.5.2.1.2 Bis(2-nitrophenyl)diselenide EXAFS Studies 61
3.5.2.2 Bis(2-aminophenyl)diseleinde XAS studies 67
3.5.2.2.1 Bis(2-aminophenyl)diselenide XANES Studies 67
3.5.2.2.2 Bis(2-aminophenyl)diselenide EXAFS Studies 69

3.5.2.3 Ebselen XAS Studies 73

3.5.2.3.1 Ebselen XANES Studies 73

3.5.2.3.2 Ebselen EXAFS Studies 77

3.5.2.4 X-Ray Fluorescence Microscopy Studies 79

3.6 Conclusions and Future Directions 89

3.6.1 Conclusions 89

3.6.2 Future Directions 90

3.7 Acknowledgements 92

3.8 References 93

Chapter 4. Fluorescence and XFM studies into the anticancer mode of action of the ruthenium-based anti-cancer agent NKP-1339 within A549 human lung adenocarcinoma epithelial cells **99**

4.1 Abstract 100

4.2 Abbreviations 101

4.3 Introduction 102

4.3.1 Cisplatin 102

4.3.2 Ruthenium-based anticancer alternatives 103

4.3.3 NKP-1339 106

4.3.4 Experimental aims 106

4.4 Materials & Methodology 108

4.4.1 Materials 108

4.4.1.1 Cell culture solutions and reagents 108

4.4.1.2 NKP-1339 treatment solutions 108

4.4.1.3 MitoTracker fluorescence probes treatment solutions 108

4.4.1.4 Cell fixation solutions 109

4.4.2 Methodology 109

4.4.2.1 Cell Culture 109

4.4.2.2 X-ray fluorescence imaging of unlabelled single cells (Advanced Photon Source) 109
4.4.2.2.1 Sample Preparation 109
4.4.2.2.2 Data Collection 109
4.4.2.2.3 Data Analysis 110
4.4.2.3 X-ray fluorescence imaging of fluorescence-labelled single cells (Advanced Photon Source) 110
4.4.2.3.1 Sample Preparation 110
4.4.2.3.2 Data Collection 111
4.4.2.3.2.1 Fluorescence-Probe Labelled Imaging 111
4.4.2.3.2.2 X-ray Fluorescence Imaging 111
4.4.2.3.3 Data Analysis 112
4.4.2.3.3.1 X-ray Fluorescence Image Analysis 112
4.5 Results & Discussion 113
4.5.1 NKP-1339 Exploratory Study 113
4.5.2 NKP-1339 Experiments with Organelle Staining 120
4.6 Conclusions and Future Directions 131
4.7 Acknowledgments 132
4.8 References 133
Chapter 5. Summary of outcomes and future directions **139**
Appendix I – Other Publications **AI-1**

THESIS ABSTRACT

The use of synchrotron-based experimental techniques has gained increasing recognition, as they are powerful tools to explore the cellular metallome. Metallomics, which encompasses all aspects of biological systems, especially the cell, involved in metal speciation and metabolism; and probes the spatial metal ion distributions within differing cell types, organelles and regulating proteins. As such, the precise imaging of metal ion and intracellular organelle distribution within the wider context of cellular regulation pathways and biological function is essential.

Biological systems are inherently complex, with the metal of interest being contained within an intricate biological matrix. Synchrotron-based techniques have benefits that laboratory-based fluorescence experiments do not; reduced required sample preparation, direct metal distribution imaging, and the ability to characterise the chemical nature of the intracellular metal pool.

This thesis describes the use of two synchrotron-based techniques; X-ray absorption spectroscopy (XAS) and X-ray fluorescence microscopy (XFM), to investigate the effects of biometal-based agents on the intracellular metallome.

Firstly, the intracellular fate of a luminescent rhenium(I) tricarbonyl tetrazolato complex probe within 22Rv1 human prostate epithelial carcinoma cells was explored. It was demonstrated that the cellular distribution of the luminescent imaging agent could be determined by monitoring the luminescence from the compound using optical microscopy and then correlated with the cellular distributions of rhenium and iodine contained in the species within the same samples as measured using micro-probe XFM.

A combination of XAS and XFM was employed to investigate the neuroprotective action purported for diphenyl diselenide. This was achieved by treating SH-SY5Y human neurocarcinoma epithelial cells with more water soluble diphenyl diselenide analogues; bis(2-aminodiphenyl)diselenide and bis(2-nitrodiphenyl)diselenide.

These two studies showcased that the advantageous, simultaneous collection of metallome and mode of action information can provide a pathway to exploring neurological diseases and disorders, the production of better therapeutic agents, and could be used diagnostically in medicine.

Finally, the anticancer action of NKP-1339, a KP1019 analogue, within A549 human lung adenocarcinoma epithelial cells was investigated. Initially a co-localisation of NKP-1339, or its ruthenium-containing metabolites, with intracellular iron and copper was observed. Subsequent attempts to visualise a mitochondrial compartmentalisation of the NKP-1339 or its ruthenium-based metabolites utilising a combination of optical and synchrotron-based fluorescence microscopy were unsuccessful.

The studies into the Re-I probe and diphenyl diselenide analogues showcased the power of synchrotron-based spectroscopic techniques yielding mode-of-action information as well as visualising the effects of the biometal-containing agents on the intracellular metallome. The study into NKP-1339, while largely unsuccessful, did provide similar information related to the perturbation of the intracellular metallome while not yielding mode-of-action information.

LINKAGE BETWEEN CHAPTERS

This thesis of 5 chapters is comprised of 4 manuscripts and 1 journal article. The manuscripts form the introduction (Chapter 1), two of the experimental sections (Chapters 3 and 4) and a final conclusion section (Chapter 5). Chapter 2 is presented as a published journal article. The work of Chapter 3 has also been published in a peer-reviewed, international journal. Due to the nature of the results for the studies that are presented in Chapter 4, there is no plan to pursue publication. The manuscripts are listed at the end of this section.

The introductory chapter consists of a review of synchrotron-based techniques and their application into probing the intracellular metallome. This section aims to provide a broad context towards the importance of a greater understanding of the metallome and how synchrotron-based techniques are a powerful tool well placed to achieve this aim. This chapter also aims to introduce and provide a basis for the subsequent experimental sections and their aims.

In Chapters 2-4, the results of synchrotron-based studies into a luminescent rhenium(I) tricarbonyl tetrazolato complex probe, selenium-containing stroke mitigation agent and ruthenium-based anticancer agent's effects on the intracellular metallome in addition to mode-of-action information are presented.

Chapter 2 showcases the use of X-ray fluorescence microscopy (XFM) in conjunction with laboratory-based fluorescence techniques to investigate the cellular fate of the luminescent probe as well as the impacts the probe has on the intracellular metallome. As stated above, Chapter 2 is presented as the paper appears in the peer-reviewed journal *Metallomics*. Included is the journal edition cover, which was designed by the candidate at the request of the journal.

Chapter 3 employs XFM along with X-ray absorption spectroscopy (XAS) to investigate the stroke-mitigation action of water-soluble diphenyl diselenide analogues. The results, aided by comparison to known stroke-mitigation agent Ebselen, indicated that the nuclear penetration (XFM data) and changes in chemical speciation (XAS data) had a large bearing on the afforded protective action. Despite being published prior to thesis submission, the original, complete, non-truncated version of the research is presented in this thesis.

Chapter 4 presents the use of XFM in conjunction with laboratory-based fluorescence techniques to investigate the mode-of-action of a ruthenium-based anticancer agent. Whilst mode-of-action information was not obtained, the resulting changes to the intracellular metallome from treatment were visualised.

Chapter 5 closes the main body of the thesis aiming to draw together the results from the three experimental chapters within the broader context presented in the introduction section.

Appendix I finally presents a published work that the candidate assisted with, which while related to the research presented within Chapter 3 did not fit within the context of this thesis.

Below is the list of manuscripts that constitute Chapters 2, 3 and Appendix I of this thesis:

J. L. Wedding, H. H. Harris, C. A. Bader, S. E. Plush, R. Mak, M. Massi, D. A. Brooks, B. Lai, S. Vogt, M. V. Werrett, P. V. Simpson, B. W. Skelton and S. Stagni (2017) Intracellular distribution and stability of a luminescent rhenium(I) tricarbonyl tetrazolato complex using epifluorescence microscopy in conjunction with X-ray fluorescence imaging, *Metallomics*, 9 (4) 382-390.

J. L. Wedding, B. Lai, S. Vogt, H. H. Harris (2018) Investigation into the intracellular fates, speciation and mode of action of selenium-containing neuroprotective agents using XAS and XFM, *Biochim. Biophys. Acta*, 1862 (11) 2393-2404.

M. Sooriyaarachchi, **J. L. Wedding**, H. H. Harris, J. Gailer (2014) Simultaneous observation of the metabolism of cisplatin and NAMI-A in human plasma in vitro by SEC-ICP-AES, *J. Bio. Inorg. Chem.*, 19 (6) 1049–1053.

CHAPTER 1. The advantageous use of synchrotron-based techniques, XAS and XFM, in exploring the cellular metallome

Jason Wedding and Hugh Harris*

*School of Physical Sciences, The University of Adelaide, SA, 5005, Australia

1.1 Abstract

The use of synchrotron-based experimental techniques, such as X-ray absorption spectroscopy and X-ray fluorescence microscopy, has gained increasing recognition as powerful tools to explore the cellular metallome. Biological systems are inherently complex, with the metal of interest being contained within an intricate biological matrix. Furthermore, biometals are tightly regulated within cells and compartmentalised within organelles, producing “pools” of the same metal that can function differently from one another. Synchrotron-based techniques have the benefits that laboratory-based fluorescence experiments do not; reduced required sample preparation, direct metal distribution imaging, and can characterise the chemical nature of the intracellular metal pool. As such synchrotron-based techniques provide a pathway to exploring neurological diseases, the production of better anti-cancer drugs, and can be used diagnostically in medicine.

1.2 Abbreviations

EXAFS	Extended X-ray absorption fine structure;
HPLC	High performance liquid chromatography;
ICP-MS	Inductively coupled plasma mass spectrometry;
Linac	Linear (particle) accelerator;
XANES	X-ray absorption near-edge structure;
XAS	X-ray absorption spectroscopy;
XFM	X-ray fluorescence microscopy;
SH-SY5Y	Human bone marrow epithelial neuroblastoma cells;
22Rv1	Human prostate epithelial carcinoma cells.

1.3 Introduction

1.3.1 Synchrotron Facilities – Brief History and Basic Principles

The synchrotron-based X-ray techniques, XAS (X-ray absorption spectroscopy) and XFM (X-ray fluorescence microscopy), allow for chemical speciation and elemental distribution to be investigated with relatively less sample preparation than their more common, laboratory based counterparts (e.g. ICP-MS). The development of the principles behind synchrotron science is uniquely credited to both Vladimir Veksler and Edwin McMillian, but independently. Veksler published the theory behind synchrotron operations in 1944[1], with McMillian constructing the first synchrotron in 1945 without the aid of Veksler's paper[2,3].

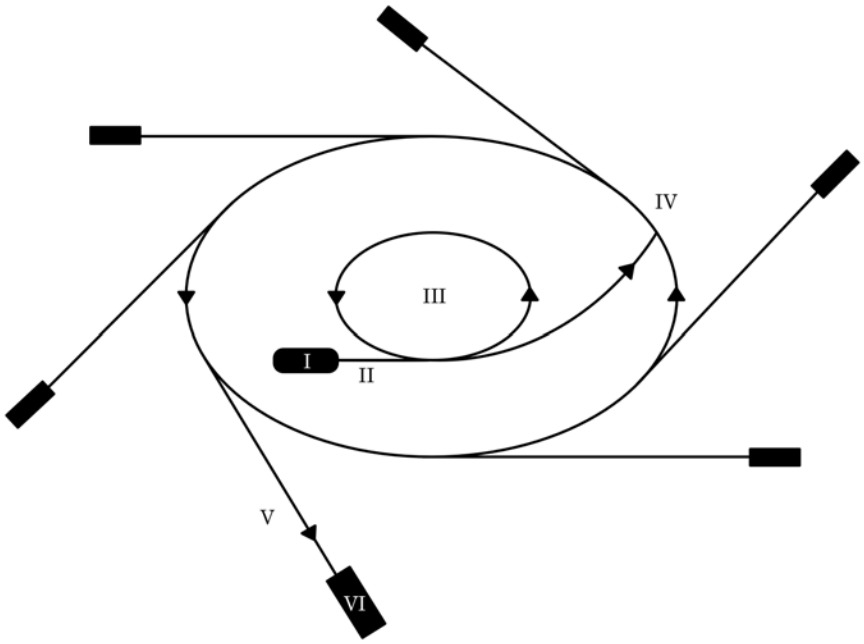

Figure 1.1 – Schematic of a synchrotron highlighting its main features of (I) electron generation by thermionic emission with subsequent electrons being rapidly accelerated over a short distance in a linac (II) before entering the booster ring (III) at near the speed of light. After spending only half a second and completing over a million laps the electrons then enter the storage ring (IV). Beamlines (V) are positioned to catch the tangential synchrotron radiation given off by the storage ring, with experiments utilising the radiation occurring in custom hutches (VI) that are optimised for the particular type of experiments.

Synchrotrons (Figure 1.1) are large particle accelerators that use a narrow ring of magnets in an elliptical arrangement, which are interrupted by gaps where a high voltage electric field accelerates the charged particles. Particles are injected with considerable initial energy from a

smaller accelerator ring (booster ring), into a larger storage ring where they move in a circle of constant radius at 99.9997% the speed of light. The forced acceleration of the particles (typically electrons) within a strong magnetic field produces electromagnetic radiation with special properties to be radiated at high intensity and within a narrow cone tangentially to the circular path, and is termed synchrotron radiation.[4-7]

Synchrotron radiation, while initially regarded as an unwanted bi-product of the particle acceleration experiments was quickly recognised for its unique properties and synchrotrons began to optimise their structure around the production and collection of this radiation.[4,5,7] Modern synchrotrons use insertion devices (wigglers and undulators) to significantly increase the intensity of the light produced by increasing the acceleration that the particles experience.[5,7] Synchrotron radiation has high brightness due to its high intensity and collimated nature, can be generated and tuned across a wide range of the electromagnetic spectrum (IR to hard X-rays), is highly polarised, and can be emitted in extremely short pulses (typically less than a nano-second) enabling time-resolved studies.[5-8]

Applications of synchrotron radiation bridge a wide range of scientific areas, from biosciences (protein crystallography and cell biology)[9-12], medical research (microbiology, cancer cell radiation therapy and high resolution imaging)[13-16], environmental sciences (atmospheric research and toxicology) [17-22], and agriculture (plant genomics, soil studies and plant imaging)[18,23].[5,6,18,24,25]

Within the field of bioscience, the native low concentrations within samples are uniquely compensated for by the high intensity and sensitivity.[18,24] This has allowed for the determination of accurate bond lengths and active site geometrics by XAS, of particular import to understand reaction mechanisms.[24] It has provided information when crystallography was not available (e.g. in solution enzyme catalysis), as well as additional information when crystallography was available (found a missed Se-S interaction within Escherichia coli formate dehydrogenase H).[24]

1.3.2 Metallomics – Metal Ion Metabolism

Metallomics, which encompasses all aspects of biological systems, especially the cell, involved in metal speciation and metabolism; and probes the spatial metal ion distributions within differing cell types, organelles and regulating proteins. As such the precise imaging of metal ion and intracellular organelle distribution within the wider context of cellular regulation pathways and biological function is essential.[26-28]

All life has evolved to capitalise on the unique chemical characteristics of metal ions to carry out varied functions not available to non-metals.[26,29-33] It is estimated that one third of proteins interact with metal ions, and half of enzymes require metal ions to function. Biometal cofactors act in numerous ways; such as stabilising protein structures (Zn finger proteins), aiding in catalytic activity (cytochrome P450), as well as in cell signalling pathways. Furthermore, free metal ions have been linked to the regulation of resting and action potentials, neurotransmission activity, osmotic potentials and biological pH regulation.[26,34,35] Due to the wide-ranging effects that biometals exert, biometal metabolism is a viable therapeutic target within various disease states.[36-38]

The investigation of metallomics is hindered by the inherent complexity of biological systems and accompanied unpredictably of biological processes that make accurate measurements difficult. Ideal experimentation involves the measurement of a stable analyte that does not undergo chemical changes during the associated preparation steps as well as the during the measurement window itself. However, metallomics involves the study of metal ions which is complicated by; metal ions exhibiting multiple roles, in vitro evidence of metal ion-protein interactions not necessarily indicating primary function, some metal ion-protein interactions being transient, and changes in cellular distributions of metal ions being indicative of changes in activity without an overall net change in metal ion level (such as mobilisation of metal ions from storage proteins allowing for indiscriminate reactivity as labile ions).[26,39-41]

The biometal pool is under tight control within the cell, with cofactors carefully chaperoning ions through the cell by a network of ligands, due to the potential of metal ions to cause injury due to unregulated activity, or activity at the incorrect time or in the wrong intracellular location.[42,43] This fine balance provides opportunities for pathological processes to perturb the biometal homeostasis leading to disease states, but also means the balance is easily disturbed by attempts to monitor it.[44-46]

Probing the intricacies of metal ion metabolism is important due to its major implications for greater understanding of not only basic biology, but also for informing and improving clinical practices and biotech-based solutions. As such, direct in vivo imaging of these systems with minimal and careful sample preparations would provide the most powerful and accurate insights into metal ion metabolism.[26,47]

1.3.2.1 The Metallomics Image Problem

Tools well suited for exploring metallomics need to be able to image the multiple forms of a given metal across a range of biochemistry, physiology and pathology processes. Traditional tools involve investigating single isolated metal bound species (e.g. crystallography, various spectroscopies of purified metalloproteins), or they examine the entire biometal pool without differentiating the chemical forms (ICP-MS of tissues).

Furthermore, traditional laboratory-based tools are frequently destructive, especially in regards to the hyphenated chromatography-spectroscopies, e.g. the sample is destroyed during measurement during ICP-MS. This limits the ability to corroborate results, control the risks associated with sample preparations and the measurement technique itself altering the biometal chemical speciation.

While current technology provides adequate sensing to detect physiological concentrations and distributions of the most common biologically relevant metal ions, e.g. Ca, Zn, Fe. These native metal ions and their metabolism and regulation are highly susceptible to extrinsic factors that can perturb how the total biometal is distributed. Biometal homeostasis is dynamic and so capturing an unbiased snapshot is an analytical challenge. Issues arise as to whether the produced images are true depictions of physiological biometal metabolism, or merely a depiction of the effects of external perturbations introduced by the measuring techniques and required sample preparations.[26]

1.3.2.2 Sample Preparations

The ability of metal ions to form dyes visible to the naked eye has been a useful characteristic traditionally utilised to profile spatial distributions.[26,47] While useful in a clinical setting, this approach has limited utility in use as a research tool for assessing true quantitative distributions and spatial coordination of biometals in a native state.[26] The chemical processing required for the visualisation (e.g. staining) exerts some influence on the biometal levels.

Samples are typically immersed in a fixation solution, such as formaldehyde, dehydrated with alcohol and xylene, sectioned, all before being placed in a cover-slipped glycerol medium. This affords ample opportunity for labile metal ions to be lost or introduced into the sample environment. Moreover, the nature of the stain may also alter the metal ion within the sample, either through binding directly or causing re-distribution and resultant speciation changes.[26] Other techniques, such as atomic absorption spectroscopy or inductively-coupled plasma

mass spectrometry, require homogenisation and chemical digestion prior to analysis. These provide valuable information but cannot reveal the spatial distribution of biometals within the sample, as well as requiring the isolation and detection of discrete species.

Currently accepted preparative treatments have been found to have the potential to exert a marked impact on total biometal levels, speciation and distribution on the μ-scale.[48] FT-IR on brain sections with and without formalin staining elucidated significant effects on the organic composition and exposed biometal redistribution and influx.[49] The use of synchrotron-based techniques XFM and PIXE, proton induced X-ray emission, has provided quantitative assessment of various fixative techniques with the conclusion being that the effects on concentrations and distributions of biometals vary depending on the chemical treatment employed.[50,51] Synchrotron-based studies can limit sample preparation to freeze-drying hydrated samples, which avoids chemical modification of the target metal ion prior to analysis.

1.3.2.3 Technique-introduced Bias

The most common biometal sensor design is utilising a fluorophore that generates a measurable signal, or change in signal, upon binding to the target metal ion. The fluorophore by definition disturbs the biological system, and in turn affects the distribution and concentration of the target metal ion. This issue is most prevalent when dealing with biological systems where there exists a labile metal ion pool, where the binding of metal ions to the sensor can induce unintended transfer of protein-bound metal ions to the sensor, or movement between different intracellular locations.[26]

These concerns are currently minimised by designing the probe to have sufficient brightness and sensitivity such that they can operate at extremely low treatment concentrations[52], or by using reaction-based probes that do not directly bind the target metal ion[53]. It is however, impossible to completely eliminate sensor interference, and is important instead to understand the detection protocol's effects on the metallome distribution and speciation changes. It is only by measurement of other parameters, such as cell viability, mitochondrial function or reactive oxygen species (ROS) levels, that a sensor can be confirmed to have no or minimal unwanted effects.[26]

1.3.3 A Synchrotron-based Solution

Synchrotron science affords the ability to conduct holistic, multimodal studies of a sample's intact, cellular metallome, thereby providing a pathway to better research a myriad of topics;

producing better anticancer drugs[54,55], probe neurological disease states[37], as well as provide better diagnostic imaging[56]. These types of techniques provide direct and simultaneous imaging of multiple chemical forms with cellular resolution at intact cells, tissues and organism levels.

Cellular processes involving biometals are directed by complex metal chemistry at an atomic and molecular scale; X-rays can provide information pertaining to local coordination geometry as well as the chemical states of species at a subcellular level.[8] This unique ability to detect speciation, which is crucial to understanding the chemistry of biometals in cellular processes, makes synchrotron-based experimentation tools particularly powerful in the elucidation of the roles and function of biometals at a cellular level.[8]

X-ray fluorescence microscopy facilitates the localisation and quantification of elements in cells and tissues, and is commonly used in conjunction with X-ray absorption spectroscopy. X-ray absorption spectroscopy can add speciation information; such as the chemical or oxidation state and the local coordination geometry of the probed element. Together these two techniques allow for the in situ imaging of, and information gathering on, biometals within a range of sample types.[8]

Synchrotron-based X-ray microscopy has a spatial resolution down to the tens of nanometres without the need of invasive procedures such as labelling, dehydration, nor chemical fixation, which alter the endogenous biometal chemistry. This ability to obtain subcellular resolution is especially important as biometal homeostasis involves tight regulation of biometal-containing species through subcellular compartmentalisation. For example, Fe-S clusters and heme synthesis products are kept in the mitochondria, Zn-finger proteins are found in the nucleus and Cu is regulated within the Golgi apparatus.[8,57,58]

Synchrotron-based tools for exploring metallomics are not without their own drawbacks. Due to the nature of the high intensity radiation employed there is always the risk of radiation-induced damage, which has been also shown to perturb biochemical activity and alters speciation and distribution of biometals.[59] This risk is managed by cryogenic preservation, which involves the combination of cryo-cooling, vacuum chambers, and more recently streaming liquid nitrogen onto samples at atmospheric pressure. As such, synchrotron-based techniques are developing into a “standard” for exploring undisturbed cellular systems, especially with the ability to image larger standards including fully hydrated room temperature tissue samples.[26]

1.3.3.1 Principles of XAS

X-ray absorption spectroscopy, or XAS, involves the absorption of x-rays by core electrons (e.g. 1s), followed by either promotion to a higher bound state (termed the edge region, e.g. 1s to 3d or 1s to 4p), or the core electron is ejected as a photoelectron (termed the extended X-ray fine structure region). When neighbouring atoms are present the emitted photoelectron will be backscattered off these nearby atoms and produce interference between the outgoing and backscatter waves producing EXAFS modulations.

Practically, a spectrum is produced by scanning across an energy range both above and below the absorption edge of the probed element (Figure 1.2). The X-ray near-edge structure is collected within 100 eV of the absorption edge, with the core electron being ejected and thus producing the EXAFS at a higher level.[13,60,61] Due to the intrinsically low concentrations of the probed element within the samples fluorescent photons are collected. These fluorescent photons are emitted as lower energy photons, which result from bound electrons falling to fill the core hole left by the ejected core electron.[24] X-ray absorption spectra represent the bulk coordination environment and oxidation of the probed element of interest, including contributions from all chemical forms containing the element within the sample.[6]

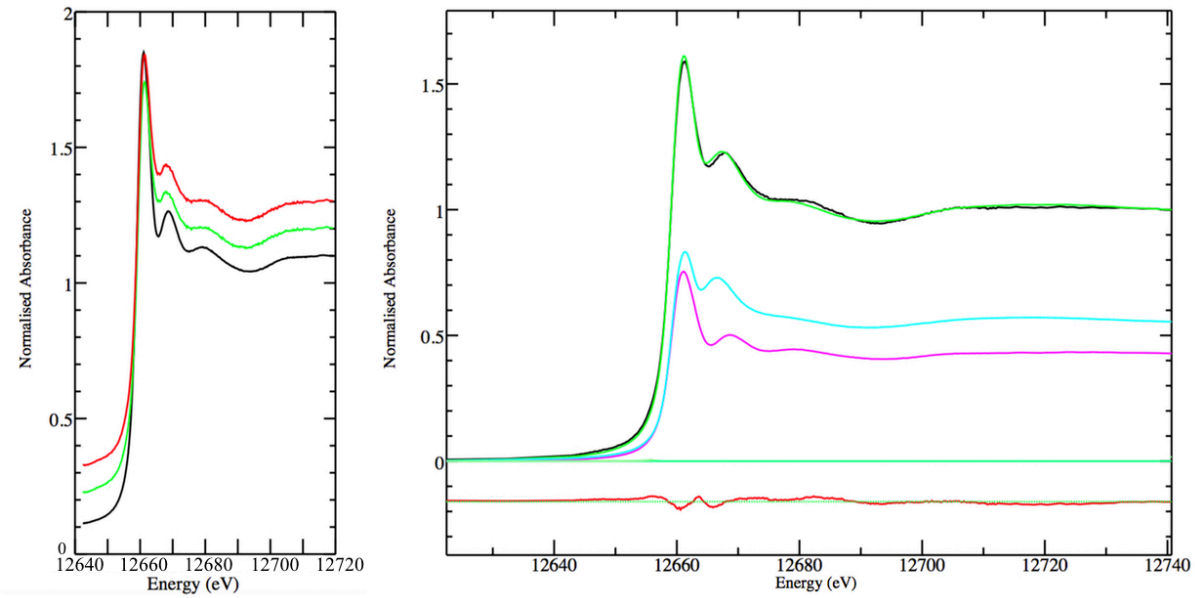

Figure 1.2 – Left: The selenium near-edge (XANES) region of bulk cell pellets treated with a selenium-based agent. Right: Fitted XANES spectra for a bulk cell pellet treated with a selenium-based agent. The experimental spectrum is in black, while the resultant fit of two Se-model compound spectra (pink and light blue) is shown in dark green. The residual, or difference between the experimental and fitted data is shown in red.

XAS near-edge structure can provide important information on electronic structure, such as the element's oxidation state, spin state, direct determination of metals in the active site (which is only implied by crystallography) in macromolecules. The EXAFS, however, provides the primary structural determination tool. From fitting of the EXAFS very accurate bond lengths can be obtained (~0.002 Å), which is superior to protein crystallography by an order of magnitude. However, it is a very short ranged technique, with covalently bound atoms being able to be observed but not distant atoms (>5 Å). Furthermore EXAFS has limited bond length resolution (~0.1 Å) in discriminating between similarly coordinated atoms, is not effective with the determination of coordination numbers (~20%), and cannot accurately differentiate between backscattering atoms of similar size (e.g. S, Cl).[6,24]

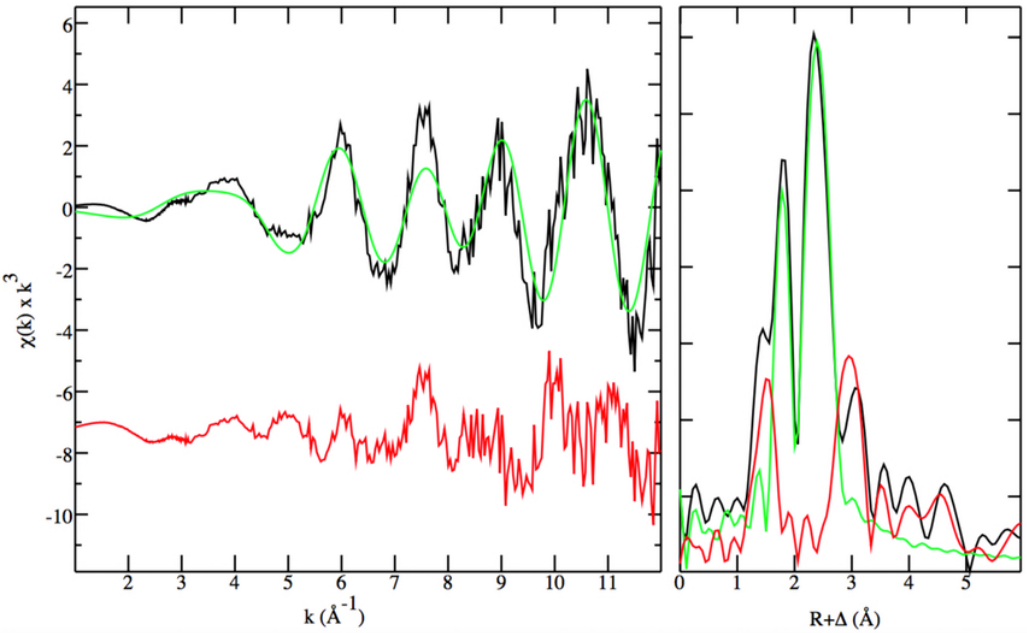

Figure 1.3– EXAFS spectra and corresponding Fourier transforms of cells treated with a selenium-based agent, showing experimental (black) and calculated (green) data, with the residual shown offset (red). The Fourier Transform fitting indicating two dominant back-scattering neighbouring atoms.

A single XAS scan contains both the XANES and EXAFS regions, and so through independent analysis results can be combined to more confidently assess the speciation and structure of the element of interest. Furthermore, relatively short scan times allows for multiple scans of the same sample (at differing spots on the sample) to lessen photo-reduction effects and noise within the EXAFS region. The resultant XANES spectra are fit with linear combinations of model compound spectra, while EXAFS are analysed a priori with the tentative XANES findings acting as the starting point to the EXAFS analysis.

XAS excels in investigation into biometals where not only the total metal distribution is important, but also the speciation of the biometals present. XAS can provide information on species which standard crystallography cannot, such as solution-based enzyme catalysis, or provide supplemental information for systems for which crystallography is available.[6,8,24] Utilising the principles of XAS as a microscopic technique provides opportunities for chemical mapping of metals down to the nano-scale, providing speciation and localisation information critical to understanding the mechanisms and roles of biometals in specific biological processes.[8]

1.3.3.2 Principles of XFM

Fluorescence, or secondary, photons used to create X-ray absorption spectra are also used as the foundation of XFM. Each element possesses an electronic structure with characteristic energy levels, XFM capitalises on these fingerprint-like electronics. Incident photons with enough energy above the ionisation threshold eject core electrons, much like XAS, these core holes are then subsequently filled by outer shell electrons resulting in the emission of lower energy fluorescence photons.

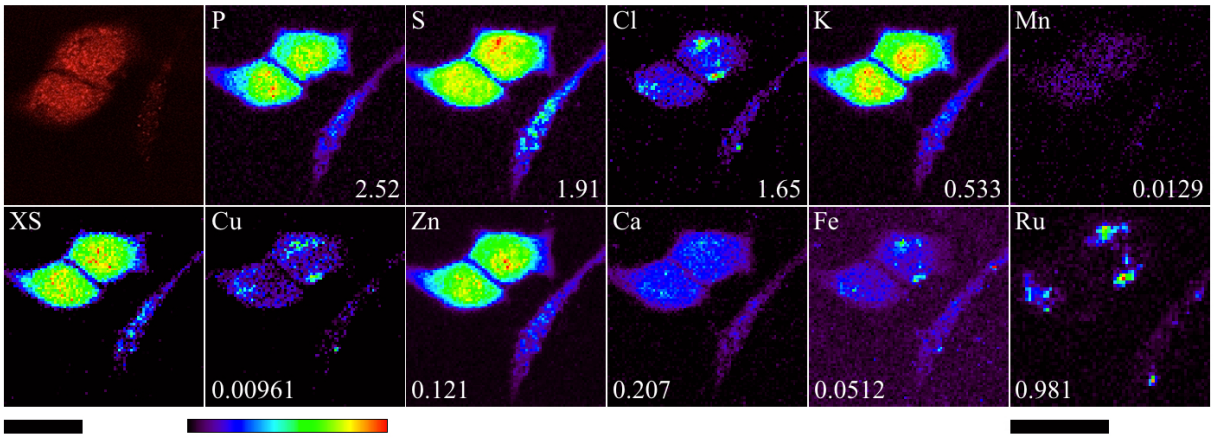

Figure 1.4 – Optical fluorescence image (top left), scattered X-ray (XS) and XFM elemental distribution maps of cells treated with a ruthenium-based agent. The maxima elemental area densities (quantified from standards and expressed in micrograms per square centimetre) are given in the bottom corner of each map. The black bar under the maps represents 10 µm.

Instead of scanning a range of energies through the sample such as with XAS, the energy is held constant and above the absorption edge for XFM, with the sample then moved through the beam to produce an elemental map based on the fluorescence at each point (Figure 1.4). Precision of the raster scanning process allows for imaging down to the cellular level, with the potential of sub-cellular organelle determination, such as the nucleus of cells that contain

high P and K concentrations. XFM has developed a reputation as the most versatile imaging technique for simultaneously obtaining structural and compositional information relating to biometals.[26]

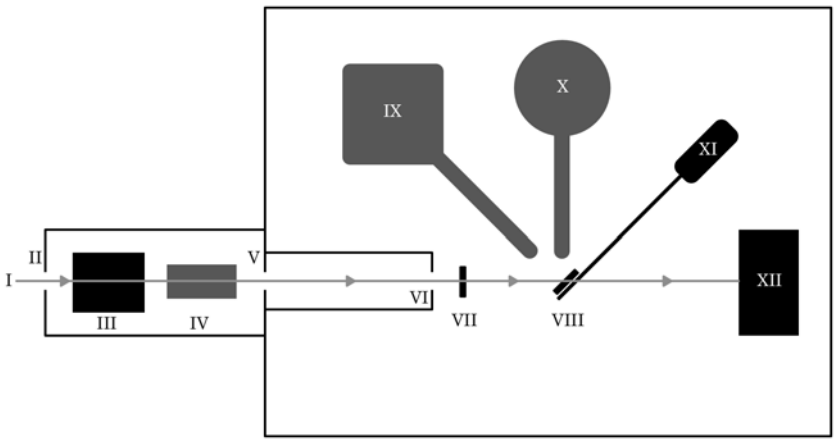

Figure 1.5 – Schematic of a XFM experimental hutch with the incident synchrotron beam (I) passing through the primary aperture (II) before the double crystal monochromators (III) and focusing mirrors (IV). The beam then passes into the experimental hutch through a secondary aperture (V), pinhole (VI) and the primary filter (VII) before reaching the sample (VIII) loaded onto a mechanised, moveable stage (XI). The location of the sample respective to the beam is monitored with a microscope (IX) and fluorescence photons collected by the detector (X), with the beam finally ending its path at the beam stop (XII).

XFM features primary and secondary apertures that define the incident beam, which along with double crystal monochromators and focusing mirrors direct the beam onto a specimen loaded onto an x-y-z digital stage (Figure 1.5). The X-ray detector is placed at 90° to the incident beam to capture the resultant fluorescence photons. The energy used to excite the element of interest will also excite elements with lower atomic numbers, thus elemental maps of these elements are simultaneously generated. Although sensitivity to lower atomic numbered elements is diminished with increasing incident energy. In addition to the mapping of individual elements, spatial relationships can be identified and then through comparison to elemental standards the concentrations of the elements can be determined.[5,6]

A number of metallomic questions have utilised both μ–XFM and nano-XFM; including the effects of non-essential metal detoxification on subcellular homeostasis of native biometals, biometal profiles in cellular processes and diseases, and cellular localisation of metal-containing drugs.[8] XAS and XFM have successfully been used in conjunction in the study of

metal and non-metals in wide ranging fields of biology. The speciation and distribution of mercury within the human brain following exposure was investigated by Korbas et. al.[62]. Similarly the speciation and distribution of selenium and copper within rat kidneys was investigated with XAS and XFM.[63] EXAFS[64] and XFM[12] have been used to investigate the mode of action of ruthenium-based anticancer agents within tumour-like settings. Even the effects of labile nanoparticles on homeostasis have been probed using XFM techniques.[65]

1.3.4 Experimental Aims

Given the increasing popularity of synchrotron-based XAS and XFM techniques within the field of bioinorganic chemistry[6,66] and their application towards elucidating intracellular speciation and distributions of elements heavier than Si, these two techniques were employed to probe into the cellular fates of selenium, rhenium and ruthenium due to directed drug exposure. Furthermore, these methods allow for the advantageous ability to directly detect the element-containing drugs and their metabolites within cells without excessive sample preparations typical of laboratory-based systems (such as HPLC).

Rhenium and ruthenium are two elements that are not naturally occurring within the human biological system. Furthermore selenium, while present within the body at extremely low-basal levels, has its role confined to being a component of only a relatively small number of discovered proteins that exists with diverse patterns of tissue distributions. Selenium is incorporated into proteins involved in antioxidant roles (glutathione peroxidase, GPx), redox regulation (thioredoxin reductase, TrxR), nuclear transcription (selenoprotein H, Sel H) and early muscle formation (selenoprotein N, Sel N).[63,67,68] As such, changes in selenium content composition and distribution following drug treatments would indicate perturbations of intracellular homeostasis.

As such any and all rhenium and ruthenium detected by XAS and XFM would directly correlate to drug and resulting metabolites from treatment with agents containing the respective elements. The use of controls along with the low native basal levels of selenium also allows for the monitoring of changes in selenium speciation and distributions resulting from selenium-containing agent treatments.

The use of XFM was thus employed to detect and monitor the uptake and sub-cellular compartmentalisation of a rhenium-based luminescent rhenium(I) tricarbonyl tetrazolato complex within 22Rv1 human prostate carcinoma cells. Similarly, XFM was used to probe the cellular fate of ruthenium-based anticancer agent NKP-1339 (a KP1019 analogue) within

A549 adenocarcinomic human alveolar basal epithelial cells. Finally, a combination of XAS and XFM was employed to probe the basis of diphenyl-diselenide's stroke mitigation action within SH-SY5Y human neurobalstoma cells.

1.4 References

(1) Veksler, V. *Comptes Rendus (Dokaldy) de l'Academie Sciences de l'URSS* **1944**, *43* (329-331).

(2) McMillan, E. M. *Phys Rev* **1945**, *68* (143).

(3) *Fifty years of synchrotrons*; Sitges, Barcelona, Spain, 1996.

(4) Giancoli, D. C. *Physics*, 5 ed.; Prentice Hall: New Jersey, 1998.

(5) Smith, J. V. *Analyst* **1995**, *120* (5), 1231.

(6) Weekley, C. M. The Combined Application of XAS and XFM Techniques to the Problem of Selenium Speciation in Biological Systems, University of Adelaide, Adelaide, Australia, 2013.

(7) Castillo-Michel, H. A.; Larue, C.; Pradas Del Real, A. E.; Cotte, M.; Sarret, G. *Plant Physiol. Biochem.* **2017**, *110*, 13.

(8) Stewart, T. J. *Metallomics* **2019**, *11*, 29.

(9) Fahrni, C. J. *Curr. Opin. Chem. Biol.* **2007**, *11* (2), 121.

(10) Kehr, S.; Malinouski, M.; Finney, L.; Vogt, S.; Labunskyy, V. M.; Kasaikina, M. V.; Carlson, B. A.; Zhou, Y.; Hatfield, D. L.; Gladyshev, V. N. *J. Mol. Biol.* **2009**, *389* (5), 808.

(11) Aitken, J. B.; Lay, P. A.; Duong, T. T. H.; Aran, R.; Witting, P. K.; Harris, H. H.; Lai, B.; Vogt, S.; Giles, G. I. *J. Biol. Inorg. Chem.* **2012**, *17* (4), 589.

(12) Aitken, J. B.; Antony, S.; Weekley, C. M.; Lai, B.; Spiccia, L.; Harris, H. H. *Metallomics* **2012**, *4* (10), 1051.

(13) Aitken, J. B.; Levina, A.; Lay, P. A. *Curr. Top. Med. Chem.* **2011**, *11* (5), 553.

(14) Wang, H. C.; Riahi, M.; Pothen, J.; Bayse, C. A.; Riggs-Gelasco, P.; Brumaghim, J. L. *Inorg. Chem.* **2011**, *50* (21), 10893.

(15) Shanu, A.; Groebler, L.; Kim, H. B.; Wood, S.; Weekley, C. M.; Aitken, J. B.; Harris, H. H.; Witting, P. K. *Antiox. Redox Signal.* **2013**, *18* (7), 756.

(16) Malinouski, M.; Kehr, S.; Finney, L.; Vogt, S.; Carlson, B. A.; Seravalli, J.; Jin, R.; Handy, D. E.; Park, T. J.; Loscalzo, J.; Hatfield, D. L.; Gladyshev, V. N. *Antiox. Redox Signal.* **2012**, *16* (3), 185.

(17) Misra, S.; Peak, D.; Chen, N.; Hamilton, C.; Niyogi, S. *Comp. Biochem. Physiol. C Toxicol. Pharmacol.* **2012**, *155* (4), 560.

(18) Majumdar, S.; Peralta-Videa, J. R.; Castillo-Michel, H.; Hong, J.; Rico, C. M.; Gardea-

Torresdey, J. L. *Anal. Chim. Acta* **2012**, *755*, 1.

(19) Lombi, E.; Scheckel, K. G.; Kempson, I. M. *Environ. Exp. Bot.* **2011**, *72*, 3.

(20) Lombi, E.; Susini, J. *Plant Soil* **2009**, *320*, 1.

(21) Lombi, E.; de Jonge, M. D.; Donner, E.; Ryan, C. G.; Paterson, D. *Anal. Bioanal. Chem.* **2011**, *400*, 1637.

(22) Fittschen, U. E. A.; Flakenberg, G. *Spectrochim. Acta Part B* **2011**, *66*, 567.

(23) Yu-Feng, L.; Xiaoyan, W.; Liming, W.; Bai, L.; Yuxi, G.; Chunying, C. *J. Anal. At. Spectrom.* **2010**, *25* (3), 426.

(24) George, G. N.; Hedman, B.; Hodgson, K. O. *Nat. Struct. Mol. Biol.* **1998**, *5*, 645.

(25) VB, B.; GN, K.; AN, S. *Nucl. Instrum. Methods Phys. Res. A* **1986**, *246* (1-3), 739.

(26) New, E. J.; Wimmer, V. C.; Hare, D. J. *Cell Chem. Biol.* **2018**, *25*, 7.

(27) Haraguchi, H. *J. Anal. At. Spectrom.* **2004**, *19*, 5.

(28) Chang, C. J. *Nat. Chem. Biol.* **2015**, *11*, 744.

(29) Irving, H.; Williams, R. J. P. *J. Chem. Soc.* **1953**, 3192.

(30) Poulos, T. L. *Chem. Rev.* **2014**, *114* (7), 3919.

(31) Sahu, S.; Goldberg, D. P. *J. Am. Chem. Soc.* **2016**, *138* (36), 11410.

(32) Solomon, E. I.; Heppner, D. E.; Johnston, E. M.; Ginsbach, J. W.; Cirera, J.; Qayyum, M.; Kieber-Emmons, M. T.; Kjaergaard, C. H.; Hadt, R. G.; Tian, L. *Chem. Rev.* **2014**, *114* (7), 3659.

(33) Solomon, E. I.; Light, K. M.; Liu, L. V.; Srnec, M.; Wong, S. D. *Acc. Chem. Res.* **2013**, *46* (11), 2725.

(34) Holm, R. H.; Kennepohl, P.; Solomon, E. I. *Chem. Rev.* **1996**, *96*, 2239.

(35) Waldron, K. J.; Rutherford, J. C.; Ford, D.; Robinson, N. J. *Nature* **2009**, *460*, 823.

(36) Stockwell, B. R.; Angeli, J. P. F.; Bayir, H. L.; Bush, A. I.; Conrad, M.; Dixon, S. J.; Fulda, S.; Gascon, S.; Hatzios, S. K.; Kagan, V. E.; Noel, K.; Jiang, X.; Linkermann, A.; Murphy, M. E.; Overholtzer, M.; Oyagi, A.; Pagnussat, G. C.; Park, J.; Ran, Q.; Rosenfeld, C. S.; Salnikow, K.; Tang, D.; Torti, F. M.; Torti, S. V.; Toyokuni, S.; Woerpel, K. A.; Zhang, D. D. *Cell* **2017**, *171*, 273.

(37) Williams, J. R.; Trias, E.; Beilby, P. R.; Lopez, N. I.; Labut, E. M.; Bradford, C. S.; Roberts, B. R.; McAllum, E. J.; Crouch, P. J.; Rhoads, T. W.; Pereira, C.; Son, M.; Elliott, J. L.; Franco, M. C.; Estevez, A. G.; Barbeito, L.; Beckman, J. S. *Neurobio. Dis.* **2016**, *89*, 1.

(38) Martin-Bastida, A.; Ward, R. J.; Newbould, R.; Piccini, P.; Sharp, D.; Kabba, C.; Patel, M. C.; Spino, M.; Connelly, J.; Tricta, F.; Dexter, R. R. C. D. T. *Sci Rep* **2017**, *7* (1398).

(39) Andreini, C.; Bertini, I.; Rosato, A. *Bioinformatics* **2004**, *20*, 1373.

(40) Cvetkovic, A.; Menon, A. L.; Thorgersen, M. P.; Scott, J. W.; Poole, F. L., II; Jenney, F. E., Jr; Lancaster, W. A.; Praissman, J. L.; Shanmukh, S.; Vaccaro, B. J.; Trauger, S. A.; Kalisiak, E.; Apon, J. V.; Siuzdak, G.; Yannone, S. M.; Adams, J. A. T. M. W. W. *Nature* **2010**, *466*, 779.

(41) Valko, M.; Jomova, K.; Musilek, K.; Rhodes, C. J.; Kuca, K. *Arch. Toxicol.* **2016**, *90*, 1.

(42) Ryu, M.-S.; Zhang, D.; Protchenko, O.; Shakoury-Elizeh, M.; Philpott, C. C. *J. Clin. Invest.* **2017**, *127*, 1786.

(43) Banci, L.; Bertini, I.; Ciofi-Baffoni, S.; Kozyreva, T.; Zovo, K.; Palumaa, P. *Nature* **2010**, *465*, 645.

(44) Campuzano, V.; Montermini, L.; Moltò, M. D.; Pianese, L.; Cossée, M.; Cavalcanti, F.; Monros, E.; Rodius, F.; Duclos, F.; Monticelli, A.; Zara, F.; Cañizares, J.; Koutnikova, H.; Bidichandani, S. I.; Gellera, C.; Brice, A.; Trouillas, P.; De Michele, G.; Filla, A.; De Frutos, R.; Palau, F.; Patel, P. I.; Di Donato, S.; Mandel, J.-L.; Cocozza, S.; Koenig, M.; Pandolfo, M. *Science* **1996**, *271* (5254), 1423.

(45) Levi, S.; Rovida, E. *Neurobio. Dis.* **2015**, *81*, 134.

(46) Trist, B. G.; Davies, K. M.; Cottam, V.; Genoud, S.; Ortega, R.; Roudeau, S.; Carmona, A.; De Silva, K.; Wasinger, V.; Lewis, S. J. G.; Sachdev, P.; Smith, B.; Troakes, C.; Vance, C.; Shaw, C.; Al-Sarraj, S.; Ball, H. J.; Halliday, G. M.; Hare, D. J.; Double, K. L. *Acta Neuropathol.* **2017**, *134* (1), 113.

(47) McRae, R.; Bagchi, P.; Sumalekshmy, S. *Chem. Rev.* **2009**, *109*, 4780.

(48) Roudeau, S.; Carmona, A.; Perrin, L.; Ortega, R. *Anal. Bioanal. Chem.* **2014**, *406* (27), 6979.

(49) Hackett, M. J.; McQuillan, J. A.; El-Assaad, F.; Aitken, J. B.; Levina, A.; Cohen, D. D.; Siegele, R.; Carter, E. A.; Grau, G. E.; Hunt, N. H.; Lay, P. A. *Analyst* **2011**, *136* (14), 2941.

(50) James, S. A.; Myers, D. E.; de Jonge, M. D.; Vogt, S.; Ryan, C. G.; Sexton, B. A.; Hoobin, P.; Paterson, D.; Howard, D. L.; Mayo, S. C.; Altissimo, M.; Moorhead, G. F.; Wilkins, S. W. *Anal. Bioanal. Chem.* **2011**, *401* (3), 853.

(51) Perrin, L.; Carmona, A.; Roudeau, S.; Ortega, R. *J. Anal. At. Spectrom.* **2015**, *30* (12), 2525.

(52) Carter, K. P.; Young, A. M.; Palmer, A. E. *Chem. Rev.* **2014**, *114* (8), 4564.

(53) Ackerman, C. M.; Lee, S.; Chang, C. J. *Anal. Chem.* **2016**, *89* (1), 22.

(54) Levina, A.; Mitra, A.; Lay, P. A. *Metallomics* **2009**, *1* (6), 458.

(55) Michlewska, S.; Ionov, M.; Maroto-Díaz, M.; Szwed, A.; Ihnatsyeu-Kachan, A.; Loznikova, S.; Shcharbin, D.; Maly, M.; Ramirez, R. G.; la Mata, de, F. J.; Bryszewska, M. *J. Inorg. Biochem.* **2018**, *181*, 18.

(56) Duan, X.; Wang, Y.; Zhang, F.; Lu, L.; Cao, M.; Lin, B.; Zhang, X.; Mao, J.; Shuai, X.; Shen, J. *J Biomed Nanotechnol* **2016**, *12*, 2112.

(57) Hare, D. J.; McCollb, G.; New, E.; de Jonge, M. D. *Chem. Soc. Rev.* **2015**, *44*, 5941.

(58) Polishchuk, R.; Lutsenko, S. *Histochem. Cell Biol.* **2013**, *140* (3), 285.

(59) Paunesku, T.; Vogt, S.; Maser, J.; Lai, B. *J. Cell. Biochem.* **2006**, *99*, 1489.

(60) Weekley, C. M.; Aitken, J. B.; Vogt, S.; Finney, L. A.; Paterson, D. J.; de Jonge, M. D.; Howard, D. L.; Musgrave, I. F.; Harris, H. H. *Biochemistry* **2011**, *50* (10), 1641.

(61) Weekley, C. M.; Aitken, J. B.; Vogt, S.; Finney, L. A.; Paterson, D. J.; de Jonge, M. D.; Howard, D. L.; Witting, P. K.; Musgrave, I. F.; Harris, H. H. *J. Am. Chem. Soc.* **2011**, *133*, 18772.

(62) Korbas, M.; O'Donoghue, J. L.; Watson, G. E.; Pickering, I. J.; Singh, S. P.; Myers, G. J.; Clarkson, T. W.; George, G. N. *ACS Chem Neurosci* **2010**, *1* (12), 810.

(63) Weekley, C. M.; Shanu, A.; Aitken, J. B.; Vogt, S.; Witting, P. K.; Harris, H. H. *Metallomics* **2014**, *6* (9), 1602.

(64) Gransbury, G. K.; Kappen, P.; Glover, C. J.; Hughes, J. N.; Levina, A.; Lay, P. A.; Musgrave, I. F.; Harris, H. H. *Metallomics* **2016**, *8* (8), 762.

(65) Chevallet, M.; Veronesi, G.; Fuchs, A.; Mintz, E.; Michaud-Soret, I.; Deniaud, A. *Biochim. Biophys. Acta* **2017**, *1861* (6), 1566.

(66) Shen, C. L.; song, W.; Pence, B. C. *Cancer Epidemiol. Biomarkers Prev.* **2001**, *10* (4), 385.

(67) Reeves, M. A.; Hoffmann, P. R. *Cell Mol. Life Sci.* **2009**, *66* (15), 2457.

(68) B'Hymer, C.; Caruso, J. A. *J. Chromatogr. A* **2006**, *1114* (1), 1.

CHAPTER 2. Intracellular distribution and stability of a luminescent rhenium(I) tricarbonyl tertazolato complex using epifluorescence microscopy in conjunction with X-ray fluorescence imaging.

Jason Wedding and Hugh Harris*

*School of Physical Sciences, The University of Adelaide, SA, 5005, Australia

Chapter 2. Statements of Authorship

Statement of Authorship

Title of Paper	Intracellullar distribution and stability of a luminescent rhenium(I) tricarbonyl tetrazolato complex using epifluorecence microscopy in conjunction with X-ray fluorescence imaging.
Publication Status	☐ Published ☐ Accepted for Publication ☐ Submitted for Publication ☐ Unpublished and Unsubmitted w ork w ritten in manuscript style
Publication Details	Wedding, J. L., Harris, H. H., Bader, C. A., Plush, S. E., Mak, R., Massi, M., Brooks, D. A., Lai, B., Vogt, S., Werrett, M. V., Simpson, P. V., Skelton, B. W., Stagni, S., *Intracellullar distribution and stability of a luminescent rhenium(I) tricarbonyl tetrazolato complex using epifluorecence microscopy in conjunction with X-ray fluorescence imaging*, Metallomics : integrated biometal science 9 4 (2017): 382-390, DOI:10.1039/c6mt00243a

Principal Author

Name of Principal Author (Candidate)	Jason Lee Wedding		
Contribution to the Paper	Worked with those listed below to design experiment, carried out biological-sample related experiments, performed epifluorescence microscopy, analysed all imaging data, interpreted data and conceived and prepared manuscript.		
Overall percentage (%)	40%		
Certification:	This paper reports on original research I conducted during the period of my Higher Degree by Research candidature and is not subject to any obligations or contractual agreements with a third party that would constrain its inclusion in this thesis. I am the primary author of this paper.		
Signature	[redacted]	Date	11/2/2019.

Co-Author Contributions

By signing the Statement of Authorship, each author certifies that:

i. the candidate's stated contribution to the publication is accurate (as detailed above);

ii. permission is granted for the candidate in include the publication in the thesis; and

iii. the sum of all co-author contributions is equal to 100% less the candidate's stated contribution.

Name of Co-Author	Hugh H. Harris		
Contribution to the Paper	Supervised the development of the work, assisted with the conception and development of the manuscript and acted as a corresponding author.		
Signature	[redacted]	Date	11/2/2019

Name of Co-Author	Rachel Mak		
Contribution to the Paper	Assisted with collection of XRF imaging data. Signed by Hugh Harris on behalf of Rachel Mak		
Signature	[redacted]	Date	11/2/2019

Name of Co-Author	Christie A. Bader		
Contribution to the Paper	Assisted with biological-sample related experiments, assisted with epifluorescence microscopy.		
Signature		Date	22/01/2019

Name of Co-Author	Sally E. Plush		
Contribution to the Paper	Supervised the development of the work, assisted with the conception and development of the manuscript.		
Signature		Date	21/01/2019

Name of Co-Author	Douglas A. Brooks		
Contribution to the Paper	Supervised the development of the work, assisted with the conception and development of the manuscript.		
Signature		Date	21/01/2019

Name of Co-Author	Melissa V. Werret		
Contribution to the Paper	Responsible for synthesis and characterisation of the treatment compound.		
Signature		Date	21/1/19

Name of Co-Author	Peter V. Simpson		
Contribution to the Paper	Responsible for photophysical characterisation of the treatment compound.		
Signature		Date	21/1/19

Name of Co-Author	Brian W. Skelton		
Contribution to the Paper	Responsible for collection and analysis of X-ray diffraction crystallographic data of treatment compounds.		
Signature		Date	21/01/2019

Name of Co-Author	Massimiliano Massi		
Contribution to the Paper	Supervised the development of the work, assisted with the conception and development of the manuscript and acted as a corresponding author.		
Signature		Date	18/01/19

Name of Co-Author	Stefano Stagni		
Contribution to the Paper	Supervised the development of the work, assisted with the conception and development of the manuscript.		
Signature		Date	18/01/19

Name of Co-Author	Barry Lai		
Contribution to the Paper	Assisted with the collection and analysis of XFM data.		
Signature		Date	Jan. 21, 2019

Name of Co-Author	Stefan Vogt		
Contribution to the Paper	Assisted with the collection and analysis of XFM data.		
Signature		Date	Feb 2. 2019

Volume 9 | Number 4 | April 2017 | Pages 337–426

Metallomics

rsc.li/metallomics

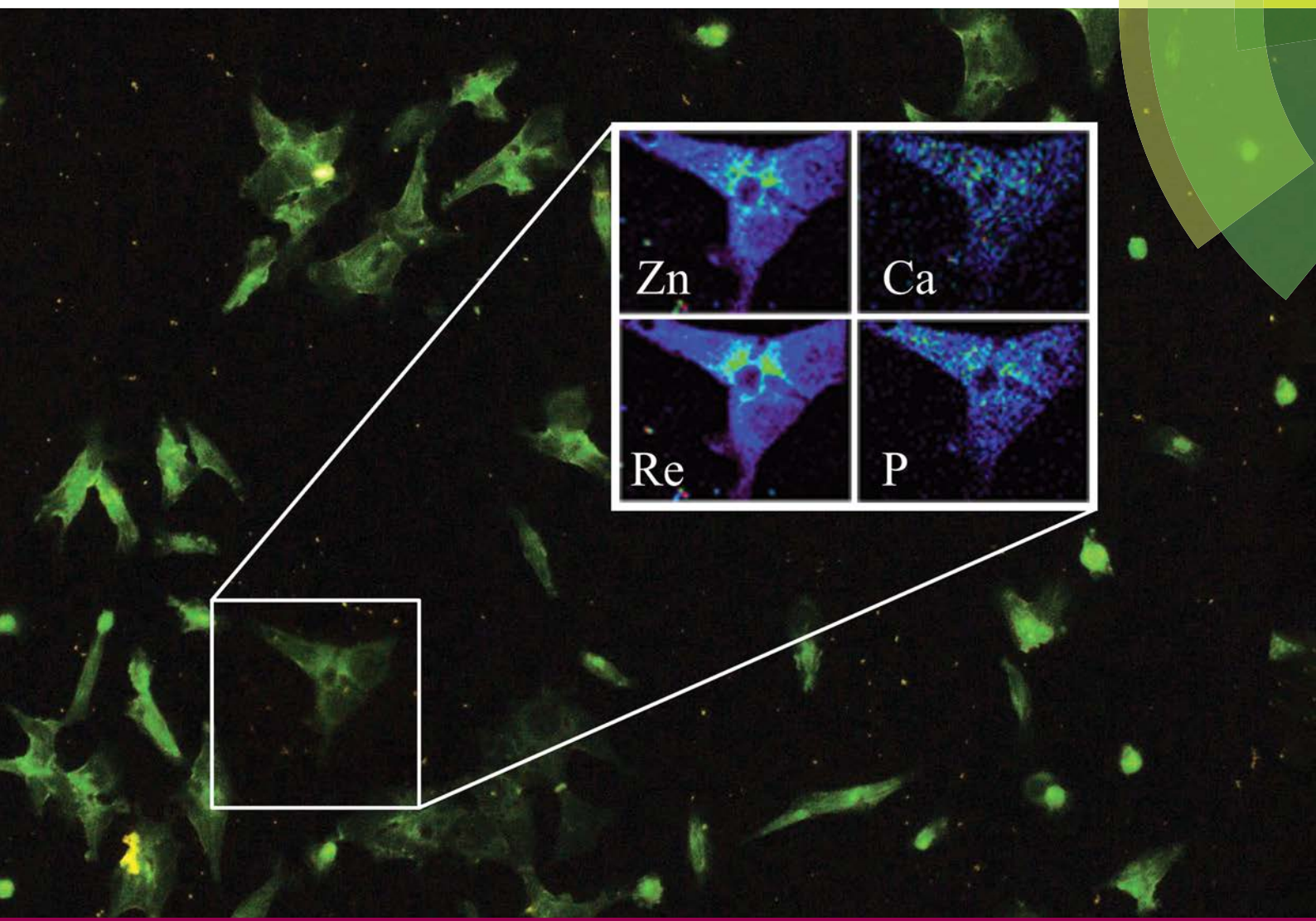

Themed issue: Imaging Metals in Biology

ISSN 1756-591X

ROYAL SOCIETY OF CHEMISTRY

PAPER
H. H. Harris, M. Massi *et al.*
Intracellular distribution and stability of a luminescent rhenium(I) tricarbonyl tetrazolato complex using epifluorescence microscopy in conjunction with X-ray fluorescence imaging

Indexed in Medline!

Metallomics

PAPER

View Article Online
View Journal | View Issue

Cite this: *Metallomics*, 2017, 9, 382

Intracellular distribution and stability of a luminescent rhenium(I) tricarbonyl tetrazolato complex using epifluorescence microscopy in conjunction with X-ray fluorescence imaging†

J. L. Wedding,[a] H. H. Harris,*[a] C. A. Bader,[b] S. E. Plush,[b] R. Mak,[c] M. Massi,*[d] D. A. Brooks,[b] B. Lai,[e] S. Vogt,[e] M. V. Werrett,[d] P. V. Simpson,[d] B. W. Skelton[f] and S. Stagni[g]

Received 21st October 2016,
Accepted 22nd November 2016

DOI: 10.1039/c6mt00243a

www.rsc.org/metallomics

Optical epifluorescence microscopy was used in conjunction with X-ray fluorescence imaging to monitor the stability and intracellular distribution of the luminescent rhenium(I) complex *fac*-[Re(CO)$_3$(phen)L], where phen = 1,10-phenathroline and L = 5-(4-iodophenyl)tetrazolato, in 22Rv1 cells. The rhenium complex showed no signs of ancillary ligand dissociation, a conclusion based on data obtained *via* X-ray fluorescence imaging aligning iodine and rhenium distributions. A diffuse reticular localisation was detected for the complex in the nuclear/perinuclear region of cells, by either optical or X-ray fluorescence imaging techniques. X-ray fluorescence also showed that the rhenium complex disrupted the homeostasis of some biologically relevant elements, such as chlorine, potassium and zinc.

Significance to metallomics

Organelle or tissue targeted luminescent imaging agents are vital tools for researchers hoping to enhance knowledge of fundamental physiological processes. Metal complexes offer a number of advantages as imaging agents compared to other species due to favourable photophysical properties, but the subtle chemistry they display gives rise to the potential for artefacts that may cloud the information they provide. By correlating optical fluorescence microscopy of treated cells with elemental distribution from X-ray fluorescence imaging of the same cells, we have demonstrated stability in a biological setting for a Re(I) tricarbonyl-based imaging agent which allays concerns regarding artefactual data from its use.

Introduction

Interest and advancement of coordinated group VII elements, such as rhenium and technetium, has been largely due to their application as radionuclides in the development of radiopharmaceuticals[1–5] and as optical dyes for cellular imaging in microscopy.[6–9] The ability to incorporate these radionuclides into tracer molecules has been at the forefront in developing diagnostic radiopharmaceuticals.[10] ^{99m}Technetium has become a popular choice, being used in over 85% of diagnostic scans every year, due to its medicinally appropriate half-life, wide range of compatible ligands affording stable complexes and low bioaccumulation rates in patients.[3,6,10,11] Luminescent metal complexes of rhenium(I), ruthenium(II) and iridium(III) have found considerable application as luminescent imaging agents due to their favorable photophysical properties.[5–7,12,13] In particular, their large Stokes shifts prevent concentration quenching phenomena and, along with their long excited state lifetime, allows for easier discrimination from background autofluorescence. Furthermore, chemical design can render these complexes photostable, thus preventing fast bleaching upon excitation. Bioconjugation of these complexes to biological vectors (such as avidin or octreotide) has been successfully employed to

[a] *Department of Chemistry, The University of Adelaide, SA 5005, Australia. E-mail: hugh.harris@adelaide.edu.au*
[b] *School of Pharmacy and Medical Sciences, University of South Australia, Adelaide, South Australia, 5005, Australia*
[c] *School of Chemistry, The University of Sydney, NSW 2006, Australia*
[d] *Department of Chemistry, Perth, Western Australia, 6102, Australia. E-mail: M.Massi@curtin.edu.au*
[e] *Advanced Photon Source, X-ray Science Division, Argonne National Laboratory, Argonne, IL 60439, USA*
[f] *Centre for Microscopy, Characterisation and Analysis, University of Western Australia, Crawley 6009 WA, Australia*
[g] *Department of Industrial Chemistry "Toso Montanari" – University of Bologna, viale del Risorgimento 4, Bologna 40136, Italy*

† Electronic supplementary information (ESI) available: Details of X-ray crystallography and UV-Vis absorption/emission spectra. CCDC 1510599. For ESI and crystallographic data in CIF or other electronic format see DOI: 10.1039/c6mt00243a

confer biological specificity in cell lines, including specific organelles, after internalisation.[2,4,6–8]

Rhenium[14,15] and iridium[2,16,17] complexes have already been shown to be useful as cellular imaging agents due to their favorable intracellular localisations and organelle targeting,[18] and offer the possibility of combining their functions as fluorescence microscopy imaging agents with *in vivo* radio-imaging.[5,19–22] For example rhenium(I) is used as a "cold", or non-radioactive, ^{99m}technetium chemical analogue, thereby allowing for insight into the *in vivo* and *in vitro* localisations of ^{99m}technetium analogues.[18,23]

As a result of extensive attention, the chemistry of rhenium organometallic complexes is well documented.[3–5,10,11,23–26] A wide range of accessible oxidation states (−1 to +7) lends structural diversity to rhenium complexes, however the low oxidation state complexes are more kinetically stable and hence more suitable for use as fluorescence imaging agents.[3,5]

The most studied[18,27–31] luminescent rhenium complexes belong to the family of *fac*-$[Re(CO)_3(diim)X]^{0/+}$, where diim is a bidentate diimine ligand such as 1,10-phenathroline (phen) and X is a monodentate anionic or neutral ancillary ligand such as chloride or pyridine.[32] These complexes have well documented photophysical properties that can be appropriately adjusted *via* the introduction of various functional groups into the diimine or ancillary ligand. Furthermore, chemical modification of these complexes can be used to modulate their lipophilicity and optimise cellular uptake and cytotoxicity. Consequently, *fac*-$[Re(CO)_3(diim)X]^{0/+}$ complexes have generally shown low levels of cytotoxicity.[13] However, in some cases, cytotoxic effects have been observed in a number of cell lines, although the specific mechanism is not yet clearly elucidated.[33]

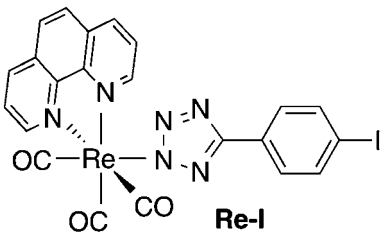

Re-I

In our studies, we have investigated the cellular uptake and localisation of neutral *fac*-$[Re(CO)_3(phen)T]$ complexes, where T represents an aryltetrazolato ligand. These complexes localise in different organelles such as lipid droplets,[34] endoplasmic reticulum,[35] and acidic vesicles[34] depending of the specific substituent present on the tetrazolato ligand. For example, the rhenium species bound to 5-(4-cyanophenyl)-tetrazolate accumulates in lipid droplets with a high specificity for polar lipids such as phosphatidylethanolamine, cholesterol and sphingomyelin,[36] and allows the visualisation of polar lipid trafficking.[37] On the other hand, the rhenium species bound to 5-(pyrid-4-yl)-tetrazolate strongly located in the endoplasmic reticulum and permitted the visualisation of membrane events in live cells.[35] These complexes were all found to be highly amenable to long term imaging in live cells and exhibited very low toxicity. The previous studies suggest that these rhenium tetrazolato complexes are kinetically inert and do not undergo ligand exchange reactions, at least before their specific targeted organelle is reached. This study therefore aimed to prove this and assess the stability of a rhenium tetrazolato complex after cellular incubation. For this scope, the complex *fac*-$[Re(CO)_3(phen)L]$ was synthesised, where L is 5-(4-iodophenyl)-tetrazolate (iodine was initially installed with a view to further coupling chemistry) and the complex is herein referred to as **Re–I.** The aim is to combine optical epifluorescence microscopy alongside X-ray fluorescence (XRF) imaging to monitor the intracellular localisation of the Re metal center and an I-labeled 5-(4-iodophenyl)tetrazolate ancillary ligand.

Experimental

Synthesis and characterisation

All reagents and solvents were purchased from Sigma Aldrich or Alfa Aesar. Nuclear magnetic resonance spectra were recorded using a Bruker Avance 400 spectrometer (400 MHz for ^{1}H NMR; 100 MHz for ^{13}C NMR) at 300 K. All NMR spectra were calibrated to residual solvent signals. Infrared spectra were recorded using an attenuated total reflectance Perkin Elmer Spectrum 100 FT-IR with a diamond stage. IR spectra were recorded from 4000–650 cm^{-1}. The intensities of the band are reported as strong (s), medium (m), or weak (w), with broad (br) bands also specified. Melting points were determined using a BI Barnsted Electrotermal 9100 apparatus. Elemental analysis were carried out on bulk samples using a Thermo Finning EA 1112 Series Flash.

1*H*-5-(4-Iodophenyl)tetrazole was prepared following the methodology described by Koguro.[38] Yield 57%. M.p. 268–269 °C (dec.). ν_{max}/cm^{-1}: 2964 w, 2816 w, 2668 w, 2514 m, 2445 m, 1906 m, 1602 s, 1557 m, 1492 w, 1478 m, 1431 s, 1405 w, 1364 w, 1272 w, 1252 w, 1165 m, 1117 w, 1088 w, 1055 m, 1025 w, 1005 w, 81 s, 826 s, 742 m, 711 w, 693 w. ^{1}H-NMR δ/ppm (DMSO-d_6): 7.98 (2H, d, J = 8.4 Hz, Ph H2,6), 7.81 (2H, d, J = 8.4 Hz, Ph H3,5). ^{13}C-NMR δ/ppm (DMSO-d_6): 155.2 ($\underline{C}N_4$), 138.3, 128.7, 123.8, 98.4.

The synthesis of **Re–I** was performed according to the following procedure. *fac*-$[Re(CO)_3(phen)Cl]$ (0.10 g, 0.2 mmol) was added to 10 mL of 3 : 1 a (v/v) ethanol/water solvent mixture. To this suspension, a solution obtained by dissolving 1*H*-5-(4-iodophenyl)tetrazole (1.6 eq.) and triethylamine (1.6 eq.) in 2.5 mL of 3 : 1 a (v/v) ethanol/water solvent mixture was added. The mixture was vigorously stirred and heated at reflux for 20 h. After this time, the mixture was cooled to room temperature, filtered over a glass frit, and washed with a 3 : 1 a (v/v) ethanol/water solvent mixture (5 mL) to afford the desired complex as a yellow microcrystalline powder. Yield 95%. M.p. 291.3–291.9 °C (dec.). Elemental analysis for $C_{22}H_{12}IN_6O_3Re$: calculated: C 36.62, H 1.68, N 11.65; found: C 36.43, H 1.44, N 11.46. ν_{max}/cm^{-1}: 3798 w, 3060 w, 2023 s (CO, A′(1)), 1908 br s (CO, A′(2)/A″), 1631 w, 1600 w, 1584 w, 1425 m, 1411 m, 1338 w, 1269 w, 1226 w, 1177 w, 1146 w, 1117 w, 1038 w, 1000 w, 965 w, 848 w, 825 w, 779 w, 748 w, 721 w. ^{1}H-NMR δ/ppm (acetone-d_6): 9.65 (2H, d, J = 5.2 Hz, phen H2,9), 8.96 (2H, d, J = 8.2 Hz, phen H4,7), 8.30 (2H, s, phen H5,6), 8.19–8.15 (2H, m, phen H3,8), 7.62 (2H, d, J = 8.4 Hz, Ph H3,5), 7.43 (2H, d, J = 8.8 Hz, Ph H2,6).

^{13}C-NMR δ/ppm (acetone-d_6): 162.9 ($\underline{C}N_4$), 155.2, 148.3, 140.4, 138.4, 131.7, 130.9, 128.7, 128.6, 127.4, 93.9. Crystals suitable for X-ray analysis were obtained by liquid–liquid diffusion of petroleum spirits into a dichloromethane solution of **Re–I** (see ESI†).

Photophysical measurements

Absorption spectra were recorded at room temperature using a Cary 4000 UV/Vis spectrometer. Uncorrected steady state emission and excitation spectra were recorded on an Edinburgh FLSP980-S2S2-stm spectrometer equipped with: (i) a temperature-monitored cuvette holder; (ii) 450 W Xenon arc lamp; (iii) double excitation and emission monochromators; (iv) a Peltier cooled Hamamatsu R928P photomultiplier tube (spectral range 200–870 nm). Emission and excitation spectra were corrected for source intensity (lamp and grating) and emission spectral response (detector and grating) by a calibration curve supplied with the instrument. According to the approach described by Demas and Crosby,[39] luminescence quantum yields (Φ_{em}) were measured in optically dilute solutions (O.D. <0.1 at excitation wavelength) obtained from absorption spectra on a wavelength scale [nm] and compared to the reference emitter by the following equation:

$$\Phi_x = \Phi_r \left[\frac{A_r(\lambda_r)}{A_x\lambda_x}\right]\left[\frac{I_r(\lambda_r)}{I_x\lambda_x}\right]\left[\frac{n_x^2}{n_r^2}\right]\left[\frac{D_x}{D_r}\right]$$

where A is the absorbance at the excitation wavelength (λ), I is the intensity of the excitation light at the excitation wavelength (λ), n is the refractive index of the solvent, D is the integrated intensity of the luminescence and Φ is the quantum yield. The subscripts r and x refer to the reference and the sample, respectively. The quantum yield determinations were performed at identical excitation wavelength for the sample and the reference, therefore cancelling the $I(\lambda_r)/I(\lambda_x)$ term in the equation. The quantum yields of complexes were measured against an aqueous solution of $[Ru(bipy)_3]Cl_2$ (bipy = 2,2′-bipyridine; $\Phi_r = 0.028$).[40] Emission lifetimes (τ) were determined with the time correlated single photon counting technique (TCSPC) with the same Edinburgh FLSP980-S2S2-stm spectrometer using a pulsed picosecond LED (EPLED/EPL 377 nm, FHWM $<$ 800 ps). The goodness of fit was assessed by minimising the reduced χ^2 function and by visual inspection of the weighted residuals. The dichloromethane solvent used for the preparation of the solutions for the photophysical investigations were of LR grade. Degassing of the dichloromethane solution was performed using the freeze–pump–thaw method. Experimental uncertainties are estimated to be $\pm$8% for lifetime determinations, $\pm$20% for quantum yields, $\pm$2 nm and $\pm$5 nm for absorption and emission peaks, respectively.

Cell culture

22Rv1 human prostate epithelial carcinoma cells, originally purchased from the European Collection of Cell Cultures *via* CellBank Australia (Children's Medical Research Institute, New South Wales Australia), were cultured as monolayers in complete RPMI-1640 (Sigma Life Sciences) supplemented with foetal bovine serum (10% v/v; Invitrogen Australia, Thermo-Fischer Scientific), L-glutamine (2 mM, Sigma Life Sciences), antibiotic–antimyotic mixture (100 mg mL^{-1} penicillin and 100 U mL^{-1} streptomycin; Sigma Life Sciences) at 310 K in a 5% CO_2-humidified incubator and were sub-cultured every 3–4 days.

Preparation of Re–I treatment solutions

Re–I was dissolved in DMSO to produce a 10 mM solution. This solution was then diluted with PBS to the treatment concentration of 10 μM (0.1% DMSO).

Cell treatment sample preparations

Cells were prepared for XRF imaging by growth on 1.5 × 1.5 mm × 500 nm silicon nitride windows (Silson, UK) in 6-well plates as described previously.[41–46] The plates were seeded at 1×10^6 cells per well in complete DMEM and were incubated at 310 K in a 5% CO_2-humidified incubator for 24 h prior to treatment. Cells were then treated with **Re–I** (for either 2 or 4 h) or DMSO (0.1%) as a vehicle-only control for 2 h. At the end of the treatment time the medium was removed and cells were fixed with 3.7% paraformaldehyde (prepared fresh in PBS) solution for 15 min. Fixed windows were then washed with PBS, ammonium acetate (in Milli-Q water) and Milli-Q water thrice. (Procedure adapted from ref. 47 and 48.)

Spectroscopic data collection

Optical epifluorescence images were collected with an Olympus BX53 upright fluorescence microscope (Olympus, Australia), with a 10× lens and excitation wash with a blue LED and images were collected in bright field mode or using a long band pass filter.

XRF elemental distribution maps of single cells were recorded on beamline 2-ID-D at the Advanced Photon Source (APS), Argonne National Laboratory, Illinois, USA. The X-ray beam was tuned to an incident energy of 12.7 keV using a double crystal monochromator and was focused to a diameter of ~0.25 μm using a "high-flux" zone plate. A single element silicon drift energy dispersive detector (Vortex EX, SII Nano-technology, Northridge, CA), at 90° to the incident beam, was used to collect the fluorescence signal for 1 s per spatial point from samples under a He atmosphere.

Four to eight individual cells per sample were selected and located using an optical microscope (Leica DMRXE). Cells were subsequently relocated in the beamline by correlating the light microscope coordinates with those determined from the X-ray transmission image of the window as viewed on a CCD camera. Whole cells were raster scanned using a 25 nm accuracy Newport sample positioning stage. Low resolution scans with a step size of 4 μm and a dwell time of 0.5 s were used to locate the cells before obtaining high-resolution scans with a step size of 0.5 μm and a dwell time of 1 s.

XRF imaging data analysis

The fluorescence spectrum at each spatial point was fit to Gaussians, modified by the addition of a step function and a tailing function to describe mostly incomplete charge collection and other detector artefacts.[49,50] The integrated fluorescence spectra extracted from these regions were also fit with modified Gaussians to determine average elemental area densities

(in units of μg cm^{-2}). Quantification was performed by comparison to the corresponding measurements on the thin-film standards NBS-1832 and NBS-1833 from the National Bureau of Standards (Gaithersburg, MD). The analysis was performed using MAPS software.[42,50]

Results

The complex **Re–I** was obtained *via* a direct ligand exchange reaction between the chloro ligand in *fac*-[Re(CO)$_3$(phen)Cl] with the tetrazolate anion. Compared to previously investigated methodologies, involving the preparation of the intermediate complex *fac*-[Re(CO)$_3$(phen)(NCCH$_3$)]$^+$,[51] the direct exchange yields the targeted compound in high purity without the need of chromatographic purification. The species **Re–I** displays the expected peaks belonging to the CO ligands at 2023 and 1908 cm^{-1} in the IR spectrum, as typical for rhenium tetrazolato complexes of *facial* configuration.[51] The formulation of **Re–I** was further supported by NMR and elemental analysis. Single crystals suitable for X-ray diffraction could be obtained by layering petroleum spirits onto a dichloromethane solution of the complex. The obtained structure (see ESI†) highlights the expected rhenium complex coordinated by three *facial* CO ligands, a chelating phen and the N2 coordinated tetrazolato ligand.

The photophysical data for **Re–I** from a diluted dichloromethane solution are reported in Table 1, and the relative absorption, excitation, and emission spectra are reported in the ESI.† As expected for this class of rhenium complexes,[51] the absorption profile presents an intense band in the 250–310 nm region originating from ligand centered (LC) ππ* transitions on the phen and tetrazolato ligands. A further band of lower intensity is visible in the 310–420 nm region, typical of metal-to-ligand charge transfer transitions (MLCT) partially mixed with ligand-to-ligand charge transfer character (LLCT). Upon excitation to the charge transfer manifold, **Re–I** exhibits an emission profile that is broad and structureless with a maximum at 590 nm. The elongation of the excited state lifetime (τ) from 0.262 to 0.591 μs upon degassing, along with an increase of the photoluminescence quantum yield (Φ), supports the assignment of triplet spin multiplicity to the excited state (^{3}MLCT).

Table 1 Photophysical data for **Re–I** from diluted (*ca* 10^{-5} M) dichloromethane solutions

Absorption: λ_{max}/nm (ε/10^4 M^{-1} cm^{-1})	267 (5.15), 365 (0.50)
Emission – 298 K: λ_{max}/nm	590
Air-equilibrated – 298 K: τ/μs	0.262
Deaerated – 298 K: τ/μs	0.591
Air-equilibrated Φ	0.028
Deaerated Φ	0.083
k_r/10^6 s^{-1}	0.14
k_{nr}/10^6 s^{-1}	1.55

Cellular uptake and distribution of **Re–I** was investigated using optical epifluorescence and X-ray fluorescence microscopy. 22Rv1 cells were grown on silicon nitride windows overnight before being treated with **Re–I** for 2 and 4 h. After incubation, the cells were fixed in paraformaldehyde and freeze dried before imaging. The use of paraformaldehyde as a fixative agent is known to preserve the morphology of cells for optical fluorescence and XRF imaging.[43,44,52] The optical fluorescence of the entire window was imaged and stitched together immediately after fixation. Samples were then transported to the Advanced Photon Source (APS), Argonne National Laboratory, Illinois, USA for subsequent XRF imaging.

The zinc (Zn) map was used to identify the approximate boundaries of the cells as this element showed consistently higher signal-to-noise ratio (Fig. 1). The synchrotron beam was raster scanned to simultaneously obtain elemental maps of individual cells. As the beam moved across the cells the resulting fluorescence spectrum at each dwell point was collected and formed a single pixel within the elemental map.

Elemental maps were obtained for typically important biological elements (P, S, Cl, K, Ca) as well as transition metals (Fe, Zn). Rhenium concentrations were below detection limit within the control cells (Fig. 1), – no rhenium-based fluorescence signal was observed, nor any definable cellular localisation. Likewise, iodine was only found to be present in extremely low native concentrations in the control cells, with a very poorly defined intracellular distribution.

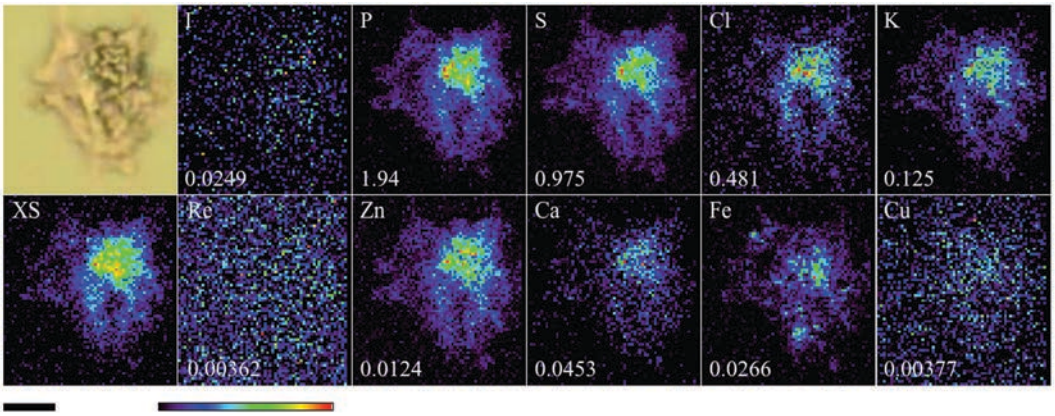

Fig. 1 Optical micrograph (top left), scattered X-ray (XS) and XRF elemental distribution maps of a 22Rv1 control cell. The maximum elemental area densities (quantified from standards and expressed in μg cm^{-2}) are given in the bottom corner of each map. The scale bar represents 10 μm.

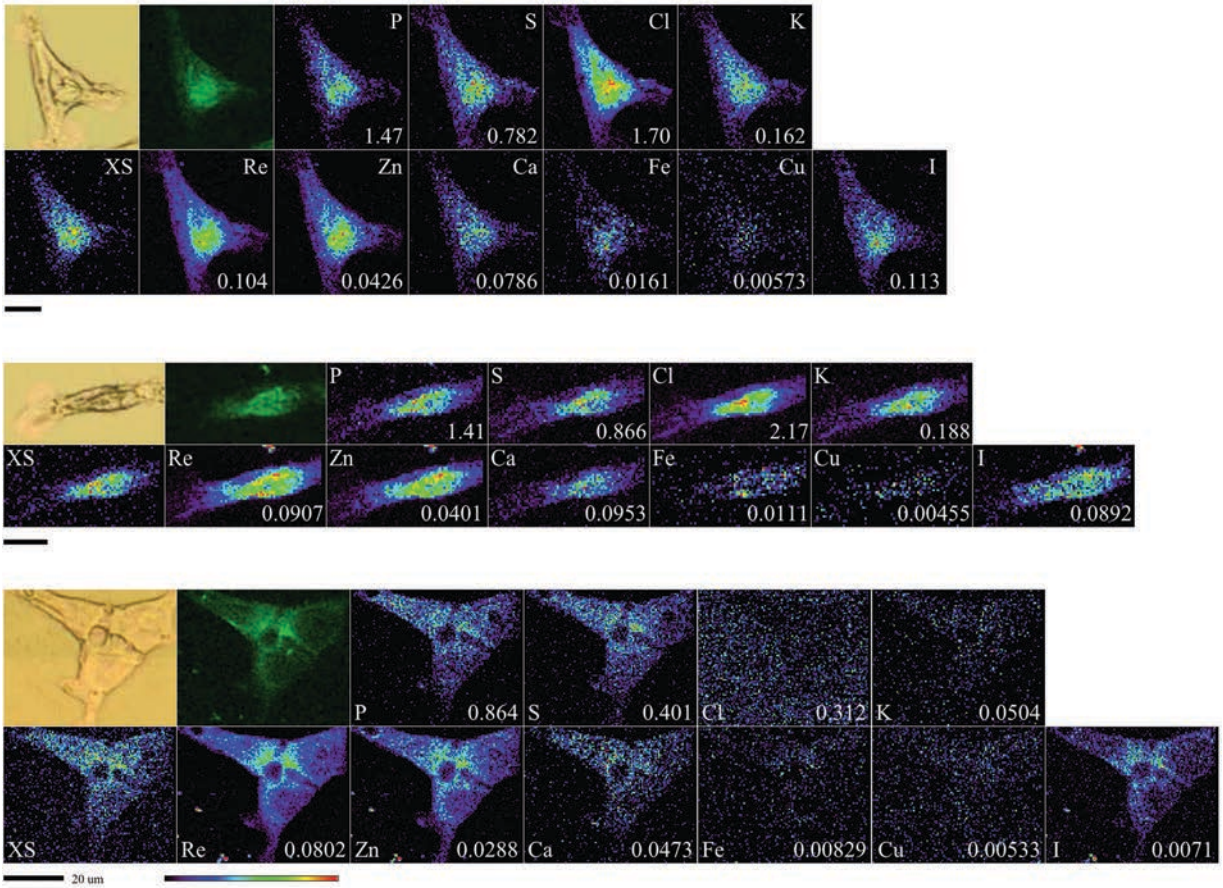

Fig. 2 Optical micrographs (top left), epifluorescence microscopy images (second right, top), scattered X-ray (XS) and XRF elemental distribution maps of 22Rv1 cells treated with **Re–I** for 2 h (top, middle) or 4 h (bottom). The maximum elemental area densities (quantified from standards and expressed in μg cm^{-2}) are given in the bottom corner of each map. The scale bar represents 10 μm unless otherwise indicated.

All cells treated with **Re–I** showed elemental concentrations localised within the cell, with notable exceptions for rhenium, iodine and zinc, which were also occasionally found outside the boundaries of the cell (Fig. 2). The co-localisation of rhenium and iodine, both inside and outside the cells, is consistent with the fact that the tetrazolato ancillary ligand has not dissociated from the rhenium center. The cellular uptake of **Re–I** was evident in high intracellular concentrations of both rhenium and iodine within all treated cells.

The **Re–I** complex appeared to strongly adhere to the silicon nitride windows such that extracellular localisations of rhenium and iodine were visible (Fig. 2). These spots were also fluorescent, identifying them to be from adhered complex, however the co-localisation with zinc is unusual. Zinc, while not contained in **Re–I**, was the only element to be additionally co-localised both within the cell and in the spots where **Re–I** adhered.

The intense regions of the optical fluorescence images were visually similar to the rhenium intracellular distribution from XRF imaging, indicating that the luminescence detected by epifluorescence microscopy was likely to be originating from **Re–I**. Taken together with the similarity of the XRF maps of rhenium and iodine distributions, this supports the interpretation that the complex was still intact at the time of XRF imaging. This is in line with the theory that the low spin d^6 complexes form kinetically stable complexes, even in complex biological systems.

The distribution of **Re–I** in the 22Rv1 cell is consistent with the staining of a diffuse reticular network in the nuclear/perinuclear region; where the nuclear regions of the cells were identified using the P and Zn maps, given the inherently higher concentrations of phosphate from the DNA backbone and Zn from zinc finger proteins within the nucleus.[48] The localisation of **Re–I** is consistent with other previously reported neutral *fac*-[$Re(CO)_3$(phen)T] complexes, where T is an aryltetrazolato ligand. The distribution of **Re–I** does follow the thickness of the cell (Fig. 3) but this is as expected; 22Rv1s are a relatively thin cell where the vast majority of cellular organisation is localised around the nucleus.

Localisation within the diffuse reticular network of the endoplasmic reticulum has been previously reported with other rhenium tetrazolato complexes in live HeLa cells[53] as well as with larger more complex ancillary biomolecules, such as nuclear,[21] peri-nuclear,[15] cytoplasmic[17] and cellular compartments,[14] and some organelle[18] specific distributions, for certain complexes. Three-colour elemental correlation images readily identified strong extracellular colocalisations of rhenium, iodine and zinc for **Re–I** treated cells (Fig. 4).

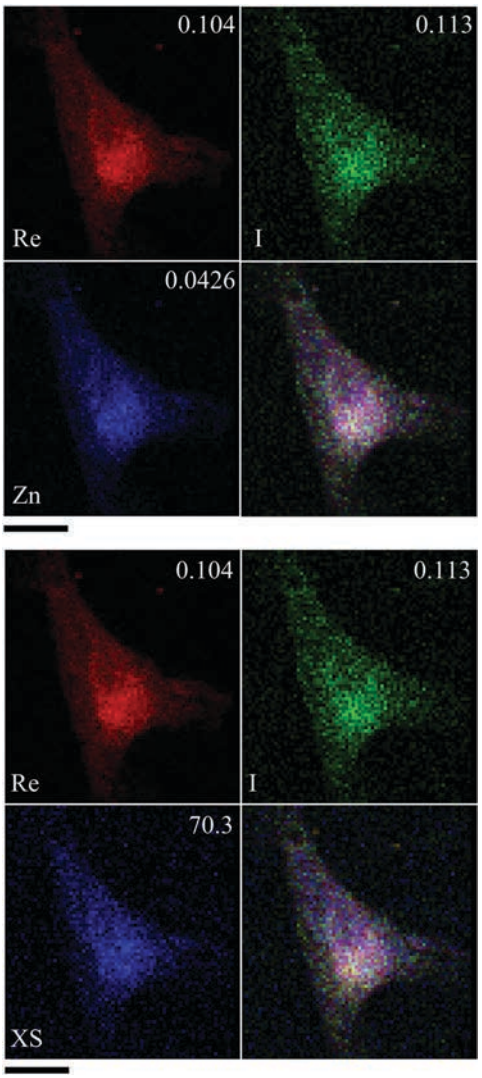

Fig. 3 XRF elemental distribution maps for a 22Rv1 cell incubated with **Re–I** for 2 h showing the colocalisation of rhenium (red), iodine (green) and zinc (blue) (top), cell thickness (blue, XS) (bottom), and the resultant three-colour overlay; where white indicates co-localisation of all three elements. The maximum elemental area densities (quantified from standards and expressed in μg cm^{-2}) are given in the top corner of each map. The scale bar represents 10 μm.

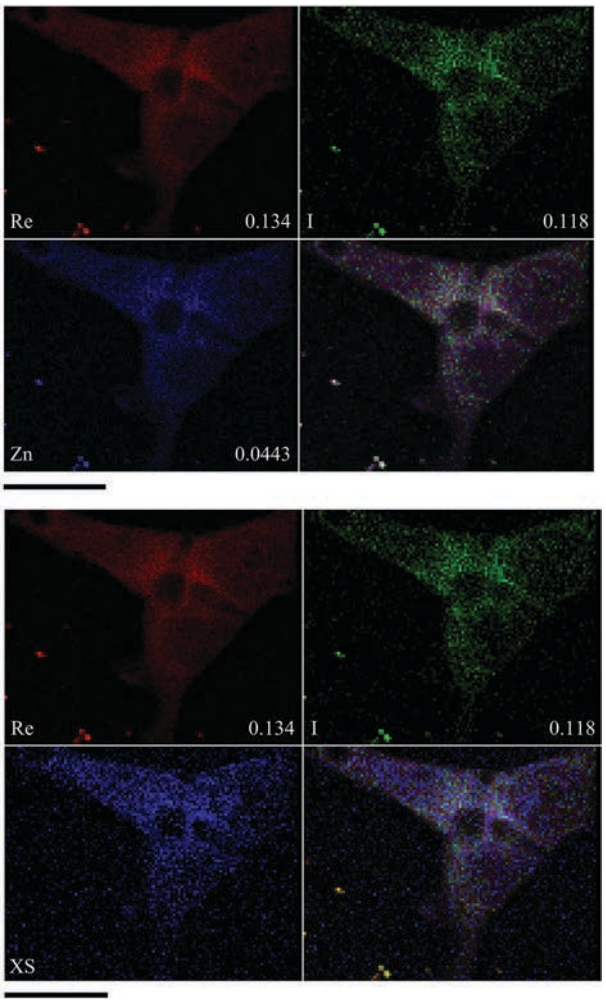

Fig. 4 XRF elemental distribution maps for a 22Rv1 cell incubated with **Re–I** for 4 h showing the colocalisation of rhenium (red), iodine (green) and zinc (blue) (top), cell thickness (blue, XS) (bottom), and the resultant three-colour overlay; where white indicates co-localisation of all three elements. The maximum elemental area densities (quantified from standards and expressed in μg cm^{-2}) is given in the bottom corner of each map. The scale bar represents 20 μm.

From the XRF data the total average rhenium content can be quantified for both the cell as a whole and related to an area designated as nuclear fractions (Fig. 5). The quantitation of cellular elemental content showed a significant increase in both rhenium and iodine concentrations in **Re–I** treated cells compared to untreated controls. Furthermore, the ratio of cell to nuclear content for rhenium is consistent with data that shows **Re–I** preferentially localises to cytoplasmic areas around the nucleus. It should be noted that the quantitation of elemental contents in the nuclear regions of the cell also includes elemental content in over- or underlying structures, *e.g.* the endoplasmic reticulum, because the XRF images are simply two-dimensional projections of (dried) three-dimensional objects. There was no significant increase in intracellular contents of either rhenium or iodine in treated cells between the 2 and 4 h incubation periods, indicating that a 2 h treatment was sufficient to allow maximum uptake. The ratio of the total cellular contents (as masses) for rhenium and iodine were observed to be approximately in concordance with the ratio of their atomic masses and the expected 1 : 1 stoichiometric ratio, again providing some evidence to support the kinetic stability of the complex after cellular uptake.

Homeostasis of some other biologically relevant elements was disrupted by incubation with **Re–I** with significant changes in intracellular content of selenium, chlorine, zinc and potassium. However, not all elements were similarly affected, for example there was a general increase in zinc content for both the 2 and 4 h treatments; whereas potassium only saw significant increases with the 2 h treatment. There are a range of possible causes for disturbance of the homeostasis of these elements, for example in the case of potassium, the complex may transiently

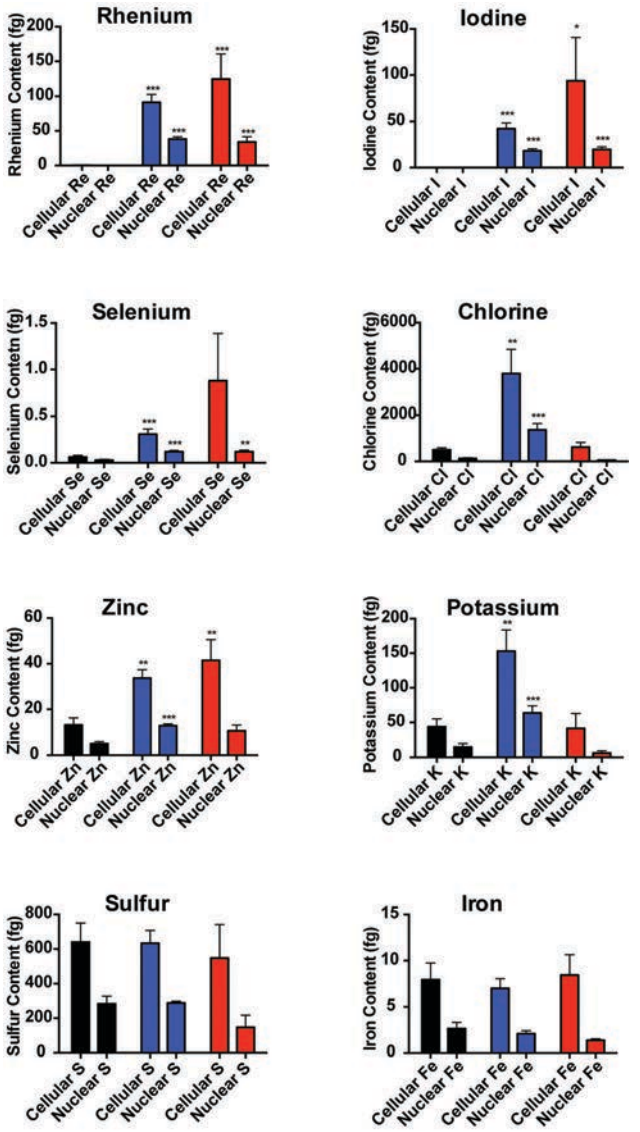

Fig. 5 Intracellular content of rhenium and other biologically relevant elements within 22Rv1 cells treated with fluorescent complex **Re–I** as quantified by XRF studies. Control bars are black, 2 h treatment blue, 4 h treatment red. * Represents $p < 0.1$, ** $p < 0.05$, *** $p < 0.005$ for comparisons between controls and treated cells.

activate Na^+/K^+ ATPase[54] or even inhibit K^+ ion channels;[55] both of these would lead to the observed increase in intracellular potassium contents. However, the data presented herein provide no evidence to support or disprove either of these hypotheses, nor any other, and complementary experiments would be needed to further investigate the topic. Furthermore, some elements saw no significant change to their content levels, such as sulfur and iron. Nonetheless, this approach might provide a very important way of assessing the impact of imaging agents on cells by identifying subtle changes in cellular metabolism/homeostasis, especially when combined with other methodologies which can provide information regarding the mechanisms by which homeostasis is disturbed.

Conclusions

In this study we have demonstrated that the cellular distribution of a novel Re(I) based luminescent imaging agent can be determined by monitoring the luminescence from the compound using optical microscopy and then correlated with the cellular distributions of rhenium and iodine contained in the species within the same samples as measured using microprobe X-ray fluorescence imaging.

The iodinated tetrazolato ancillary group on the complex resulted in a similar cellular distribution within the 22Rv1 cell line to that reported for a related *fac*-[$Re(CO)_3$(phen)T], where T is 5-(pyrid-4-yl)-tetrazolate, which interacts with endoplasmic reticulum. The intracellular distribution of **Re–I** therefore approximately followed the cell thickness producing a diffuse reticular network staining pattern.

The combination of optical microscopy with XRF imaging was able to provide more information beyond just the distribution of the complex. A co-localisation of zinc with the exogenous elements was evident both inside and outside of the cells. Quantitation of cellular elemental contents arising from integrated XRF signals showed that the homeostasis of some biological elements was disrupted by treatment with **Re–I** and that this may be used to identify subtle impacts of imaging agents on cellular homeostasis. The principal conclusion drawn from the XRF imaging study was based on the observation that the distributions of rhenium and iodine were very similar, which indicated that the complex remained intact in the cells after uptake.

Acknowledgements

Financial support for this research was provided by the Australian Research Council Discovery Scheme (DP140100176) and Future Fellowship scheme (FT130100033). We acknowledge travel funding provided by the International Synchrotron Access Program (ISAP) managed by the Australian Synchrotron and funded by the Australian Government. This research used resources of the Advanced Photon Source, a U.S. Department of Energy (DOE) Office of Science User Facility operated for the DOE Office of Science by Argonne National Laboratory (DE-AC02-06CH11357). The authors acknowledge the facilities, and the scientific and technical assistance of the Australian Microscopy & Microanalysis Research Facility at the Centre for Microscopy, Characterisation & Analysis, The University of Western Australia, a facility funded by the University, State and Commonwealth Governments.

References

1 R. G. Balasingham, M. P. Coogan and F. L. Thorp-Greenwood, *Dalton Trans.*, 2011, **40**, 11663–11674.
2 V. Fernandez-Moreira, F. L. Thorp-Greenwood and M. P. Coogan, *Chem. Commun.*, 2010, **46**, 186–202.
3 S. Prakash, M. J. Went and P. J. Blower, *Nucl. Med. Biol.*, 1996, **23**, 543–549.

4 W. A. Volkert and T. J. Hoffman, *Chem. Rev.*, 1999, **99**, 2269–2292.
5 L. H. Wei, J. W. Babich, W. Ouellette and J. Zubieta, *Inorg. Chem.*, 2006, **45**, 3057–3066.
6 A. Carreno, M. Gacitua, J. A. Fuentes, D. Paez-Hernandez, J. P. Penaloza, C. Otero, M. Preite, E. Molins, W. B. Swords, G. J. Meyer, J. M. Manriquez, R. Polanco, I. Chavez and R. Arratia-Perez, *New J. Chem.*, 2016, **40**, 7687–7700.
7 M. P. Coogan and V. Fernandez-Moreira, *Chem. Commun.*, 2014, **50**, 384–399.
8 M. Patra and G. Gasser, *ChemBioChem*, 2012, **13**, 1232–1252.
9 V. Sathish, E. Babu, A. Ramdass, Z. Z. Lu, M. Velayudham, P. Thanasekaran, K. L. Lu and S. Rajagopal, *Talanta*, 2014, **130**, 274–279.
10 S. R. Banerjee, L. H. Wei, M. K. Levadala, N. Lazarova, V. O. Golub, C. J. O'Connor, K. A. Stephenson, J. F. Valliant, J. W. Babich and J. Zubieta, *Inorg. Chem.*, 2002, **41**, 5795–5802.
11 R. Alberto, R. Schibli, R. Waibel, U. Abram and A. P. Schubiger, *Coord. Chem. Rev.*, 1999, **192**, 901–919.
12 S. T. Lam, N. A. Y. Zhu and V. W. W. Yam, *Inorg. Chem.*, 2009, **48**, 9664–9670.
13 K. K. W. Lo, *Acc. Chem. Res.*, 2015, **48**, 2985–2995.
14 A. J. Amoroso, M. P. Coogan, J. E. Dunne, V. Fernandez-Moreira, J. B. Hess, A. J. Hayes, D. Lloyd, C. Millet, S. J. A. Pope and C. Williams, *Chem. Commun.*, 2007, 3066–3068.
15 R. G. Balasingham, F. L. Thorp-Greenwood, C. F. Williams, M. P. Coogan and S. J. A. Pope, *Inorg. Chem.*, 2012, **51**, 1419–1426.
16 C. Y. Li, M. X. Yu, Y. Sun, Y. Q. Wu, C. H. Huang and F. Y. Li, *J. Am. Chem. Soc.*, 2011, **133**, 11231–11239.
17 K. K. W. Lo, A. W. T. Choi and W. H. T. Law, *Dalton Trans.*, 2012, **41**, 6021–6047.
18 E. E. Langdon-Jones, N. O. Symonds, S. E. Yates, A. J. Hayes, D. Lloyd, R. Williams, S. J. Coles, P. N. Horton and S. J. A. Pope, *Inorg. Chem.*, 2014, **53**, 3788–3797.
19 P. Hafliger, N. Agorastos, B. Spingler, O. Georgiev, G. Viola and R. Alberto, *ChemBioChem*, 2005, **6**, 414–421.
20 K. P. Maresca, S. M. Hillier, F. J. Femia, C. N. Zimmerman, M. K. Levadala, S. R. Banerjee, J. Hicks, C. Sundararajan, J. Valliant, J. Zubieta, W. C. Eckelman, J. L. Joyal and J. W. Babich, *Bioconjugate Chem.*, 2009, **20**, 1625–1633.
21 V. Polyakov, V. Sharma, J. L. Dahlheimer, C. M. Pica, G. D. Luker and D. Piwnica-Worms, *Bioconjugate Chem.*, 2000, **11**, 762–771.
22 M. Sagnou, S. Tzanopoulou, C. P. Raptopoulou, V. Psycharis, H. Braband, R. Alberto, I. C. Pirmettis, M. Papadopoulos and M. Pelecanou, *Eur. J. Inorg. Chem.*, 2012, 4279–4286.
23 D. J. Kramer, A. Davison, W. M. Davis and A. G. Jones, *Inorg. Chem.*, 2002, **41**, 6181–6183.
24 T. W. Spradau and J. A. Katzenellenbogen, *Bioconjugate Chem.*, 1998, **9**, 765–772.
25 S. Top, A. Vessieres and G. Jaouen, *J. Chem. Soc., Chem. Commun.*, 1994, 453–454.
26 G. Gasser, I. Ott and N. Metzler-Nolte, *J. Med. Chem.*, 2011, **54**, 3–25.
27 A. El Nahhas, A. Cannizzo, F. van Mourik, A. M. Blanco-Rodriguez, S. Zalis, A. Vlcek and M. Chergui, *J. Phys. Chem. A*, 2010, **114**, 6361–6369.
28 P. J. Giordano and M. S. Wrighton, *J. Am. Chem. Soc.*, 1979, **101**, 2888–2897.
29 T. M. McLean, J. L. Moody, M. R. Waterland and S. G. Telfer, *Inorg. Chem.*, 2012, **51**, 446–455.
30 D. K. Orsa, G. K. Haynes, S. K. Pramanik, M. O. Iwunze, G. E. Greco, D. M. Ho, J. A. Krause, D. A. Hill, R. J. Williams and S. K. Mandal, *Inorg. Chem. Commun.*, 2008, **11**, 1054–1056.
31 R. Schibli and P. A. Schubiger, *Eur. J. Nucl. Med. Mol. Imaging*, 2002, **29**, 1529–1542.
32 R. A. Kirgan, B. P. Sullivan and D. P. Rillema, *Top. Curr. Chem.*, 2007, **281**, 45–100.
33 A. Leonidova and G. Gasser, *ACS Chem. Biol.*, 2014, **9**, 2180–2193.
34 C. A. Bader, R. D. Brooks, Y. S. Ng, A. Sorvina, M. V. Werrett, P. J. Wright, A. G. Anwer, D. A. Brooks, S. Stagni, S. Muzzioli, M. Silberstein, B. W. Skelton, E. M. Goldys, S. E. Plush, T. Shandala and M. Massi, *RSC Adv.*, 2014, **4**, 16345–16351.
35 C. A. Bader, A. Sorvina, P. V. Simpson, P. J. Wright, S. Stagni, S. E. Plush, M. Massi and D. A. Brooks, *FEBS Lett.*, 2016, **590**, 3051.
36 C. A. Bader, E. A. Carter, A. Safitri, P. V. Simpson, P. Wright, S. Stagni, M. Massi, P. A. Lay, D. A. Brooks and S. E. Plush, *Mol. BioSyst.*, 2016, **12**, 2064–2068.
37 C. A. Bader, T. Shandala, E. A. Carter, A. Ivask, T. Guinan, S. M. Hickey, M. V. Werrett, P. J. Wright, P. V. Simpson, S. Stagni, N. H. Voelcker, P. A. Lay, M. Massi, S. E. Plush and D. A. Brooks, *PLoS One*, 2016, **11**, e0161557.
38 K. Koguro, T. Oga, S. Mitsui and R. Orita, *Synthesis*, 1998, 910–914.
39 J. N. Demas and G. A. Crosby, *J. Phys. Chem.*, 1971, **75**, 991–1024.
40 K. Nakamaru, *Bull. Chem. Soc. Jpn.*, 1982, **55**, 2697–2705.
41 J. B. Aitken, S. Antony, C. M. Weekley, B. Lai, L. Spiccia and H. H. Harris, *Metallomics*, 2012, **4**, 1051–1056.
42 E. A. Carter, B. S. Rayner, A. I. McLeod, L. E. Wu, C. P. Marshall, A. Levina, J. B. Aitken, P. K. Witting, B. Lai, Z. H. Cai, S. Vogt, Y. C. Lee, C. I. Chen, M. J. Tobin, H. H. Harris and P. A. Lay, *Mol. Biosyst.*, 2010, **6**, 1316–1322.
43 C. M. Weekley, J. B. Aitken, S. Vogt, L. A. Finney, D. J. Paterson, M. D. de Jonge, D. L. Howard, I. F. Musgrave and H. H. Harris, *Biochemistry*, 2011, **50**, 1641–1650.
44 C. M. Weekley, J. B. Aitken, S. Vogt, L. A. Finney, D. J. Paterson, M. D. de Jonge, D. L. Howard, P. K. Witting, I. F. Musgrave and H. H. Harris, *J. Am. Chem. Soc.*, 2011, **133**, 18272–18279.
45 C. M. Weekley, G. Jeong, M. E. Tierney, F. Hossain, A. M. Maw, A. Shanu, H. H. Harris and P. K. Witting, *J. Biol. Inorg. Chem.*, 2014, **19**, 813–828.
46 C. M. Weekley, A. Shanu, J. B. Aitken, S. Vogt, P. K. Witting and H. H. Harris, *Metallomics*, 2014, **6**, 1602–1615.
47 R. McRae, B. Lai and C. J. Fahrni, *Metallomics*, 2013, **5**, 52–61.
48 R. McRae, B. Lai, S. Vogt and C. J. Fahrni, *J. Struct. Biol.*, 2006, **155**, 22–29.

49 P. Van Espen, Spectrum Evaluation, in *Handbook of X-Ray Spectrometry*, ed. R. E. Van Grieken and A. A. Markowicz, CRC Press, 2nd edn, 2002, vol. 29.
50 S. Vogt, *J. Phys. IV*, 2003, **104**, 635–638.
51 M. V. Werrett, D. Chartrand, J. D. Gale, G. S. Hanan, J. G. MacLellan, M. Massi, S. Muzzioli, P. Raiteri, B. W. Skelton, M. Silberstein and S. Stagni, *Inorg. Chem.*, 2011, **50**, 1229–1241.
52 C. M. Weekley, J. B. Aitken, L. Finney, S. Vogt, P. K. Witting and H. H. Harris, *Nutrients*, 2013, **5**, 1734–1756.
53 M. V. Werrett, P. J. Wright, P. V. Simpson, P. Raiteri, B. W. Skelton, S. Stagni, A. G. Buckley, P. J. Rigby and M. Massi, *Dalton Trans.*, 2015, **44**, 20636–20647.
54 J. H. Kaplan, in *Handbook of ATPases*, ed. M. Futai, Y. Wada and J. H. Kaplan, Wiley-VCH, Weinheim, 2004, pp. 89–97.
55 D. A. Doyle, J. M. Cabral, R. A. Pfuetzner, A. L. Kuo, J. M. Gulbis, S. L. Cohen, B. T. Chait and R. MacKinnon, *Science*, 1998, **280**, 69–77.

CHAPTER 3. Investigation into the intracellular fates, speciation and mode of action of selenium-containing stroke mitigation agents

Jason L. Wedding and Hugh H. Harris*

*School of Physical Sciences, The University of Adelaide, South Australia, 5005, Australia

Chapter 3. Statements of Authorship

Statement of Authorship

Title of Paper	Investigation into the intracellular fates, speciation and mode of action of selenium-containing e agents using XAS and XFM.
Publication Status	☐ Accepted for Publication ☒ Submitted for Publication ☐ Unpublished and Unsubmitted w ork w ritten in manuscript style
Publication Details	Wedding, J. L., Lai, B., Vogt, S., Harris, H. H., *Investigation into the intracellular fates, speciation and mode of action of selenium-containing neuroprotective agents using XAS and XFM*, Biochimica et Biophysica Acta (BBA) - General Subjects, 1862(11), April 2018, DOI: 10.1016/j.bbagen.2018.03.031

Principal Author

Name of Principal Author (Candidate)	Jason Lee Wedding		
Contribution to the Paper	Designed experimental work, carried out all experiments, performed XFM and XAS experiments, analysed data, interpreted data and conceived and prepared manuscripts.		
Overall percentage (%)	60		
Certification:	This paper reports on original research I conducted during the period of my Higher Degree by Research candidature and is not subject to any obligations or contractual agreements with a third party that would constrain its inclusion in this thesis. I am the primary author of this paper.		
Signature		Date	

Co-Author Contributions

By signing the Statement of Authorship, each author certifies that:

i. the candidate's stated contribution to the publication is accurate (as detailed above);
ii. permission is granted for the candidate in include the publication in the thesis; and
iii. the sum of all co-author contributions is equal to 100% less the candidate's stated contribution.

Name of Co-Author	Barry Lai		
Contribution to the Paper	Assisted with the acquisition of XFM data and subsequent analysis.		
Signature		Date	Jan. 21, 2019

Name of Co-Author	Stefan Vogt		
Contribution to the Paper	Assisted with the acquisition of XFM data and subsequent analysis.		
Signature		Date	2/2/2019

Name of Co-Author	Hugh Harris		
Contribution to the Paper	Supervised the development of the work, assisted with the acquisition of XAS data, assisted with the conception and revision of the manuscript and acted as a corresponding author.		
Signature		Date	11/02/2019

3.1 Abstract

Bis(2-aminophenyl)diselenide was shown to protect against oxidative stress conditions which mimic ischemic strokes, while its nitro analogue, bis(2-nitrophenyl)diselenide did not. This protective activity was tentatively assigned to the reductive cleavage of bis(2-aminophenyl)diselenide inside human neurocarcinoma cells, SH-SY5Y, while bis(2-nitrophenyl)diselenide remained unchanged. The distinct chemistries of the related compounds were traced by the changes in selenium speciation in bulk pellets of treated SH-SY5Y cells detected by X-ray absorption spectroscopy. Further, bis(2-aminophenyl)diselenide, like the known stroke mitigation agent Ebselen, was observed by X-ray fluorescence imaging to penetrate into the nucleus of SH-SY5Y cells while bis(2-nitrophenyl)diselenide was observed to be excluded from the nuclear region. The differences in activity were thus attributed to the varied speciation and localisations of the drugs, or their metabolites, as detected by X-ray absorption spectroscopy and X-ray fluorescence microscopy.

3.2 Abbreviations

Am-DPDS	bis(2-aminophenyl)diselenide;
Cys	cysteine;
CysSeSeCys	selenocysteine;
CysSeSCys	sulfoselenocysteine;
DPDS	diphenyl diselenide;
Eb	Ebselen;
EXAFS	extended X-ray absorption fine structure;
GPx	glutathione peroxidase;
GSH	glutathione;
GSSeSG	seleno-diglutathione;
MSC	methylselenocysteine;
Ni-DPDS	bis(2-nitrophenyl)diselenide;
ROS	reactive oxygen species;
SeCys	selenocysteine;
SeMet	ʟ-selenomethionine;
XANES	X-ray absorption near edge structure;
XAS	X-ray absorption spectroscopy;
XFM	X-ray fluorescence microscopy;

3.3 Introduction

3.3.1 Ischaemia

Strokes are one of the leading causes of death in the developed world,[1-4] as well as a leading cause of long term disability, and as such continues to be a target of clinical research[5]. While neuroprotective agents continue to make it through phase III clinical trials, most are ultimately rejected due to ineffectiveness or unacceptable toxicity.[5]

Ischaemic strokes occur due to the abrupt interruption or extreme reduction of blood flow and oxygen in cerebral arteries and account for 80-85% of all stroke cases.[2,4-6] Ischaemia affects neurons by ATP depletion due to disrupted energy production, glutamine-mediated toxicity, Na^+ and Ca^+ influx, mitochondrial failure and finally cell death (Scheme 3.3.1).[6,7] Apoptosis is also a known consequence of prolonged ischaemia as oxidative stress conditions develop as lactic acid builds up due to energy depletion leading to acidosis and thus pro-oxidant conditions.[2,6,7]

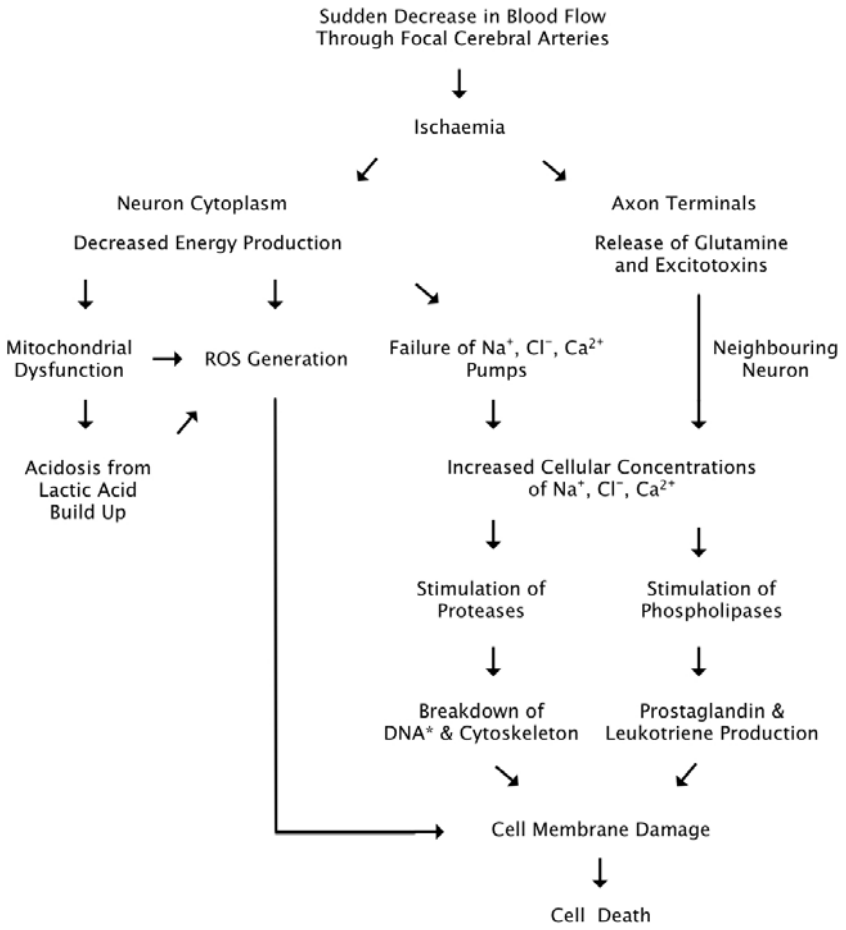

Scheme 3.3.1 - Intracellular cascade in neurons as a result of ischaemic conditions that leads to cell death.

Neurons under oxidative stress are subjected to excessive levels of molecular oxygen and its chemical derivatives (ROS).[2] Reactive oxygen species are known to be linked to ageing and disease pathogenesis.[2,8] The brain has an increased susceptibility to ROS–induced damage due to its high lipid content, low native antioxidant concentrations, high oxygen consumption and high iron levels.[2,3] During ischaemic conditions, ROS cause multi-pronged damage; including lipid peroxidation, protein denaturation, DNA modifications, and disruption of redox-sensitive transduction pathways.[2,3,9]

3.3.2 Antioxidant defences

An antioxidant is a substance that exhibits the property of dampening, quenching or removing oxidative damage.[10-12] The requirement for such activity is that the substance itself should be targeted by the ROS, leaving more valuable targets such as lipids, enzymes or DNA unscathed, while also producing a less reactive product unable to perpetuate the intracellular cascade.[10]

Biological antioxidant defences consist of two types; non-enzymatic antioxidants, such as GSH, vitamin C and vitamin E, as well as enzymatic antioxidants, including superoxide dismutase (SOD), catalase (COD) and glutathione peroxidase (GPx). The exact antioxidant defence's effectiveness and composition depends on the tissue type as well as the cell type.[10-13]

3.3.3 Therapeutic antioxidants

Interest in the protective activity of organoselenium compounds has increased since the 1980s, when it was shown that Ebselen was an antioxidant mimic for the selenoenzyme glutathione peroxidase (GPx).[14] The neuroprotective effects of Ebselen in rodent models of ischemia allowed it to be used in clinical trials for the treatment of neurological diseases linked with ischemia and thus oxidative stress.[15-17]

Ebselen's discovery and success led to the development of other organoselenium compounds designed to mimic GPx activity. These incorporate a selenium atom within an organic framework to produce a redox sensitive compound. Successful antioxidant compounds would thus catalytically increase the rate of reduction of the ROS and so enhance the effects of endogenous antioxidants within the cells. By mimicking the GPx catalytic activity, only small concentrations would be required to exert significant effects as they are not consumed by the reduction reaction.[11,18-21]

3.3.4 Ebselen

Ebselen has attracted interest as a glutathione peroxidase mimic, and has been shown to be capable of contributing to the antioxidant defence in tissues.[22] Ebselen is a potent scavenger of hydrogen peroxide, membrane bound phospholipids and cholesterylester hydroperoxides which result from ischaemic conditions.[22] The selenium within Ebselen is not bioavailable for incorporation into selenoproteins (GPx activity could not be salvaged by supplementation with Ebselen, unlike selenite, in Se-deficient animals[23,24]), which is thought to be the reason for its lack of toxicity[22], instead showing anti-inflammatory capabilities[25].

Despite the clinical trial successes of Ebselen, there is debate over the mode of action for its neuroprotective effects.[26,27] While Ebselen's intracellular interactions with organic thiols, such as glutathione, are known to be key components of its activity, the exact nature of the glutathione peroxidase activity is unproven. The involvement of diselenide and selenol forms of Ebselen after reaction with organic thiols has been posited with a focus given to the selenol (Scheme 3.3.2).[26-28]

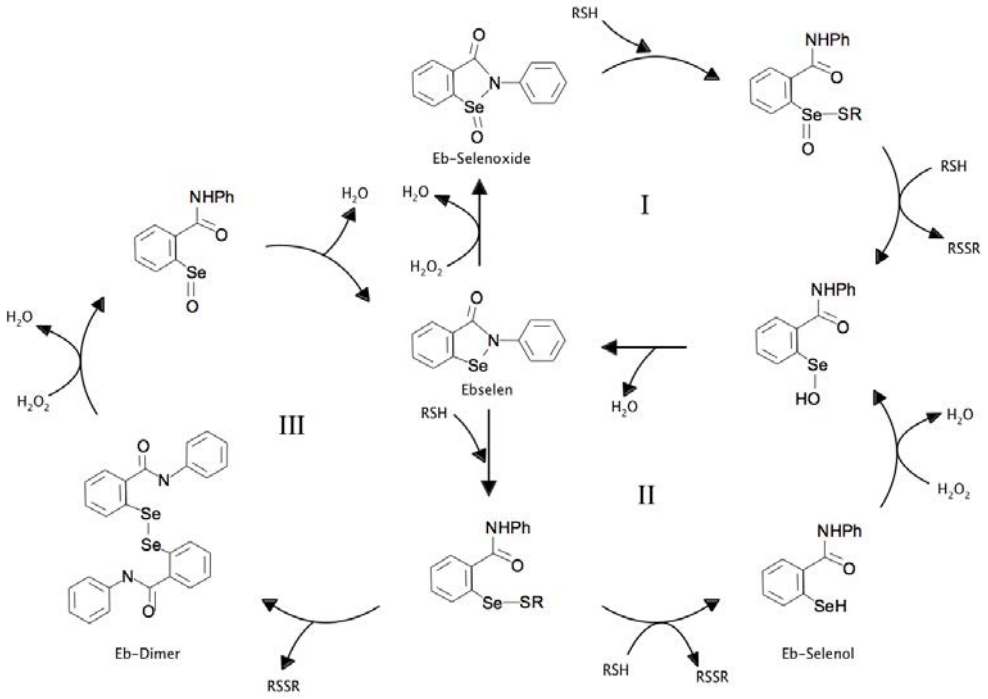

Scheme 3.3.2 - Summary of different proposed modes of action for Ebselen's glutathione peroxidase activity reacting with both hydrogen peroxide and organic thiols such as glutathione (RSH).

While a multitude of different schemes have been proposed[27,29,30], the three shown in Scheme 3.3.2 have garnered the most interest. Cycle I features the involvement of a selenoxide form of Ebselen (Eb-Selenoxide, Scheme 3.3.2)[31] which is now generally regarded not to be involved with the mode of action.[27] This catalytic reduction of hydroperoxides is in the presence of thiol is independent of the popular Ebselen selenol intermediate. This cycle is dependent on low thiol concentrations and high levels of hydrogen peroxide, which is not representative of conditions within biological systems.

Cycle II involves the selenol form of Ebselen[23,32] and has garnered recent support and features a mode of action kinetically similar to glutathione peroxidase enzyme activity in solution[25,27,32,33], while cycle III features the involvement of an Ebselen dimer[26,27]. Unlike cycle I, these schemes (cycle II and III) are dependent on excess thiol levels and low hydrogen peroxide concentrations which are more biologically consistent.[27]

3.3.5 Diphenyl diselenide

Subsequent to the discovery of Ebselen's GPx activity, diphenyl diselenide (DPDS) was reported to have an even greater GPx mimetic activity.[34] DPDS has since exhibited similar antioxidant capabilities, specifically, it reduces cerebral, renal, pulmonary and hepatic oxidative stress in mice[35-38], as well as reducing cerebral and renal oxidative stress induced in rats[39-41]. More generally it has been found to have anti-inflammatory and antinociceptive activity[42] and can prevent gastric lesions[43] and mitochondrial dysfunction[44]. Conversely, it is known to display toxicity at relatively high levels; although the exact threshold where toxicity manifests remains unknown.[45,46] DPDS is known to be less toxic than Ebselen, which is commonly used as a comparison given Ebselen's low toxicity and use in clinical trials.[36,45,47] Animals tested with DPDS were either administered it orally, dissolved in either soy-bean or canola oil, or the DPDS was dissolved in DMSO and administered subcutaneously.

3.3.6 Experimental Aims

The aim of this study was to investigate the neuroprotective action of DPDS *in vitro* against oxidative stress-induced damage, and using synchrotron techniques to probe the possible molecular basis of this protective action. DPDS is not water soluble, and thus is incompatible with cell-culture-based experiments. Instead, the ability of two more aqueous soluble analogues of DPDS, bis(2-aminophenyl)diselenide (Am-DPDS) and bis(2-nitrophenyl)diselenide (Ni-DPDS) (Scheme 3.3.3), to protect against oxidative

stress-induced damage in human neurocarcinoma (SH-SY5Y) cells will be directly investigated.

Ebselen Ni-DPDS Am-DPDS DPDS

Scheme 3.3.3 - Selenium containing compounds, alongside the parent compound diphenyl diselenide (DPDS), which will be used in cell-based studies to elucidate any neuroprotective action.

Bis(2-aminophenyl)diselenide has been previously used in aqueous experiments in the place of DPDS[48], while its nitro analogue has a similarly comparable structure to DPDS. The results of this study using the two analogues will then be compared to that of Ebselen, with the aim of elucidating the mode of action of all the three compounds within the brain and other tissues under stress.

3.3.7 Synchrotron techniques

The well-established synchrotron-based techniques for exploring local structure, electronic environments and distribution of intracellular species[49,50], X-ray Absorption Spectroscopy (XAS) and X-ray Fluorescence Microscopy (XFM), will be employed to investigate the intracellular fates of the three selenium-containing stroke mitigation agents. XAS has developed into an invaluable tool to characterize the structure of metal binding sites in metalloproteins.[51,52] XAS has been used to probe the speciation and distribution of selenium metabolites in cancer cells, as well as track changes in intracellular selenium speciation over time.[53] XAS has been employed to provide structural information of adsorbed selenium species at water-oxide junctions[54], and wider-reaching XAS has been used to investigate selenium speciation within soil samples[50].

3.3.7.1 X-ray absorption spectroscopy

XAS can provide information on the bulk properties of selenium in a cell sample; simplified by the fact that selenium in non-treated cells is at extremely low native basal levels (generally below the detection limit of the technique). XAS requires minimal sample preparation, unlike other selenium separation and characterization techniques

which may alter speciation.[55] XAS is divided into two sub-regions; X-Ray absorption near-edge structure (XANES) which provides information about oxidation state and geometry and extended X-ray absorption fine structure (EXAFS) which provides metrical information about absorber atom ligation.[56]

XANES provides information about the electronic environment of an absorber atom from comparison of the resultant unknown spectrum to spectra of known reference samples. The technique is highly sensitive to oxidation states and can provide a high level of speciation data but requires careful selection of the possible reference spectra to fully elucidate the speciation within a sample. When the absorbing atom is present in the sample in multiple forms, the XANES spectrum can be represented by the weighted addition of spectra of suitable reference samples to provide information about the relative abundance of different chemical forms within the sample.[57]

EXAFS is an excellent tool to determine the structure of the environment surrounding the absorber atom.[57] It has become a standard method for probing metal binding sites within metalloproteins, and can provide structural information when typical crystallography is impossible such as for reaction intermediates of catalysis.[57] However the EXAFS signal is far weaker than the XANES leading to a higher detection limit, EXAFS can struggle to resolve bonds at similar distances (in practice a resolution of ~0.1 Å is common), carries an uncertainty of ~20% in determination of the coordination number and an inability to distinguish different neighbouring atoms of similar size, such as S and Cl.[58] Thus information resulting from EXAFS analysis is frequently used in conjunction with the XANES finding to provide a stronger overall picture of the speciation. Structural information is extracted from the EXAFS signal by constructing a theoretical signal for expected coordination environments, which is subsequently compared to the actual experimental signal. The nature of the neighbouring structures are often initially constructed from interpretation of the XANES results, and optimized until a close fit between the experimental and theorized signals is achieved.[57]

3.3.7.2 X-ray fluorescence microscopy

XFM allows for the mapping of trace element distribution in biological samples at the (sub)cellular scale.[56] Targeted cells are scanned through the X-ray beam, with the resultant fluorescence collected at discreet points to produce pixels. The spectrum at each point is then fitted and calibrated against measure standards to produce elemental

maps for each excited element. Fortunately the excitation required for selenium fluorescence also excites other biologically relevant elements such that maps for Se, P, S, Ca, Zn, and Fe are all produced concurrently. XFM has been used to trace selenium distribution changes in healthy and diseased mouse kidneys[59,60], as well as the uptake and distribution of selenoamino acids in human lung cancer cells[61].

3.4 Materials & Methodology

3.4.1 Materials

Ebselen was used as purchased from Sigma-Aldrich, Sydney, NSW, Australia. Bis(2-aminophenyl)diselenide was used as purchased from BOC Scientific, Shirley, NY, USA. Bis-(2-nitrophenyl)diselenide was used as purchased from ACROS Organics, Geel, Antwerp, Belgium. Hydrogen peroxide (30%) was sourced from Ajax Finechem (part of Thermo Fischer Scientific, Green Fields, SA, Australia).

3.4.2 Cell culture

SH-SY5Y human neuroblastoma cells, originally purchased from the American Tissue Culture Collection, were cultured as monolayers in complete Dulbecco's Modified Eagle's Medium (DMEM; Gibco) supplemented with foetal bovine serum (5% v/v; Bovogen Biologicals), L-glutamine (2 mM), antibiotic-antimyotic mixture (100 mg.mL-1 penicillin and 100 $U.mL^{-1}$ streptomycin; Sigma Life Sciences) and non-essential amino acids (100 $U.mL^{-1}$; Sigma Life Sciences) at 310 K in a 5% CO_2-humidified incubator and were sub-cultured every 4-6 days.

3.4.3 Treatment solutions

Solutions of the selenium-containing compounds were prepared by initial solvation in DMSO (1 mL; Chem-Supply) before being made up to a 1000 μM solution in complete media. For the drug alone studies these solutions were then serially diluted in complete media to between 1 and 750 μM (<2% DMSO in final media).

Additional selenium-containing agent treatment solutions for the oxidative stress condition studies were made separately; Ebselen treatment solutions were then prepared by dilution with complete media to 10 μM (0.03% DMSO). Treatment solutions of bis(2-aminophenyl)diselenide and bis(2-nitrophenyl)diselenide were prepared by dilution with complete media to 5 μM (0.09% DMSO). Oxidative stress-inducing solutions of hydrogen peroxide were prepared by serial dilution of peroxide in serum-reduced (2% FCS) DMEM media.

3.4.4 Cell fixation solutions

Paraformaldehyde (Sigma Aldrich, 95%) was dissolved on the day of use in phosphate buffered saline (PBS) to prepare a 10% w/v solution. The pH was adjusted to 7.4 using 0.1 M NaOH and 0.1 M HCl with the aid of a pH meter. Then a subsequent 3.7% w/v

paraformaldehyde solution was prepared by diluting with PBS buffer solution. Ammonium acetate (0.1 M, isotonic) solution was prepared by dissolving ammonium acetate in Milli-Q water.

3.4.5 Cytotoxicity assays

3.4.5.1 Drug alone studies

Cell viability was assessed using the MTT (3-(4,5 dimethylthiazol-2-yl)-2,5-diphenyltetrazolium bromide) assay.[62,63] Briefly, cells were seeded at a density of 2 x 10^5 cells per well in a 96-well plate for 24 h at 310 K in a 5% CO_2-humidified incubator. Cells were then pre-treated with aforementioned selenium-containing solutions (<0.5% DMSO), or vehicle-only control (0.5% DMSO), for 24 hours.

After treatment, the cells were incubated with MTT solution (0.25 $mg.mL^{-1}$ in serum free DMEM) for 3 hours. The MTT solution was finally replaced with DMSO (100uL) and the formation of the formazan was measured at 560 nm using a microplate spectrophotometer (BMG Lab Tach Fluostar Galaxy). Cell viability was reported as a percentage absorbance relative to the control as a mean of pooled data from 4-10 individual experiments (with 16-24 replicates per experiment), with outliers being identified and removed using the ROUT test (Q=1.000%).[64] IC_{50} values were determined by curve-fitting plots of cell viability against the log of selenium-containing compound concentration.

3.4.5.2 Oxidative stress condition studies

To test the protection afforded by the three selenium-containing compounds activity against oxidative stress insult, the previous method (Method 3.4.5.1) was repeated with selenium-containing compound concentrations of 5 μM for diselenides, 10 μM for Ebselen and 0.5% DMSO as a control; followed by 24 hour hydrogen peroxide-induced oxidative stress. Solutions of hydrogen peroxide (stock 29% w/v[*]) were prepared by serial dilution in complete media. The selenium-compound containing solutions were then replaced after 24 hours with the hydrogen peroxide solutions to instigate oxidative stress conditions for a further 24 hours. Cell viability was subsequently assessed using the MTT assay as described previously (Method 2.2.5.1).

[*] The concentration of hydrogen peroxide in solution was determined by titration against a potassium permanganate solution standardized against sodium oxalate as the mean of three consistent titer values.[65]

3.4.6 Sample preparation

Bulk cell pellets from treated cultures were prepared for X-ray absorption spectroscopy by growing over 4 days to ~80% confluence in 75 mL culture flasks in complete DMEM. Cells were then pre-treated with 5 μM bis-(2-amino-diphenyl)-diselenide and bis-(2-nitro-diphenyl)-diselenide, or 10 μM Ebselen for 24 hr or DMSO as a vehicle-only control. Oxidative stress conditions were induced by treatment with hydrogen peroxide for 24 hr. Cell pellets were subsequently isolated by light scraping with a cell lifter and centrifugation (600 g). The supernatant was removed and the cells rinsed by re-suspension in PBS (3 x 5 mL) and centrifugation before the pellet was vacuum-dried for 24 hours.

Cells were prepared for XRF imaging by growth on 1.5 x 1.5 mm x 500 nm silicon nitride windows (Silson, UK) in 6-well plates as described previously.[53,61,66-69] The plates were seeded at 2 x 10^5 cells/well in complete DMEM and were incubated at 310 K in a 5% CO_2-humidified incubator for 24 hr prior to treatment. Cells were then pre-treated with 5 μM bis(2-aminophenyl)diselenide and bis(2-nitrophenyl)diselenide, or 10 μM Ebselen for 24 hr or DMSO (0.5%) as a vehicle-only control. At the end of the treatment time the medium was removed and cells were fixed with 3.7% paraformaldehyde (prepared fresh in PBS) solution for 15 min. Fixed windows were then washed with PBS, ammonium acetate (in Milli-Q water) and Milli-Q water thrice. (Procedure adapted from 70-72)

3.4.7 XAS data collection

Selenium K-edge X-ray absorption spectra were recorded at the Australian Synchrotron (AS), Victoria, Australia on beamline XAS using a double-crystal Si(111) monochromator. Harmonic rejection was achieved by setting the cut-off energy of a harmonic rejection mirror to 15 keV. The AS storage ring electron beam energy was 3 GeV with a current of 160-200 mA.

Cell pellets were compressed to approximately 4 mm in diameter and sealed in kapton tape and cooled to ~10 K in a He expansion cryostat. Spectra of the samples were recorded in fluorescence mode on a 100-element solid-state Ge fluorescence detector array at 90° to the incident beam. The energy ranges used for XANES Se-edge data collection were: pre-edge region 12430-12635 eV (10 eV steps); XANES region 12635-12685 eV (0.25 eV steps); post-edge region 12685-12875 eV. EXAFS Se-edge spectra

were collected at the following energy ranges: pre-edge region 12430-12635 eV (10 eV steps); XANES region 12635-12685 eV (0.25 eV steps); and the EXAFS region 12685-13445 eV (0.035 $Å^{-1}$ steps to k = 14 $Å^{-1}$).

A spectrum of a hexagonal selenium standard, recorded simultaneously in transmission downstream of the sample, was used to calibrate the energy scale to the first peak of the first derivative of the elemental selenium edge (12658.0 eV).

3.4.8 XAS data analysis

Calibration, averaging and background subtraction of all spectra as well as subsequent principle component, target transformation and multiple linear regression analyses of XANES spectra were performed using the EXAFSPAK software package (G. N. George, SSRL). Spectra of model selenium compounds for target analysis and XANES linear combination fitting were provided by G. N. George (University of Saskatchewan) except for MeSeCys, which was provided by C. Weekley (obtained as a 5 mM aqueous frozen solution). Spectra of bis(2-nitrophenyl)diselenide and bis(2-aminophenyl)diselenide, were recorded at the Australian Synchrotron. XAS of all selenium-containing treatment compounds were either measured solubilized (to 2 mM) in Milli-Q water (0.5% DMSO) using *N*-cetylpyridinium chloride (CPC) (12 mM), or as homogenous solids (2-3 mg) in cellulose matrix (1 g) compacted into a disc. Solutions of the selenium-containing compounds in CPC were then chemically reduced through the addition of a five times excess of dithionite, and spectra recorded at the Australian Synchrotron XAS beamline. Multiple-scattering fits of EXAFS data were performed using EXAFSPAK, including the FEFF7 code.[57]

3.4.9 XFM data collection

XRF elemental distribution maps of single cells were recorded on beamline 2-ID-D at the Advanced Photon Source (APS), Argonne National Laboratory, Illinois, USA. At the APS, the beam was tuned to an incident energy of 12.7 keV using a beam splitting Si(220) monochromator and was focused to a diameter of 1 μm using a “high-flux” zone plate. A single element silicon drift energy dispersive detector (Vortex EX, SII Nano- technology, Northridge, CA), at 90^{o} to the incident beam, was used to collect the fluorescence signal for 1 s per spatial point from samples under a He atmosphere.

Four to eight individual cells per sample were selected and located using an optical microscope (Leica DMRXE). Cells were subsequently relocated in the beamline by

correlating the light microscope coordinates with those determined from the X-ray transmission image of the window as viewed on a CCD camera. Whole cells were raster scanned using a 25-nm accuracy Newport sample positioning stage. Low resolution scans with a step size of 4 μm and a dwell time of 0.5 s were used to accurately locate the cells before obtaining high-resolution scans with a step size of 1 μm and a per-pixel dwell time of 1 s.

3.4.10 XFM data analysis

The fluorescence spectrum at each spatial point was fit to Gaussians, modified by the addition of a step function and a tailing function to describe mostly incomplete charge collection and other detector artefacts.[73,74] The integrated fluorescence spectra extracted from these regions were also fit with modified Gaussians to determine average elemental area densities (in units of μg cm^{-2}). Quantification was performed by comparison to the corresponding measurements on the thin-film standards NBS-1832 and NBS-1833 from the National Bureau of Standards (Gaithersburg, MD). The analysis was performed using MAPS software.[53,61,66,73]

Statistical analysis of quantified elemental content was carried out by calculating the mean, standard deviation and standard error of the mean for each element separately; then unpaired, two-tailed t-tests on the raw data were carried out assuming a Gaussian distribution and run with 95% confidence interval.

3.5 Results & Discussion

3.5.1 Cytotoxicity studies

3.5.1.1 Drug alone cytotoxicity studies

Cytotoxicity assays are a common feature of pharmacology and measure the effect of a treatment on the growth of a population of cells. Methyl thiazolyldiphenyl tetrazolium (MTT) acts as an indirect measure of cell number. MTT has been employed since the 1980s and is a rapid screening technique that allows for a large throughput of assays in one batch.[62,63] The MTT is a yellow aqueous dye that is reduced inside living cells to form a purple formazan product, which is insoluble in water. The formation of the formazan product can be monitored by spectrometry and is proportional to the number of viable cells.

Cytotoxicity assays were carried out on the three selenium-based compounds to determine their respective cytotoxicity towards the SH-SY5Y cell line, and to verify that the diselenide compounds have similar cytotoxicity profiles to the known drug Ebselen. It is important to understand the cytotoxicity of the drugs to get an appropriate treatment concentration window for the oxidative stress condition studies, such that uptake of the selenium drug has been achieved, but excessive cell death is avoided.

While the cytotoxicity for both Am-DPDS (11±1 μM) and Ni-DPDS (23±1 μM) have an IC_{50} value an order of magnitude lower than that of Ebselen (360±20 μM), all three are in the μM range marking them as moderately cytotoxic (Figure 3.5.1).[11]

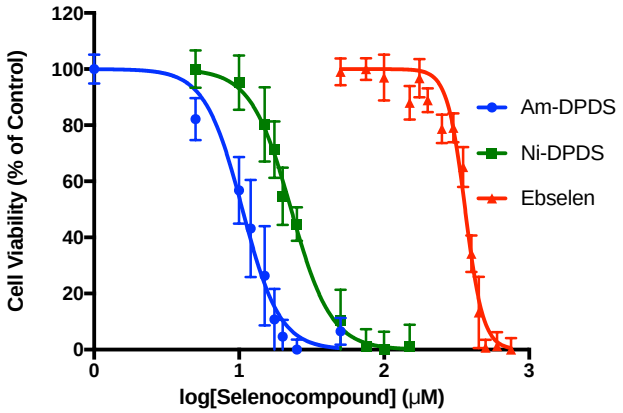

Figure 3.5.1 - Cell Viabilities of SH-SY5Y cells treated with Am-DPDS, Ni-DPDS or Ebselen for 24 hours as determined by MTT assay. Each point represents the mean of several (4-10) repeat experiments (of 16-24 replicates) and the error bars represent the standard error in the mean.

Sigmoidal dose-response curves $\left(y = bottom + \frac{top-bottom}{1+10^{(logIC_{50}-x)\times Hill\ Coefficient}}\right)$ were fit to all data sets. 'LogIC$_{50}$' is the x value when the response is halfway between 'Bottom' and 'Top' plateaus. The 'Hill Coefficient' describes the steepness of the curve. A standard sigmoid dose-response curve has a Hill Slope of 1.0. Interestingly the IC$_{50}$ values for the two diselenides differ significantly, despite only varying in the nitrogen functional groups.

Furthermore, unlike the previous studies that investigated the toxicities of Ebselen and DPDS in mice and rats which found that Ebselen was less toxic than DPDS[36,42], the converse was observed. It should be noted, however, that these aforementioned studies found that many factors impact on the observed relative toxicities. The two major factors were the species of the treated animal, mouse or rat, and the treatment technique, intraperitoneal or subcutaneous. These two factors resulted in very different toxicity patterns, with the LD$_{50}$ varying from 210 to 1200 μmol/kg for DPDS in mice and rats respectively for DPDS and 400 to 340 μmol/kg for Ebselen likewise in mice and rats. The aforementioned LD$_{50}$ values were for the intrapertioneal method, subcutaneous administration resulted in LD$_{50}$ values over 500 μmol/kg. Ultimately given the administration of the selenium-containing agents directly into the growth media and the use of a human cell-line, the results of the DPDS analogues being more cytotoxic than Ebselen is not without precedent.

3.5.1.2 Oxidative Stress Condition Studies

Cytotoxicity assays were again used to investigate if any of the three stroke mitigation drugs showed any protective effect against oxidative stress induced damage due to hydrogen peroxide insult. Oxidative stress conditions were modelled through addition of hydrogen peroxide into the SH-SY5Y cell growth media as hydrogen peroxide is known to crudely mimic oxidative stress conditions, stimulating radical and superoxide production within cell culture.[48,75-77] As a result, hydrogen peroxide insult is widely used to investigate cellular response to ROS insult as well as to assess the protection afforded by antioxidants.[11,78-80] Hydrogen peroxide ultimately causes cell death by apoptosis, or regulated cell death.[81-85]

For subsequent oxidative stress studies a pre-treatment selenocompound concentration of 5 μM was chosen as it is less than half the IC$_{50}$ for Am-DPDS, and a quarter of the IC$_{50}$ for Ni-DPDS. A pre-treatment concentration of 10 μM for Ebselen was chosen due

to past studies displaying cellular uptake at that concentration.[86] Treatment at these three levels showed no discernable cellular morphological changes after 24 hr.

Originally, a 10 µM pre-treatment concentration was trailed for Ni-DPDS (half IC_{50} value), however this concentration caused morphological changes after 24 hours and the cells partially lost adherence which inhibited the subsequent studies involving the addition of hydrogen peroxide.

Am-DPDS showed protective action (Figure 3.5.2), delaying the onset of cell death (blue line) compared to the control that had no pre-treatment (black dashed line). Furthermore, the IC_{50} value associated with peroxide exposure after Am-DPDS pre-treatment was increased from 1742±29 µM for the control to 2385±103 µM (Table 3.3.1). In spite of the structural similarities, the nitro analogue did not exhibit any protective action (green line). Ebselen, a known stroke mitigation agent notwithstanding, failed to display protective effects under the test conditions, instead treatment with Ebselen caused apparent earlier onset of cell death (Figure 3.5.2, red line).

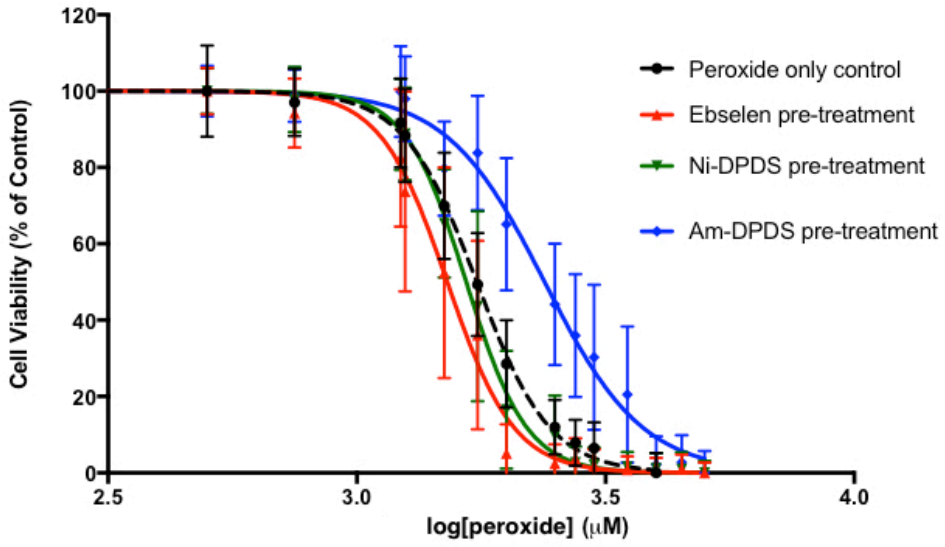

Figure 3.5.2 - Cell Viabilities of SH-SY5Y cells pre-treated with 5 µM Am-DPDS, 5 µM Ni-DPDS or 10 µM Ebselen for 24 hours prior to insult with varying concentrations of hydrogen peroxide for 24 hours as determined by MTT assay. Each point represents the mean of several (4-10) repeat experiments (of 16-24 replicates) and the error bars represent the standard error in the mean. Sigmoidal dose-response curves $\left(y = bottom + \frac{top-bottom}{1+10^{(logIC_{50}-x)\times Hill\ Coefficient}}\right)$ were fit to all data sets.

Table 3.5.1 - IC_{50} values for the cytotoxicity of hydrogen peroxide induced oxidative stress conditions on SH-SY5Y and the effects of initial pre-treatment with Ebselen, Ni-DPDS and Am-DPDS.

	Pre-Treatment Compound			
	None (0.5% DMSO)	Ebselen	Ni-DPDS	Am-DPDS
IC50 (µM)	1742 ± 29	1520 ± 50	1660 ± 29	2385 ± 108

The IC_{50} value determined for the hydrogen peroxide treatment alone is notably higher than that found for similar studies which treated with hydrogen peroxide for 24 hours (Table 3.5.1). Previous values of 100 µM[87] and 150 µM[88] were a factor of ten lower than the recorded value. These variations, while significant, are not without precedent. Other studies have found that hydrogen peroxide cytotoxicity is linked to both cell density and treatment duration.[11,79,80]

In this study the cells were initially seeded at a higher 2 x 10^5 per well density than was used in other studies. This was compounded by the fact the hydrogen peroxide insult came 24 hours after this seeding due to the pre-treatment with the selenocompounds. As a result the expected cell density would have been even greater at the time of peroxide insult, which has been shown to significantly reduce the cytotoxicity of hydrogen peroxide.[11]

The effect of the increased seeding density would have been at least partially offset by the longer treatment window. It has been shown that longer treatment durations, such as 24 hr, cause hydrogen peroxide to exhibit stronger cytotoxicity.[11] Literature suggests that the wide range of cytotoxicity displayed by hydrogen peroxide could also be due to the wide array of antioxidant defence systems that exist to protect against ROS damage.[89,90] As it is known that these defences differ between different tissues and cell lines, this means that it is expected that the IC_{50} value for SH-SY5Y cells would likely differ to the reported values for other cell lines.

Furthermore, in this study, hydrogen peroxide solutions were prepared by serial dilutions in complete media, other methods mentioned in the literature involved preparing higher concentration peroxide solutions in phosphate buffered saline (PBS)

and then pipetting these directly into the growth media at a marked dilution. This technique was unfavourable given the initial growth media contained the pre-treatment selenium compounds, which had to be removed and replaced with the peroxide containing growth media.

The simpler addition of peroxide-PBS solutions would have complicating extracellular drug-peroxide interactions, which would have interfered with the peroxide's role as an oxidative intracellular stress-inducing agent. However, the procedure employed allowed for the hydrogen peroxide to react with the growth media for several minutes prior cell exposure. Direct pipetting of peroxide in PBS would instead allow for a greater proportion of the peroxide to reach the cells before reacting with the growth media.

Taking the ramifications of these possible procedural variations into account, MTT trails of each treatment set were repeated 4-10 times with 16-24 replicates, before the data was collated for analysis. Additionally, a wide concentration range of 500-4000 µM was tested to ensure the full 100-0% viability curve was visualized for each trial. Finally the MTT assays were carried out with three different SH-SY5Y stocks (all still sourced from the American Tissue Culture Collection) at differing initial low passage numbers, to verify similar dose responses independent of the age of the cell line.

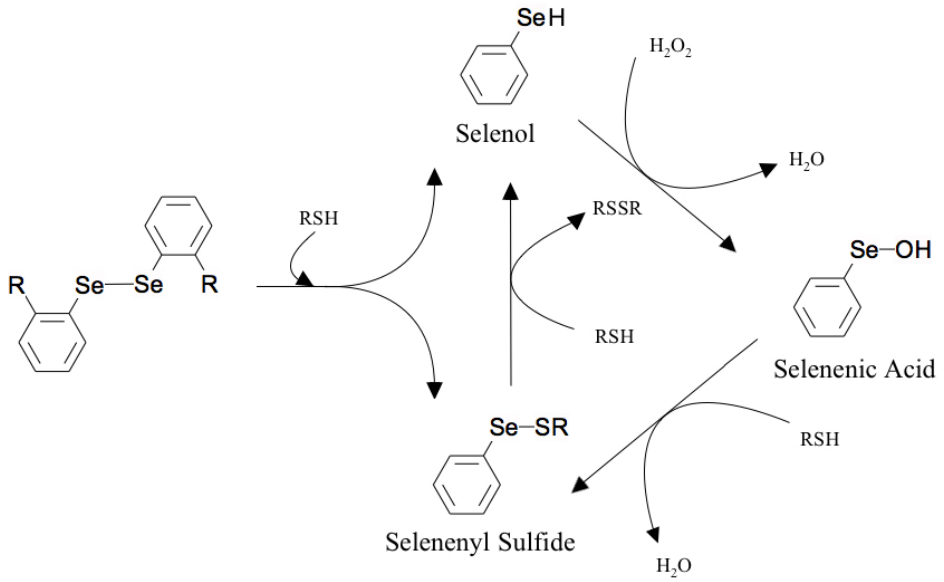

Scheme 3.5.1 – GPx-like catalytic cycle extrapolated for substituted diphenyl diselenide from literature on the antioxidant activity of benzylamine diselenides.[11,91]

It is known that Am-DPDS does not prevent oxidative damage to DNA induced by hydrogen peroxide in solution.[48] Instead, its protective action is reported to result from the selenol and selenenyl sulfide species formed from the cleavage of the diselenide bond (Scheme 3.5.1). The observed protective action thereby is either sourced from these metabolites or a secondary cellular response that could not be activated during the solution studies that only investigated direct drug-DNA interactions. To determine which of these was the source of the difference in protective action, synchrotron studies were carried out to investigate the intracellular selenium speciation and distribution.

3.5.2 Synchrotron Based Studies

3.5.2.1 Bis(2-nitrophenyl)diselenide XAS Studies

3.5.2.1.1 Bis(2-nitrophenyl)diselenide XANES Studies

XAS provides two distinct types of data that can be analysed separately, the XANES or edge region, and the EXAFS. XANES fitting has the experimental data fit with a linear combination of spectra obtained for possible known selenium species or model compounds. This provides a general indication of the selenium speciation within the sample.

EXAFS fitting allows for the identification of the selenium-bonding environment, i.e. the number and nature of neighbouring atoms, bond lengths and coordination number. The EXAFS fitting can use the XANES speciation as a starting point, with likely neighbours to the Se tested with reasonable bond lengths and coordination numbers to provide theoretical EXAFS spectra. These theoretical spectra are then compared to the experimental data and the structural parameters are optimized to provide the best fit to the experimental data.

SY-SY5Y cells were cultured as monolayers and then pre-treated with a lower 5 μM or higher 10 μM concentration of the selenium containing compounds for 24 hr prior to a 24 hr hydrogen peroxide insult to simulate oxidative stress conditions. After the 48 hr the cells were collected and centrifuged into bulk cell pellets that were freeze dried before XAS data collection.

Regardless of the oxidative stress level, all treatments with Ni-DPDS produced very similar XANES spectra (Figure 3.5.3, Left). All of the spectra shared the same white line peak at 12661 eV, as well as similar second peak energies of 12668-12669 eV. Despite the differences in spectral shapes, all spectra had a white line to second peak

ratio within the range 0.71-0.77, except for the 10 µM Ni-DPDS treated cell, which had a ratio of 0.68. Along with the sharp white line peak, these ratios indicate that self-absorption was not present within the spectra that can result in artefacts due to poor experimental optimization. Instead, the observed variations appear to be conserved across the pre-treatment conditions, with the 5 µM pre-treatments having a larger second peak energy than the 10 µM, and the variations indicate a change in the speciation dependent on intracellular selenium levels.

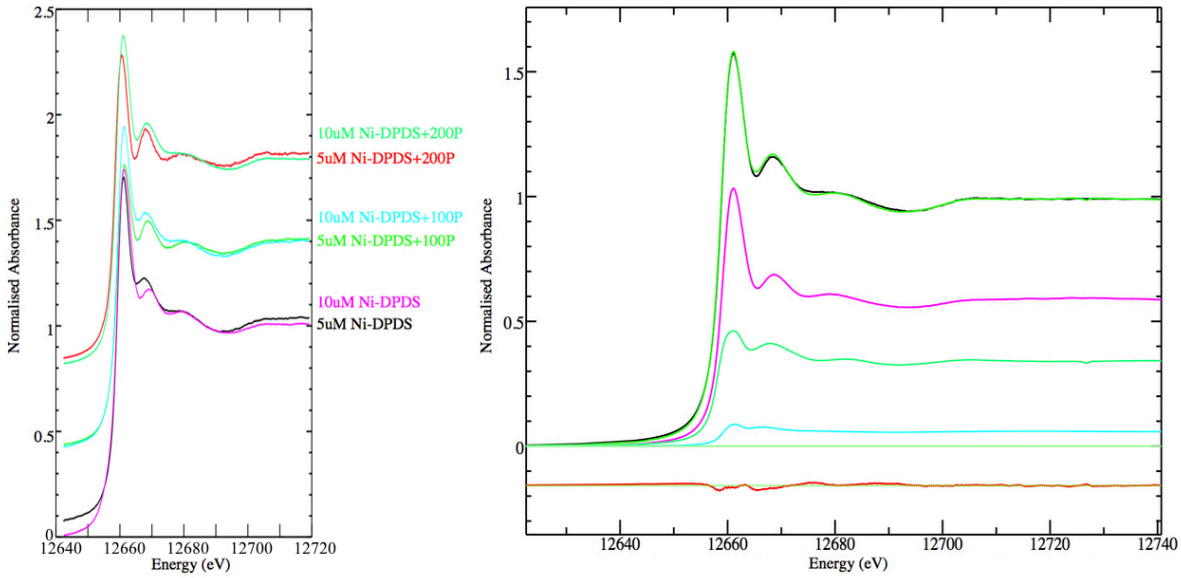

Figure 3.5.3 – Left: The selenium near-edge (XANES) region of bulk cell pellets treated with bis(2-nitrophenyl)diselenide for 24 hr prior to insult with hydrogen peroxide for 24 hours. All spectra shared the same white line peak energy and common second peak energy. Right: Fitted XANES spectra for SH-SY5Y bulk cell pellet treated with 10 µM bis(2-nitrophenyl)diselenide for 24 hours prior to insult with 200 µM hydrogen peroxide for 24 hours. The experimental spectrum is in black, while the resultant fit of the nitro diselenide (pink), amino diselenide (light green), and methylselenylcysteine (light blue) models is shown in dark green. The residual, or difference between the experimental and fitted data is shown in red.

XANES analysis of the spectra collected for the treated cells showed a consistent major component corresponding to the parent Ni-DPDS compound (Table 3.5.2). Coupled with this was a typically smaller fraction of methylselenocysteine (MSC), a Se-C bond containing species (Scheme 3.5.2). This could represent a proportion of the diselenide compound that has been reduced within the cells. This reduction would involve the cleavage of the central diselenide bond, leaving the selenium bound to the phenyl

carbon ring (Se-C) and hydrogen (Se-H). Thus the spectra of this cleaved Ni-DPDS would be similar to that of methylselenocysteine.

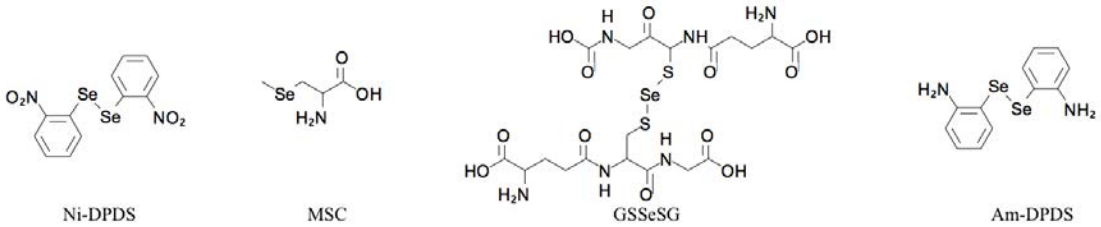

Scheme 3.5.2 – XANES fitted components for Ni-DPDS treated SH-SY5Y bulk cell samples, including the parent compound (Ni-DPDS), methylselenocysteine (MSC), seleno-diglutathione (GSSeSG) and Am-DPDS.

Table 3.5.2 – XANES linear combination fitting for cells treated with Ni-DPDS and subsequent hydrogen peroxide, showing percentage fraction of different species, as well as the residual for the fit and the resultant total for the fitted fractions.

Treatment	**Percentage of component fitted [a]**				**Residual (x 10^{-3})**	**Total [b]**
	Ni-DPDS	MSC	GSSeSG	Am-DPDS		
5 μ M Ni-DPDS	60(1)	38(1)			0.14	99
5 µM Ni-DPDS & 100 µM Peroxide	22(4)	72(4)			2.6	94
5 µM Ni-DPDS & 200 µM Peroxide	19(2)		23(2)	56(3)	0.85	97
10 µM Ni-DPDS	89(2)	14(2)			0.69	103
10 µM Ni-DPDS & 100 µM Peroxide	45.3(8)	55.9(8)			0.11	101
10 µM Ni-DPDS & 200 µM Peroxide	59(1)	6(1)		35(1)	0.044	100

[a] Values in the parentheses are the standard deviations estimated from the diagonal elements of the covariance matrix and note precision [b] Total denotes the sum of the fitted fractions.

The 200 µM peroxide treated cells showed additional fractions of the parent Am-DPDS compound (Figure 3.5.3, Right). This is not surprising as the Ni-DPDS and Am-DPDS model spectra are quite similar, with matching white line peaks at 12661 eV and very similar second peak energies of 12668.6 eV for Ni-DPDS and 12667.8 eV for Am-DPDS (Figure 3.5.4, top left) due to similar selenium environments conserved within the structures. The main difference is the two peak ratios of 0.67 for Ni-DPDS and 0.89 for Am-DPDS. This suggests that there may have been significant self-absorption within the Am-DPDS model spectra due to the sample being too concentrated.

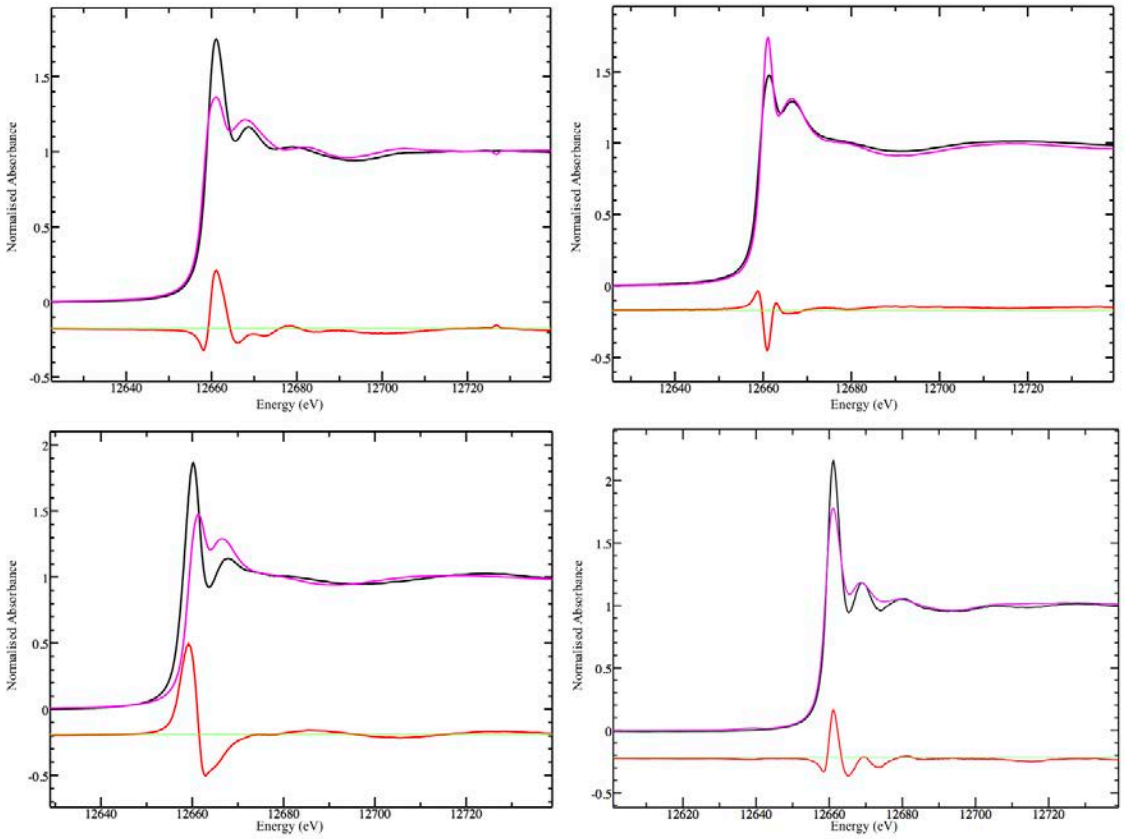

Figure 3.5.4 – Comparison plots of Ni-DPDS [black] against the amino analogue [purple] (top left) which had a residual of 0.57 x 10^{-2}; two Se-C models methyselenocysteine [purple] against ι-selenomethionine [black] (top right) which had a residual of 0.22 x 10^{-2}; a Se-S model seleno-diglutathione [black] against a Se-C model methyselenylcysteine [purple] (bottom left) which had a residual of 0.25 x 10^{-1}; solid Ni-DPDS spectra [purple] against the CPC water solubilized Ni-DPDS spectra [black] (bottom right), which had a residual of 0.46 x 10^{-2} .

Nevertheless, the difference is in stark contrast to a comparison of methylselenocysteine (MSC) with a Se-S bonding model seleno-diglutathione (GSSeSG). These two model spectra are very different with the residual between the spectra (red line, bottom left, Figure 3.5.4) clearly showing the difference in spectral morphologies and being an order of magnitude greater than for the two diselenides (Figure 3.5.4, top left).

GSSeSG has a white line peak at 12660 eV and a second peak at 12668 eV with a peak-to-peak ratio of 0.61, compared to MSC which has a white line peak at 12661.4 eV and a second peak at 12666.4 eV with a peak-to-peak ratio of 0.87.

However the difference is more pronounced than that expected between two structurally similar selenium species, such as compared to the differences between two Se-C species ι-selenomethionine (Se-Met) and MSC (Figure 3.5.4, top right). These two have a smaller residual and the same white line peak at 12661 eV, but Se-Met having subtly different second peak energy at 12666.6 eV and peak to peak ratio of 0.80.

Despite obtaining model spectra for both the Ni-DPDS as a solid and in aqueous solution (Figure 3.5.4, bottom right), only the solid-state spectrum was found to be a component of the XANES spectra. The spectra for the solvated parent compound, if forced to be part of the linear combination fit, resulted in poorer fits with larger residuals.

For example the bulk cell samples pre-treated with 10 μM Ni-DPDS for 24 hours with a subsequent 200 μM hydrogen peroxide insult when fitted with the aqueous standards gave a greater fit component to the Am-DPDS over the Ni-DPDS, and a greater residual of 0.51×10^{-3} compared to the solid standards fit residual of 0.44×10^{-3} (Figure 3.5.5). Furthermore the total fit percentage was reduced from 100 per cent for the solid standards to 96 per cent.

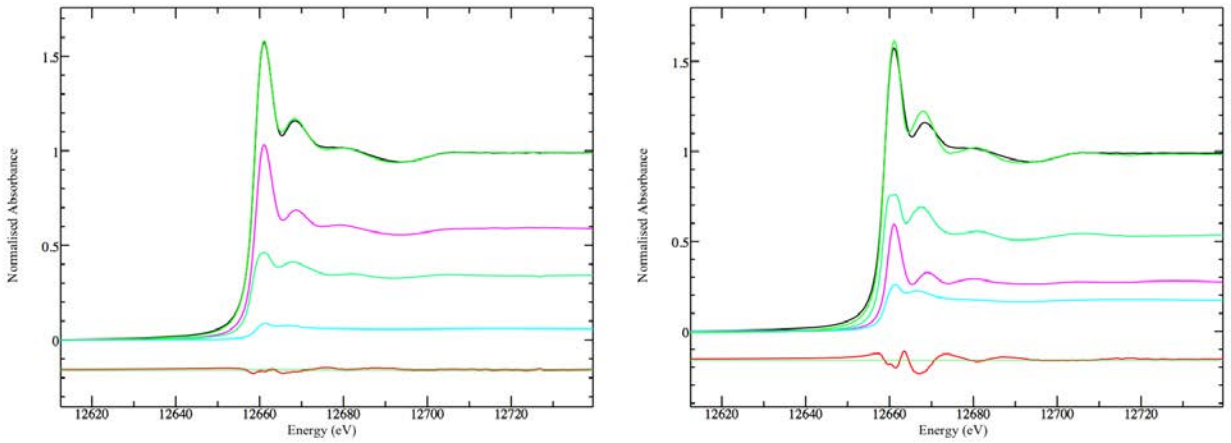

Figure 3.5.5 – XANES fittings for SH-SY5Y bulk cell samples pre-treated with 10 µM Ni-DPDS for 24 hours with a subsequent 200 µM hydrogen peroxide insult. Spectra fit with model spectra for solid Ni-DPDS (purple) [left] or CPC water-solubilized Ni-DPDS (purple) [right], Am-DPDS (light green) and MSC (light blue) components. The experimental spectrum is black, while the resultant fit of the three components is shown in dark green. The residual, or difference between the experimental and fitted data is shown in red.

The worst fit, which had an order of magnitude greater residual and only a 94% fraction fit total, was that of the 5 µM Ni-DPDS with a 100 µM hydrogen peroxide insult treated cells. The lower 5 µM treatments, where 100% uptake is not guaranteed, tended to result in spectra that had noise that resulted in sub-optimal fitting. However the components expected were conserved, if in differing percentages.

3.5.2.1.2 Bis(2-nitrophenyl)diselenide EXAFS Studies

EXAFS fitting for the Ni-DPDS pre-treated bulk cell pellets yielded results consistent with the XANES fitting, showing two dominant backscatters or neighbours to the selenium atoms, being C at 1.87-1.89 Å and Se at 2.34-2.36 Å (Figure 3.5.6). These values are in accordance with literature on aromatic diselenides, with DPDS having Se-C bond length of 1.93 Å and Se-Se bond length of 2.29 Å.[92] Bis(p-nitrophenyl)diselenide has been observed to have Se-C bond lengths of 1.92 Å and Se-Se bond lengths of 2.30 Å.[93]

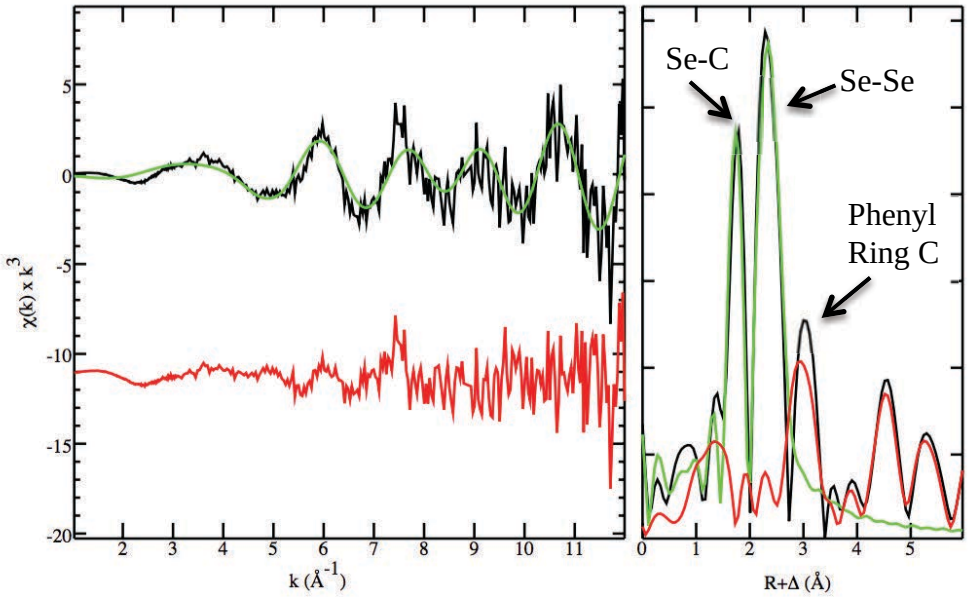

Figure 3.5.6 – EXAFS spectra (left) and corresponding Fourier transforms (right) for a 10 µM Ni-DPDS, 100 µM hydrogen peroxide treated SH-SY5Y bulk cell pellet, with the experimental data in black, the fit in green and the residual in red. Fit parameters are reported in Table 3.3.3.

In addition a backscatter at ~3.3 Å was noticeable, which was assumed to correspond to the phenyl ring carbon adjacent to the diselenide bridge.[92] These peaks could not be well fit as the noise levels in the EXAFS were too high to accommodate acceptable multiple scattering fits.

There are, nonetheless, two possible Se-C bond lengths around 3 Å to consider (Scheme 3.5.3). First there is 3.2 Å between the Se and the second phenyl ring adjacent to the C bound to the Se atom in the parent molecule (assumed to be similar to DPDS), while it is 3.4 Å from the Se to the C bound to the other Se atom. Thus if both are present and similar in the more water soluble diselenides, Ni-DPDS and Am-DPDS, then the resultant composite peak would be broad and centred ~3.2 Å (as observed).

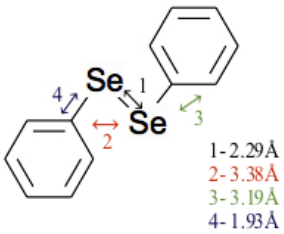

Scheme 3.5.3 – Structure of DPDS with the four interatomic bond lengths indicated as per the crystal structure.

There was also a peak observed in the EXAFS between 4 and 5 Å that was unfitted, this could correspond to the bond lengths between the Se atom and the meta (~4.2 Å) and para (~4.6 Å) carbons which would combine to make a composite peak at ~4.4 Å. These peaks, similar to the aforementioned phenyl ring carbons, were unable to be modelled, as the noise level was too great to allow for sufficient quality multiple scattering fits (Figure 3.5.7).

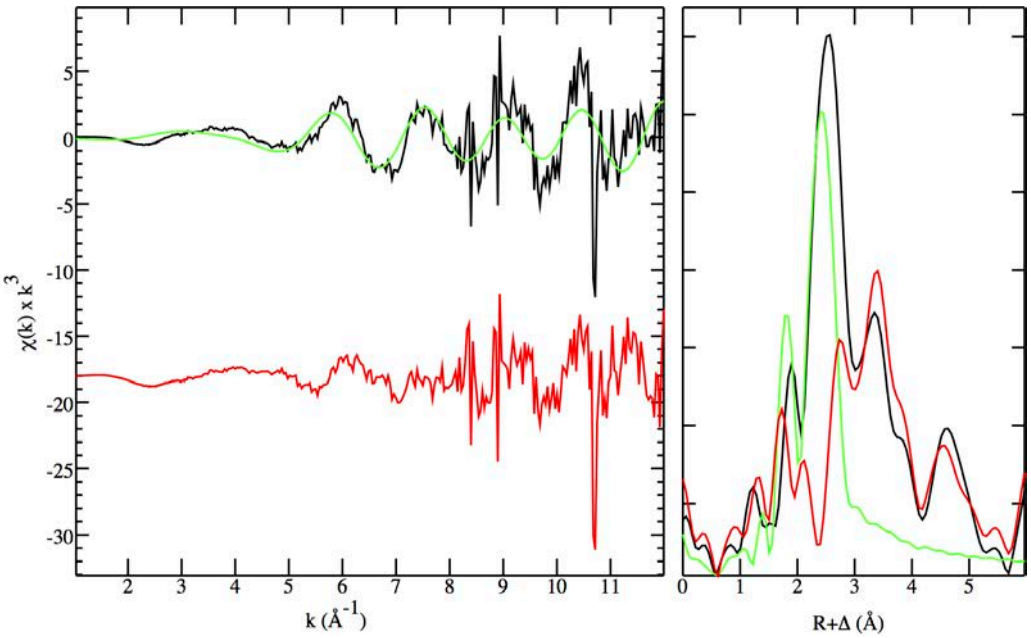

Figure 3.5.7 - EXAFS spectra (left) and corresponding Fourier transforms (right) of SH-SY5Y cells treated for 24 h with 5 µM Ni-DPDS for 24 hr showing experimental (black) and calculated (green) data with the residual shown offset (red). Fit parameters are reported in Table 3.5.3.

Table 3.5.3 – Parameters fit to EXAFS spectra of SH-SY5Y cells treated with Ni-DPDS and then insulted with hydrogen peroxide. [a]

Treatment	Scatterer	Coordination Number, N	Interatomic distance, R (Å)	Debye-Waller Factor, σ^2 (Å^2)	$-\Delta E_o$ (eV) [b]	Fit Error
5 µM Ni-DPDS	C	1.2(4)	1.92(1)	0.001(2)	10(3)	0.89
	Se	0.8	2.37(1)	0.0058(7)	10(3)	
10 µM Ni-DPDS	C	1.1(1)	1.890(7)	0.001(1)	9(2)	0.69
	Se	0.9	2.369(6)	0.0040(3)	9(2)	
10 µM Ni-DPDS & **100 µM Peroxide**	C	1.2(2)	1.86(2)	0.004(2)	12(2)	0.94
	Se	0.8	2.33(1)	0.006(1)	12(2)	
10 µM Ni-DPDS & **200 µM Peroxide**	C	1.1(5)	1.90(2)	0.004(3)	12(3)	0.85
	Se	0.9	2.348(9)	0.0038(4)	12(3)	

[a]The k-range was 1 – 12 Å^{-1} and a scale factor (S_0^2) of 0.9 was used for all fits. $\Delta E_0 = E_0 - 12658$ (eV) where E_0 is the threshold energy. Values in parentheses are the estimated standard deviation derived from the diagonal elements of the covariance matrix and are a measure of precision. The fit-error is defined as $[\Sigma k^6(X_{exp} - X_{calc})^2/\Sigma k^6 X_{exp}^2]^{1/2}$.

The coordination numbers for the fitting of C and Se backscatterers show non-integer values; this may indicate that some fraction of the parent compound was reduced. This reduction thus decreases the average coordination of selenium from one while the average Se-C coordination would be increased. This is consistent with the XANES results that showed a dominant fraction of the parent Ni-DPDS component but with additional Se-C components (MSC), which could represent this reduced form. Unlike the XANES results that showed variable reduction and thus MSC component fitted throughout the 10 µM samples, the EXAFS indicate a relatively stable level of reduction by consistent C coordination numbers across the different treatment conditions.

The XANES fitting for the SH-SY5Y cells treated for 24 hr with 10 µM Ni-DPDS followed by 100 µM hydrogen peroxide insult for a further 24 hours showed a marked

decrease in the parent Ni-DPDS component fit with no compensating Am-DPDS component fit. Thus it was expected that the EXAFS for this sample would show a likewise diminished Se-Se bond signal. This was observed (Figure 3.5.8) with the Se-C:Se-Se signals in the Fourier transform being 8.6:10 in intensity for this sample (**I**) when compared with 7.3:10 for the EXAFS for the 10 µM Ni-DPDS followed by 200 µM hydrogen peroxide cell sample's Fourier transform (**III**). The Fourier transforms for cells treated with 10 µM Ni-DPDS alone (**II**) were consistent with those treated with 10 µM Ni-DPDS followed by 200 µM hydrogen peroxide (**III**).

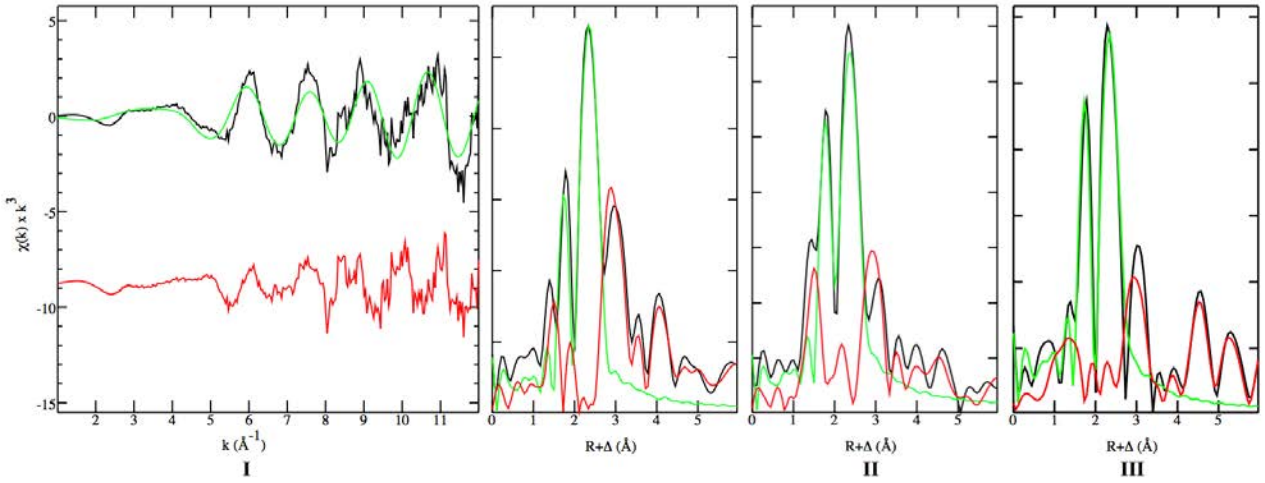

Figure 3.5.8 – (**I**) EXAFS spectra and corresponding Fourier transforms of SH-SY5Y cells pre-treated for 24 hr with 10 µM Ni-DPDS followed by 200 µM hydrogen peroxide insult for a further 24 hr showing experimental (black) and calculated (green) data with the residual shown offset (red). (**II**) Fourier transforms of SH-SY5Y cells treated for 24 hr with 10 µM Ni-DPDS showing experimental (black) and calculated (green) data with the residual shown offset (red). (**III**) Fourier transforms of SH-SY5Y cells treated for 24 hr with 10 µM Ni-DPDS followed by 100 µM hydrogen peroxide insult for a further 24 hr showing experimental (black) and calculated (green) data with the residual shown offset (red). Fit parameters are reported in Table 3.5.3.

3.5.2.2 Bis(2-aminophenyl)diselenide XAS studies

3.5.2.2.1 Bis(2-aminophenyl)diselenide XANES Studies

In a similar fashion to the Ni-DPDS experiments, SY-SY5Y cells were cultured as monolayers and then pre-treated with a lower 5 µM or higher 10 µM concentration of Am-DPDS for 24 hours prior to a 24 hour hydrogen peroxide insult to simulate oxidative stress conditions. After 48 hours, the cells were collected and centrifuged into bulk cell pellets that were freeze dried before XAS data collection. The XANES fitting results for the Am-DPDS treated cells were markedly different to the results for the Ni-DPDS (Figure 3.5.9).

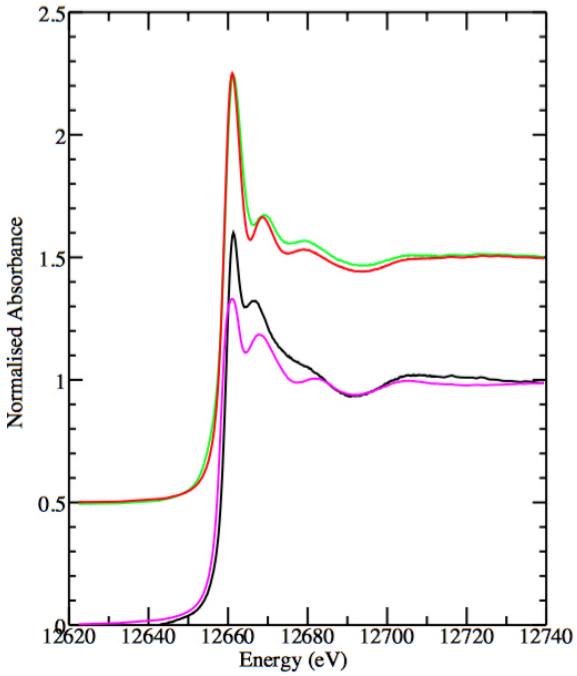

Figure 3.5.9 – The selenium near-edge (XANES) region of bulk SH-SY5Y cell pellets treated with Am-DPDS for 24 hr (black) and the parent Am-DPDS compound (purple) showing large differences compared to the spectra of Ni-DPDS treated for 24 hr cells (green) compared to its parent Ni-DPDS compound (red).

Fitting of the resultant spectra instead showed no fraction of the parent Am-DPDS compound present, instead having a major component of methylselenocysteine (MSC) (Table 3.5.4), indicating that all the compound had been reduced, or the diselenide bond cleaved, within the cell.

Table 3.5.4 – XANES fitting for cells treated with Am-DPDS prior to hydrogen peroxide insult, showing percentage fraction of different species, as well as the residual for the fit and the resultant total for the fitted fractions.

Treatment	Percentage Fitted Component [a]			Residual ($\times 10^{-3}$)	Total [b]
	MSC	SeMet	Ni-DPDS		
5 µM Am-DPDS	91(3)	10(3)		0.48	101
5 µM Am-DPDS & 100 µM Peroxide	90(3)	9(3)		0.53	99
5 µM Am-DPDS & 200 µM Peroxide	45(6)	47(6)		1.9	91
10 µM Am-DPDS	69(3)	34(3)		0.61	103
10 µM Am-DPDS & 100 µM Peroxide	76(3)	25(3)		0.54	102
10 µM Am-DPDS & 200 µM Peroxide	75(2)	9(2)	17(1)	0.21	101

[a] Values in the parentheses are the standard deviations estimated from the diagonal elements of the covariance matrix and note precision [b] Total denotes the sum of the fitted fractions.

Only the higher treatment concentration sample, 10 µM diselenide with a 200 µM peroxide insult, showed any fit component of the parent compound. Apart from methylselenocysteine (MSC), samples were also shown to have a lesser component matched to ι-selenomethionine, another Se-C model compound. Methylselenocysteine and ι-selenomethionine are both Se-C bonded species, and as such produce very similar XANES spectra (Figure 3.5.4, top right). Both of these models have the same white line peak energy and the same second peak energy as mentioned previously.

The lower concentration samples gave generally poorer fits, in particular the 5 µM diselenide with a 100 µM peroxide insult (Figure 3.5.10, black), had the largest uncertainties in the fractional percentages, and a sum that did not represent the total of 100%. The noise in the spectrum for this sample had a greater effect on the fitting of

this sample than of the higher concentration samples such as the 10 µM Am-DPDS spectra shown (Figure 3.5.10, red). The signal to noise ratio† for the lower concentration was an order of magnitude higher than that present in the 10 µM Am-DPDS spectrum, at 1.6 x 10^{-3} and 2.7 x 10^{-4} respectively.

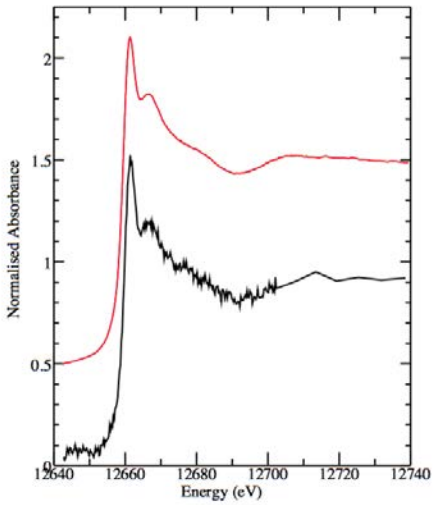

Figure 3.5.10 – XANES spectra for (black) SH-SY5Y bulk cell pellets treated with 5 µM Am-DPDS and then insulted with 200 µM hydrogen peroxide and (red) SH-SY5Y bulk cell pellets treated with 10 µM Am-DPDS.

Lastly, the 10 µM Am-DPDS and 200 µM hydrogen peroxide treated cell pellets spectrum was fit with a minor fraction of the Am-DPDS parent compound. As discussed above this is not significantly different to that of the amine compound, and so may represent some small fraction of non-reduced parent compound.

3.5.2.2.2 Bis(2-aminophenyl)diselenide EXAFS Studies

The EXAFS of cells treated with Am-DPDS, in stark contrast to the EXAFS of the cells treated with Ni-DPDS, featured only one main Se-C peak, with a small phenyl ring carbon peak (Figure 3.5.11). Furthermore, the phenyl ring C peak was now sharp and centred around 3 Å. This is logical as it corresponds to scatter between the Se and the carbon on the adjacent phenyl ring alone due to diselenide cleavage, i.e. due to the cleavage, the distance marked "2" is no longer possible and only "3" remains (Scheme 3.3.4). In other words, this indicated that the longer 3.4 Å bond length from Se to the C

† Signal to noise ratio was calculated as defined by Shimadzu's support instructions[94] as S(peak height)/N(noise in RMS). "Noise in RMS" was calculated for spectral range 12460-12640 eV as the average absolute deviation from the mean signal intensity. The white line peak was used to define the "peak height" value.

bound to the other Se was no longer present, further suggesting cleavage of the compound.

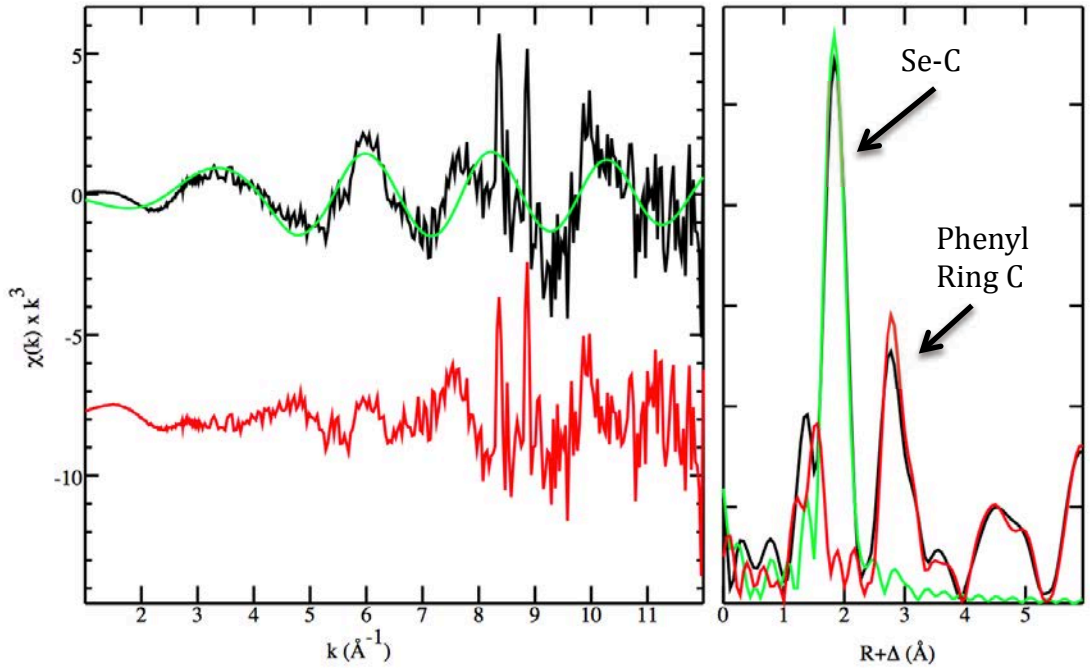

Figure 3.5.11 - EXAFS spectra (left) and corresponding Fourier transforms (right) of SH-SY5Y cells treated for 24 h with 5 µM Am-DPDS for 24 hours showing experimental (black) and calculated (green) data with the residual shown offset (red). Fit parameters are reported in Table 3.5.5.

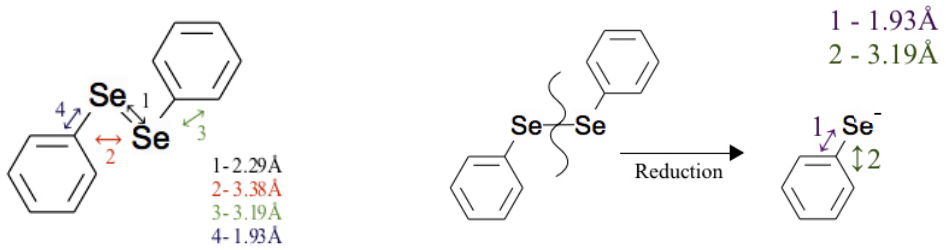

Scheme 3.3.4 – Left: Structure of DPDS with the four interatomic bond lengths indicated as per the crystal structure. Right: Schematic of the reduction of diselenide bridge, DPDS used as the example, with the resultant selenium interatomic bond lengths indicated with their corresponding values.

Once again the EXAFS interpretations reiterate the XANES results that there is no longer any of the parent Am-DPDS compound inside the cells after a 24-hr incubation (Table 3.5.5).

Table 3.5.5 – Parameters fit to EXAFS spectra of SH-SY5Y cells treated with Am-DPDS and then insulted with hydrogen peroxide.[a]

Treatment	Scatterer	Coordination Number, N	Interatomic distance, R (Å)	Debye-Waller Factor, σ^2 ($Å^2$)	$-\Delta E_o$ (eV) [b]	Fit Error
5 µM Am-DPDS	C	1.8(1)	1.906(7)	0.0032(5)	10(2)	0.82
5 µM Am-DPDS & **100 µM Peroxide**	C	2.5(4)	1.89(2)	0.0010(7)	12(5)	0.95
10 µM Am-DPDS	C	2.0(1)	1.899(5)	0.0033(4)	10(1)	0.73
10 µM Am-DPDS & **100 µM Peroxide**	C	1.9(1)	1.905(6)	0.0043(5)	8(1)	0.77
10 µM Am-DPDS & **200 µM Peroxide**	C	1.9(1)	1.892(3)	0.0012(4)	11(3)	0.79
10 µM Am-DPDS & **200 µM Peroxide**	C	1.5(1)	1.887(6)	0.0001	13(2)	0.75
	Se	0.5(1)	2.40(2)	0.009(2)	13(2)	

[a]The *k*-range was 1 – 12 $Å^{-1}$ and a scale factor (S_0^2) of 0.9 was used for all fits. ΔE_0 = E_0 – 12658 (eV) where E_0 is the threshold energy. Values in parentheses are the estimated standard deviation derived from the diagonal elements of the covariance matrix and are a measure of precision. The fit-error is defined as $[\Sigma k^6(X_{exp} - X_{calc})^2/\Sigma k^6 X_{exp}^2]^{1/2}$.

This points to a possible required activation step where the diselenide must be cleaved to produce a positive protective intracellular effect. The increased ease of the reduction between the two DPDS analogues may be due to the differences in the electronic structure of the phenyl ring between the two compounds. In the Am-DPDS, the amine groups delocalise a negative charge throughout the ring and Se due to the lone pair from the amines. The Ni-DPDS, on the other hand, is an electron-withdrawing group that does not display the same kind of resonance stabilization effects. As a consequence the

cleaved Am-DPDS structure would be more stabilized due to the amine functional group, unlike in the Ni-DPDS structure.

For the sample which had a XANES component of the Ni-DPDS, cells treated with 10 µM Am-DPDS for 24 hours prior to insult with 200 µM hydrogen peroxide (Figure 3.5.12), the EXAFS largely contradicted the XANES results Instead only one main Se-C peak was present along with the phenyl ring C peak. However the phenyl ring carbon peak may be masking a small diselenide peak due to the similar interatomic distances. During the fitting process the shoulder peak at 2.3 Å could be attributed to a Se-Se bond (Figure 3.5.12, right), strengthening the assertion that a small Se-Se peak could be present. However the noise in the EXAFS prevented the determination of whether this was evidence of a diselenide bond or just an artefact of the noise.

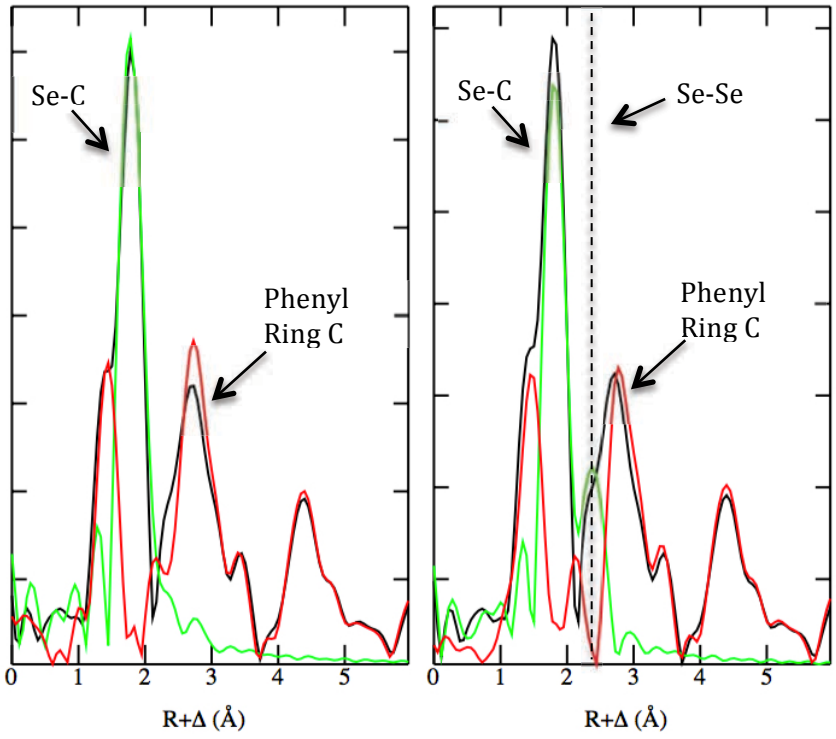

Figure 3.5.12 – Fourier transforms for a SH-SY5Y bulk cell pellet treated with 10 µM Am-DPDS for 24 hours prior to insult with 200 µM hydrogen peroxide. Experimental data is represented in black while the resultant fit in green. Left: EXAFS fit with realistic structural parameters but no Se-Se bond, Right: EXAFS forced to be fit for Se-Se bond, but which resulted in unrealistic parameters.

When the Se-Se bond was forced into the fitting process the resultant bond length was at 2.4 Å, which was not considerably higher than that of 2.36 Å as determined from the crystal structure for Am-DPDS[95]. The Se-C bond length was comparable to those fit for

the Ni-DPDS samples' EXAFS and DPDS literature bond length of 1.90 Å[95] however the Debye-Waller factor during the fitting for Se-C needed to be fixed at 0.0001 Å^2 to prevent it being optimized to a negative value. Conversely, the Debye-Waller factor for Se-Se is very large for the fit at 0.009 Å^2. Taken together, these observations suggest that while there may be a Se-Se bond present in some fraction of the total selenium species present in the treated cells, it is at too low a level to be identified above the noise. This is exacerbated by the possible Se-Se interaction being partially masked by the adjacent Se-C phenyl ring peak.

The evidence of cleavage or reduction of the Am-DPDS inside cells, given that the cytotoxicity-based evidence for Ni-DPD showed no protective action, indicates that the intracellular reduction may be important for the protective action against oxidative stress induced damage. This is not unprecedented, as it has been previously shown that Am-DPDS and DPDS undergo redox reactions in vitro and vivo studies, and this has been linked to their GPx-like activity.[35,96,97] Briefly, if Ni-DPDS is resistant to diselenide cleavage, then the GPx-like activity which requires the reversible interaction of the selenium with thiols would be impossible. In contrast Am-DPDS being able to be readily reduced would allow for the ability to readily undergo redox reactions with peroxide and thiols to give GPx-like activity (Scheme 3.5.1).

3.5.2.3 Ebselen XAS Studies

3.5.2.3.1 Ebselen XANES Studies

Experiments using SY-SY5Y cells cultured as monolayers and then pre-treated with a lower 5 μM or higher 10 μM concentration of Ebselen for 24 hours prior to a 24 hour hydrogen peroxide insult to simulate oxidative stress conditions were conducted so that the previous results could be compared to an accepted neuroprotective agent. After the 48 hours the cells were collected and centrifuged into bulk cell pellets, which were then freeze dried before XAS data collection.

XANES fitting of the resultant spectra showed a consistent major component, ~60%, corresponding to the Ni-DPDS compound (Table 3.5.6). Given the structural similarities between an Ebselen dimer and the nitro compound (Scheme 3.5.5) it is expected that fitting with this model's spectrum shows support for the intracellular presence of the Ebselen dimer. Coupled with this was a typically smaller fraction, 20-26%, of Se-S containing species (seleno-diglutathione GSSeSG and sulfoselenylcysteine

CysSSeCys). This could represent a proportion of the compound that is bound to intracellular protein thiol groups, such as cysteine residues, or reduced glutathione.[98] Finally, a 10-20% component was attributed to Se-C containing species, either SeMet or MSC.

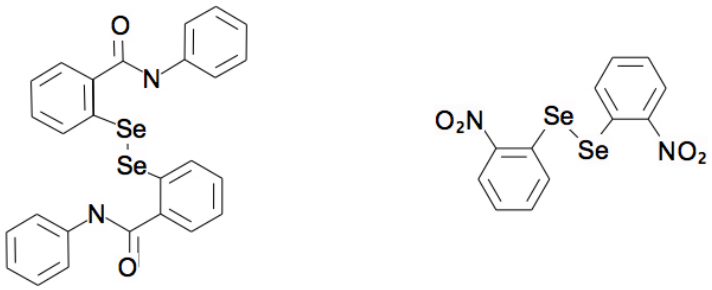

Scheme 3.5.5 – Chemical structures of the ring-opened Ebselen dimer (left) which shows structural similarities to Ni-DPDS (right).

Table 3.5.6 – XANES fitting for Ebselen treated cells, showing percentage fraction of different model species, the residual for the fit, and the resultant total for the fitted fractions.

Treatment	Percentage Fitted Component [a]					Residual (x 10^{-3})	Total [b]
	Ni-DPDS	GSSeSG	SeMet	MSC	Cys-S-Se-Cys		
5 µM Eb	60(2)	26(1)	13(1)			0.33	97
5 µM Eb & 100 µM Peroxide	40(4)		11(2)		19(3)	0.98	70
5 µM Eb & 200 µM Peroxide	58(2)	24(1)	16(1)			0.33	98
10 µM Eb	58(2)	23(1)	8(2)	12(2)		0.28	101
10 µM Eb & 200 µM Peroxide	60(1)	18(6)	17(2)	6(2)		0.13	101

[a] Values in the parentheses are the standard deviations estimated from the diagonal elements of the covariance matrix and denote precision [b] Total denotes the sum of the fitted fractions.

Again one of the lower treatment concentration samples gave a poor quality fit (Figure 3.5.13), which had a relatively small residual, but a total of only 70% fractions fitted. This low total is likely due to the noise in the pre and post edge region, which arises from the low intracellular selenium concentrations and resultant weak signal. It was also fit with selenylcysteine instead of seleno-diglutathione, as both are Se-S species this still suggests some small amount of thiol bound Ebselen.

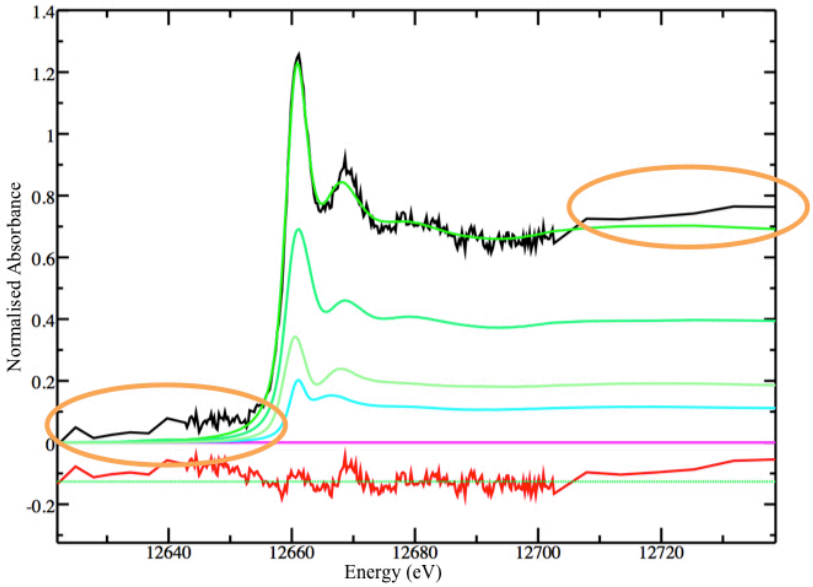

Figure 3.5.13 - Fitted XANES spectra for SH-SY5Y bulk cell pellet treated with 5 µM Ebselen for 24 hours prior to insult with 100 µM hydrogen peroxide for 24 hours. The experimental spectrum is in black, while the resultant fit of the Ni-DPDS (dark green), selenomethione (light green), and selenylcysteine (light blue) is shown in green. The residual, or difference between the experimental and fitted data is shown in red.

Thiol-bound Ebselen, a common component of the fitting, is part of its proposed mechanism of action[23,26-32], but given the toxicology results showing no protective action, this thiol-bound Ebselen may in fact be trapped and so unable to carry out its catalytic action of protection.

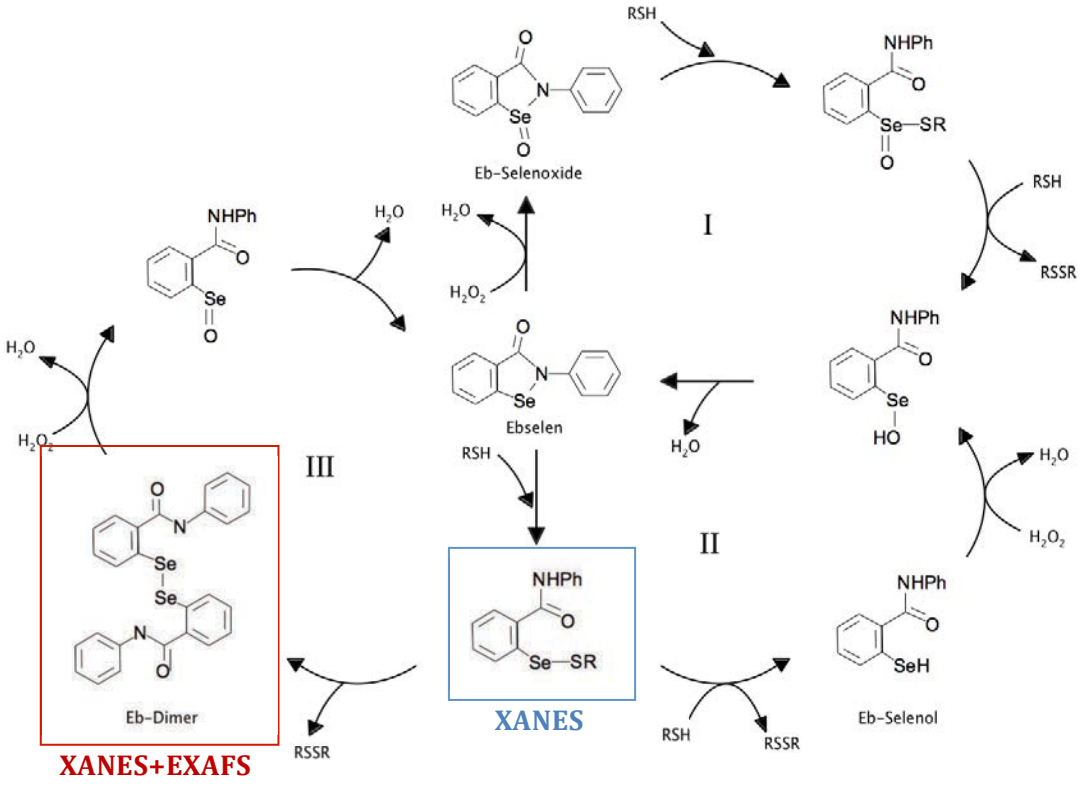

Figure 3.5.14 –Summary of different proposed modes of action for Ebselen's glutathione peroxidase activity reacting with both hydrogen peroxide and organic thiols such as glutathione (RSH). Species found to be present within Ebselen treated cells' observed X-ray absorption spectra are denoted, suggesting the involvement of Mechanism III.

Given that the fitting of Ebselen treated cells showed the presence of a Ni-DPDS-like compound as well as thiol bound selenium species, the XANES data indicate the involvement of cycle III (Figure 3.5.14).

3.5.2.3.2 Ebselen EXAFS Studies

The Ebselen EXAFS (Figure 3.5.15) were reminiscent of the bis-(2-nitrophenyl)diselenide treated cell EXAFS with two backscatterers observed at different distances. Similar to the EXAFS of Ni-DPDS treated cells, these corresponded to Se-C and Se-Se bonds. The bond lengths for both the C and Se backscatterers agree with literature with Se-C (aromatic) bond lengths 1.896-1.920 Å[93,95,99], and Se-Se bond lengths being 2.30-2.36 Å[93,95,99].

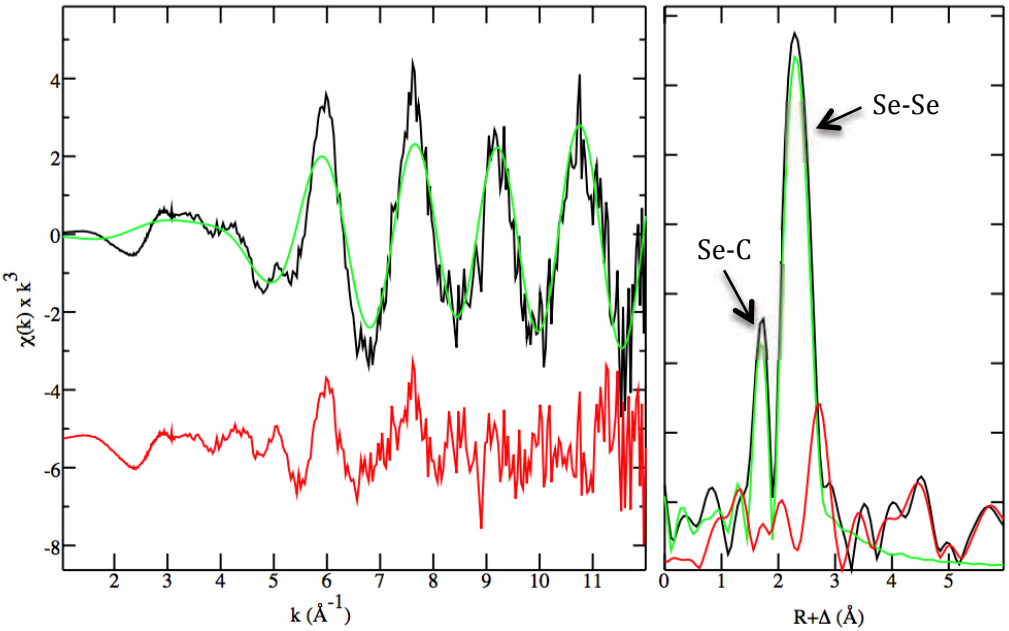

Figure 3.5.15 - EXAFS spectra (left) and corresponding Fourier transforms (right) of SH-SY5Y cells treated for 24 h with 10 µM Ebselen for 24 hours prior to 24 hour insult with 200 µM hydrogen peroxide showing experimental (black) and calculated (green) data with the residual shown offset (red). Fit parameters are reported in Table 3.5.7.

Notably, there was an absence of any evidence of any S backscatterer as indicated from the XANES fitting. There is no shoulder on the Se-Se peak within the Fourier transform at 2.193-2.195 Å, the Se-S bond length range[99], which does not appear to be in accordance with any of the proposed mechanisms of action. However, if the interaction between Ebselen and thiols like GSH are catalytic, it may be that the association is too transient to be detected by EXAFS. Ultimately, the results of the XANES and EXAFS fail to consistently indicate the presence of Se-S within the cellular samples, but don't disprove its possible presence.

While the lower treatment concentration samples yielded EXAFS too noisy to fit, all EXAFS able to be fitted yielded consistent results, with Se-C and Se-Se backscatterers. The EXAFS and XANES results therefore provide combined evidence for the presence of a mechanism of action for Ebselen's GPx activity involving GSH induced dimerisation (Cycle III, Figure 3.5.14).

Table 3.5.7 – Parameters fit to EXAFS spectra of SH-SY5Y cells treated with Ebselen and then insulted with hydrogen peroxide. [a]

Treatment	Scatterer	Coordination Number, N	Interatomic distance, R (Å)	Debye-Waller Factor, σ^2 (Å^2)	$-\Delta E_o$ (eV) [b]	Fit Error
5 µM Ebselen	C	1.0(2)	1.90(1)	0.001	15(2)	0.72
	Se	1.0(2)	2.326(7)	0.0025(3)	15(2)	
10 µM Ebselen	C	1.00(7)	1.892(4)	0.0009(5)	17(1)	0.38
	Se	1.00(7)	2.309(3)	0.0028(1)	17(1)	
10 µM Ebselen & 200 µM Peroxide	C	1.0(2)	1.892(8)	0.003(2)	16(2)	0.51
	Se	1.0(2)	2.316(6)	0.0041(2)	16(2)	

[a]The k-range was 1 – 12 Å^{-1} and a scale factor (S_0^2) of 0.9 was used for all fits. $\Delta E_0 = E_0 - 12658$ (eV) where E_0 is the threshold energy. Values in parentheses are the estimated standard deviation derived from the diagonal elements of the covariance matrix and are a measure of precision. The fit-error is defined as $[\Sigma k^6(X_{exp} - X_{calc})^2/\Sigma k^6 X_{exp}^2]^{1/2}$.

Fitting of the cells treated with 5 µM Ebselen required the fixation of the carbon backscatterer's Debye-Waller Factor at a small positive value. While the Fourier transforms showed clear indications of a carbon backscatterer at 1.90 Å the general noise in the EXAFS for the sample was too high to optimize structural parameters for this interaction to reasonable values. The values within the table were included as the calculated model was a close visual match to the experimental spectra (Figure 3.5.16). The noise in the Fourier transforms is most apparent for this sample when compared to the higher concentration treatments resulting EXAFS (Figure 3.5.15).

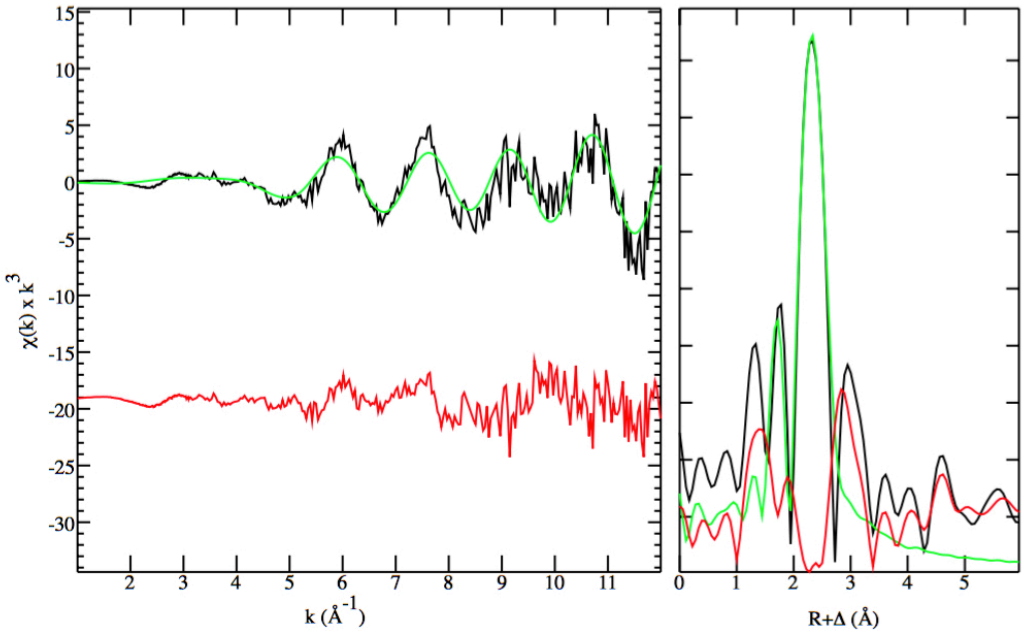

Figure 3.5.16 - EXAFS spectra (left) and corresponding Fourier transforms (right) of SH-SY5Y cell treated with 5 μM Ebselen for 24 hours showing the experimental (black) and calculated (green) data with the resultant residual shown offset (red). Fit parameters are reported in Table 3.5.7.

However, the evidence for the dimer doesn't necessarily support cycle III being the mode of action, especially given that no discernable protective effect was observed for Ebselen in the toxicology studies. Instead it may be that a competing mechanism prevents Ebselen from protecting against oxidative stress induced damage. This may explain why Ebselen showed no protective action in the cytotoxicity studies, while it has been shown to have protective action in other studies. Thus, at the conclusion of the speciation studies there is evidence that cycle III can take place within SH-SY5Y cells, but without protective action against oxidative stress. Cycle II may therefore be the protective pathway as proposed[23,32], but seemed to not to be occurring within the cells under the conditions employed here.

3.5.2.4 X-Ray Fluorescence Microscopy Studies

Cellular uptake and distribution of selenium-containing compounds was investigated using X-Ray fluorescence microscopy in an effort to seek a rationale as to why one of the diselenides shows protective action, whereas the other failed to do so. SH-SY5Y cells were grown on silicon nitride windows overnight before being treated with 5 μM Am-DPDS or Ni-DPDS or 10 μM Ebselen for 24 hours. After incubation with the

treatment compounds the cells were fixed with paraformaldehyde and freeze dried before XFM imaging.

When SH-SY5Y cells were fixed with paraformaldehyde their morphology was preserved for XFM imaging.[53,55,61,100] The zinc (Zn) map was used to identify the boundaries of the cells as this element showed consistently higher signal-to-noise ratio than the other endogenous elements (Figure 3.5.17). The synchrotron beam at an energy of 12.7 keV was focused to 1 µm and then raster scanned to simultaneously obtain maps of elemental distribution within individual cells. As the beam moved across the cells, the resulting fluorescence spectrum at each dwell point was collected and formed a single pixel within the elemental maps.

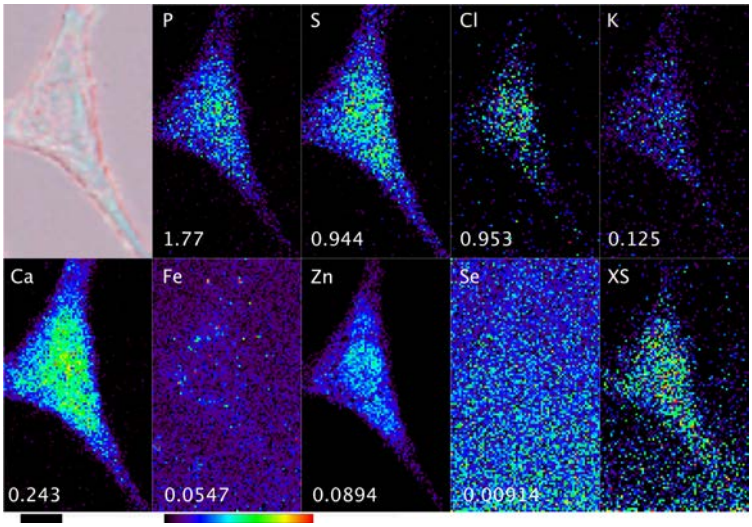

Figure 3.5.17 – Optical micrographs (top left), scattered X-ray (XS) and XFM elemental distribution maps of a SH-SY5Y control cell. The maximal elemental area density (quantified from standards and expressed in micrograms per square centimetre) is given in the bottom corner of each map. The black bar under the maps represents 10 µm.

These maps, due to the time required to complete scans, did not always contain the cells in their entirety, instead preference was given for the main body over protruding outgrowths. This was because the protruding outgrowths typically required large amounts of background to be imaged, without much gain in the actual cell area.

Information rich elemental maps were obtained for typically important biological elements (P, S, Cl, K, Ca) as well as transition metals (Fe, Zn). Selenium was found to be below the detection limit (0.1 $\mu g.g^{-1}$)[56] within the control cells (Figure 3.5.17), shown by an extremely weak fluorescence signal without any definable cellular localization.

All cells showed elemental concentrations localized within the cell, with the exception of iron (Fe) whose lower concentrations meant that any dust spots on the windows gave false positives outside the cell. Nuclear regions of the cells were identified using the P and Zn images, given the inherently higher concentrations of phosphate from the DNA backbone and Zn from zinc finger proteins within the nucleus.[101]

The inactive Ni-DPDS was observed to be excluded from the nuclear region (Figure 3.5.18, top), which, given that hydrogen peroxide is known to induce apoptosis which involves mechanisms within the nucleus [81,102], may account for Ni-DPDS's lack of protective action. Intrinsic, or stress-damage-induced, apoptosis occurs when DNA damage is detected and apoptosis-related genes are activated leading to cell death[10]. The inhibition of this type of apoptosis from the peroxide could be explained for Ebselen and Am-DPDS as they are present within the nucleus and so are able to prevent the peroxide initiating DNA damage.

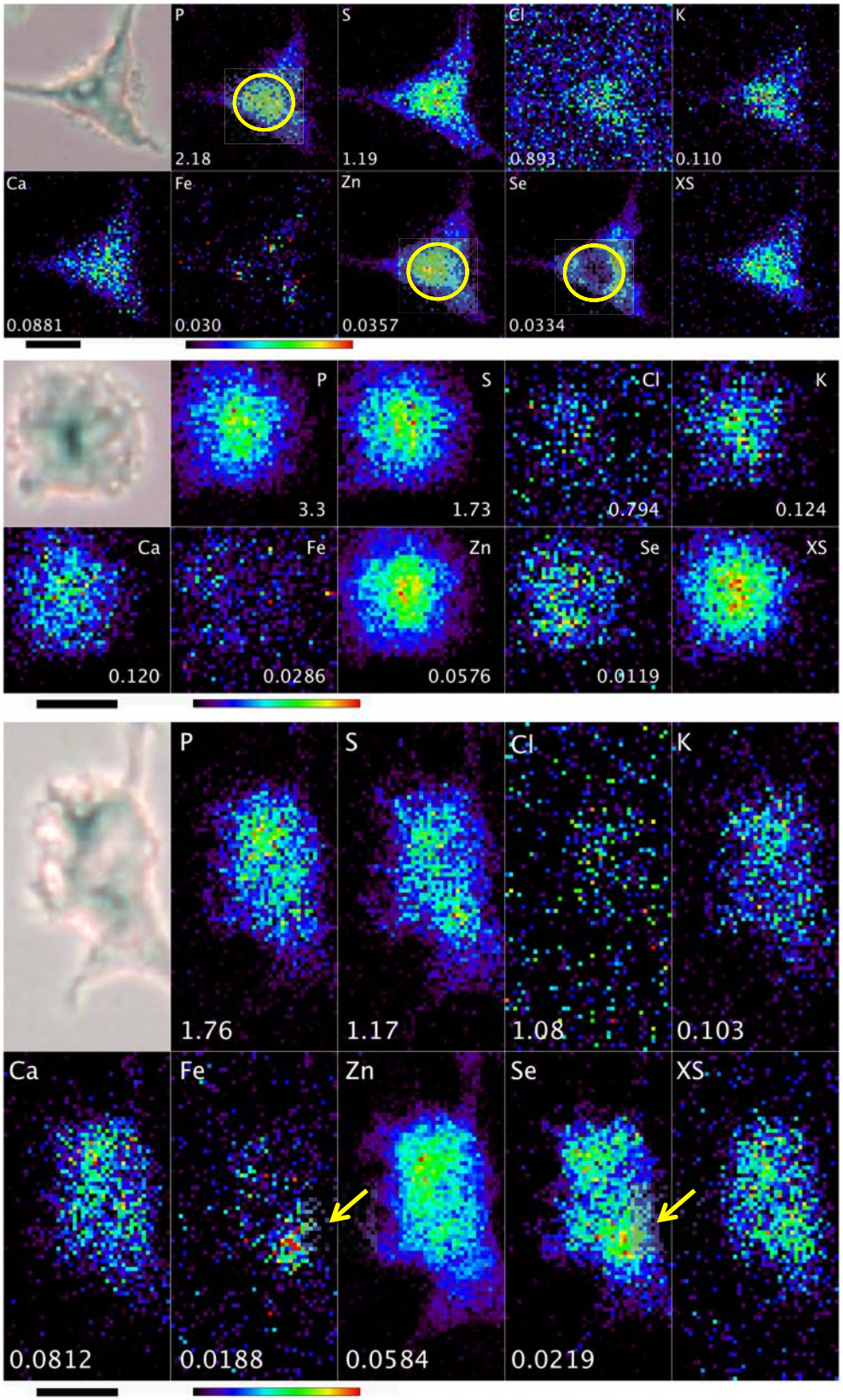

Figure 3.5.18 – Optical micrographs (top left), scattered X-ray (XS) and XFM elemental distribution maps of SH-SY5Y cells treated with 5 µM Ni-DPDS [top], 5 µM Am-DPDS [middle] and 10 µM Ebselen [bottom] for 24 h. Maximal elemental area density (quantified from standards and expressed in micrograms per square centimetre) is given in the bottom corner of each map. The nuclear region, identified by localisation of phosphorous and zinc, is circled. Arrows indicate a region that shared mutually high concentrations of iron and selenium. The black bar under the maps represents 10 µm.

From the XFM data the total average selenium content can be quantified for both the cell as a whole and just the nuclear fractions (Figure 3.5.19).

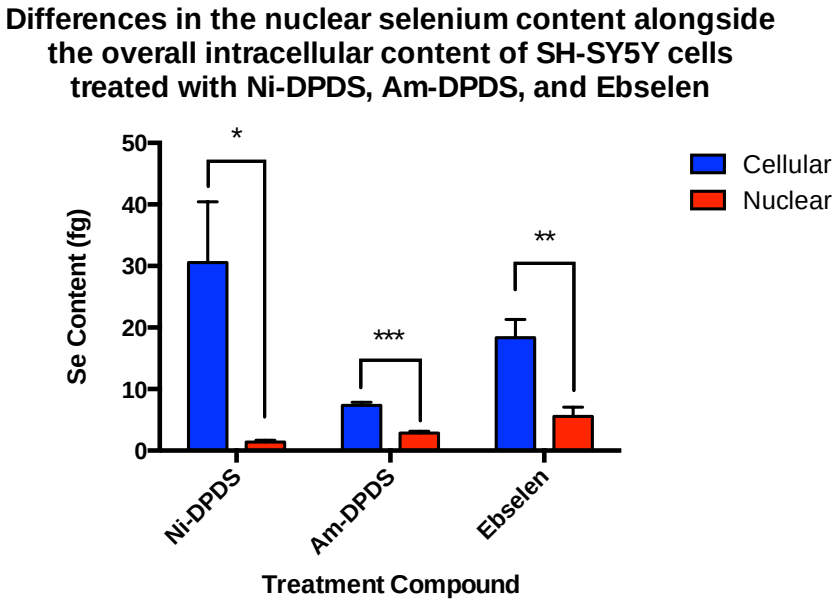

Figure 3.5.19 – Nuclear fraction of the selenium content within SH-SY5Y cells treated with 5 µM Ni-DPDS, Am-DPDS and 10 µM Ebselen as quantified by XFM studies, indicating the much lower fraction of Ni-DPDS present within the nuclear ROI compared to the other two treatments. * represents $p<0.05$, ** $p<0.001$, ***$p<0.0001$.

It is clear that Ni-DPDS treated cells have a much lower nuclear selenium content than the other two compound treated cells, at just 4.6% of the total intracellular selenium (Table 3.5.8). This non-zero value doesn't disprove that Ni-DPDS is excluded from the nucleus; instead it highlights one of the weaknesses of the XFM imaging process. XFM is a 2D imaging process, however the cells imaged were 3D, so while the nuclear region is identifiable from the image, there are still layers of cytoplasm and cellular membrane above and below the nuclear envelope that accounts for the non-zero Ni-DPDS content for the nuclear region.

Table 3.5.8 – Quantified average intracellular and nuclear selenium content in SH-SY5Y cells treated with 5 μM Ni-DPDS, Am-DPDS and 10 μM Ebselen, and the subsequent corresponding nuclear fraction percentage.

Treatment Compound	Cellular Content (fg)	Nuclear Content (fg)	Nuclear Fraction (%)
Am-DPDS	30 ± 10	1.4 ± 0.2	4.6
Ni-DPDS	7.4 ± 0.5	2.8 ± 0.3	38.6
Ebselen	18 ± 3	5.5 ± 1.5	30.2

The Am-DPDS and Ebselen treated SH-SY5Y cells showed much larger percentage nuclear selenium contents at 30.2 and 38.6 per cent respectively. These larger percentages show the abilities of the metabolites of each of these compounds to penetrate the nuclear envelope. When considered alongside the XFM maps, however, there was no clear localization, instead the selenium distributions appear to mirror changes in the total cell thickness as measured by the X-ray scatter (Figure 3.5.18).

Whilst bis(2-aminophenyl)diselenide was observed to enter the nuclear region (Figure 3.5.20, middle), total intracellular selenium concentrations were on average lower for the active Am-DPDS than for Ni-DPDS (Figure 3.5.20). Given that the XAS results showed that the Am-DPDS was cleaved within the cells, the difference in nuclear concentrations may be due to differences in the binding of the two compounds' metabolites with importin or their diffusion through the nuclear pores. Importin-interaction is critical for nuclear importation of small molecules, with it being responsible for all non-diffusion driven transport into the nucleus.[10]

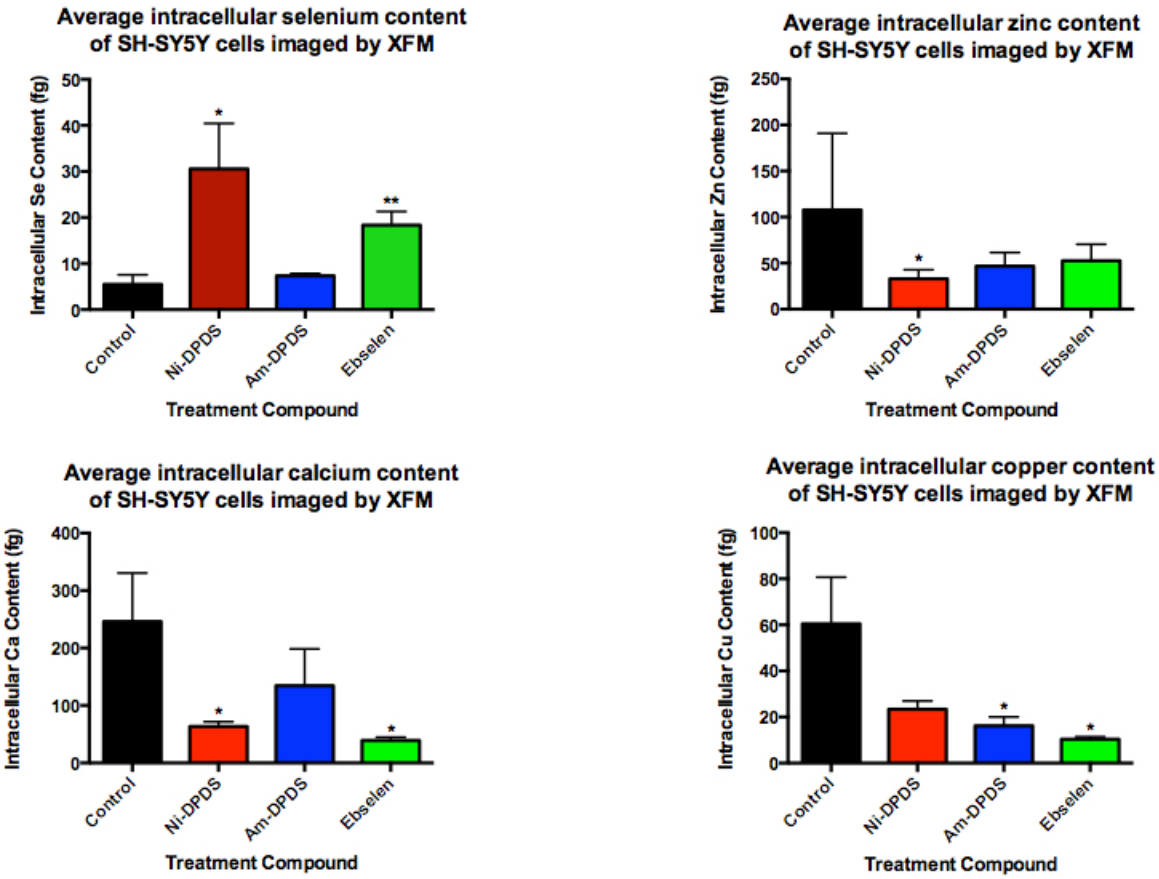

Figure 3.5.20 – Intracellular concentrations of selenium and other biologically relevant elements within SH-SY5Y cells treated with 5 µM Ni-DPDS, Am-DPDS and 10 µM Ebselen as quantified by XFM studies. Graphs indicate that homeostasis is disrupted within the treated cells differently for some elements, while not significantly for others. * represents $p<0.1$, ** $p<0.05$.

Not all elements were similarly disrupted, for example K and S showed no statistically significant deviations from the control as a result of treatment with any of the compounds. However significant decreases in the calcium concentrations within the treated cells compared to the control after treatment with Ni-DPDS and Ebselen, but not Am-DPDS, are of particular interest.

Calcium mobilization from the endoplasmic reticulum to the cytosol is known to activate apoptosis.[103-105] The signalling cascade features the exodus of cytochrome C and subsequent activation of caspase and nuclease enzymes that lead ultimately to cell death.[103,106] As a result the homeostasis of Ca^{2+} is a finely tuned intracellular event with balance afforded by anti- and pro-apoptotic proteins storing Ca^{2+} in the ER.[104,105]

The fluctuations in intracellular calcium concentrations, therefore, point towards a dysfunction of calcium homeostasis that would ultimately be detrimental to cell survival. The statistically significant decreases in intracellular calcium concentrations would indicate dysfunction within the Ni-DPDS and Ebselen treated cells, but not in the Am-DPDS treated cells.

Further inferences from the XFM imaging for the Am-DPDS were difficult due to the distribution of selenium generally following the thickness of the cell, shown by a general positive correlation between the Se and scatter maps (Figure 3.5.21, top left). The positive correlation between selenium concentration and cell thickness is not as strong as the trend of Zn with the X-ray scatter maps (Figure 3.5.21, top right), but this could be due to the relative concentrations, with the Zn giving a much stronger signal due to higher intracellular concentrations. The strongest, but least surprising, positive correlation is between phosphorous and zinc concentrations (Figure 3.5.21, bottom left), because they are largely localised within the nucleus and so are expected to be co-localised.

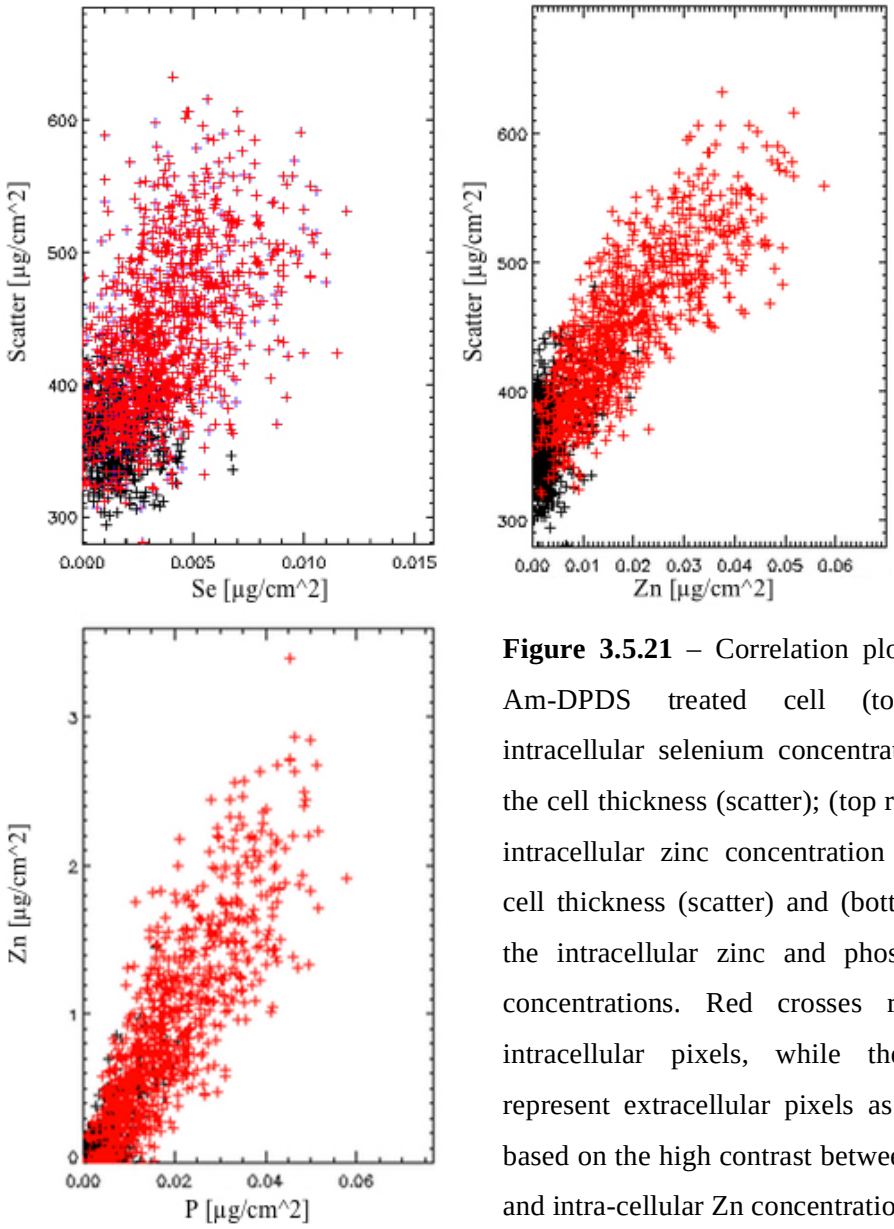

Figure 3.5.21 – Correlation plots for a Am-DPDS treated cell (top left) intracellular selenium concentration and the cell thickness (scatter); (top right) the intracellular zinc concentration and the cell thickness (scatter) and (bottom left) the intracellular zinc and phosphorous concentrations. Red crosses represent intracellular pixels, while the black represent extracellular pixels as defined based on the high contrast between extra- and intra-cellular Zn concentrations.

Ebselen was used once again used to make comparisons between the diselenides and a known therapeutic agent. It had been previously noted to have an interesting intracellular distribution in ND15 cells, with a localization with zinc but a separation from phosphorous.[86] In this study Ebselen, like the active Am-DPDS, showed the ability to enter the nucleus, with a localization with zinc and phosphorous (Figure 3.5.18, bottom).

However, given that Ebselen showed no protective action against oxidative stress induced cell death, the ability to enter the nucleus alone may not be the only requirement to assert protective ability. Instead it may be the metabolism of the Am-

DPDS to the intracellular reduced species in combination with the nuclear envelope penetration results in activity.

XFM is able to highlight treatment-derived fluctuations in the other elements due to disruptions to homeostasis. Calcium in particular is lower for the Ni-DPDS and Ebselen treated cells compared to the control, but not for Am-DPDS (Figure 3.5.20). However any generalisations about these trends and their intracellular ramifications is dampened somewhat given the small sample size available with only six cells imaged to represent each treatment condition.

Ebselen showed a possible co-localisation with iron (Figure 3.5.18, bottom), a Fenton oxidation agent. However given the overall extremely low concentration of iron it is difficult to quantify this co-localisation statistically. Visually there appears to be a subset of the iron (indicated with an arrow) that is co-localised with the selenium from the Ebselen. It is not clear if this has any bearing on the mechanism of action for Ebselen, but the co-localisation is present in future studies it could be an alternate source of protection if it prevents Fenton chemistry. Of note is that Ebselen did not follow the previously reported pattern of co-localisation with zinc and separation from phosphorous.[86]

3.6 Conclusions & Future Directions

3.6.1 Conclusions

Only Am-DPDS showed protective activity against oxidative stress induced damage in SH-SY5Y human neuroblastoma cells from MTT cytotoxicity assays, increasing the IC_{50} value of hydrogen peroxide treatment for 24 h from 1742 ± 29 μM to 2385 ± 108 μM. Ni-DPDS and Ebselen pre-treatment did not significantly alter the IC_{50} value, resulting in 1660 ± 29 μM and 1520 ± 50 μM respectively.

Synchrotron-based studies, XAS and XFM, indicated that Ni-DPDS remains largely unchanged within cells and is unable to penetrate into the nucleus, both of which limit its protective activity. XANES fitting of Ni-DPDS treated cells showed a dominant 60-89% Ni-DPDS fraction, with a smaller fraction of Se-C bonded character.

EXAFS for the Ni-DPDS treatments were consistent with their respective XANES results showing a carbon and selenium backscatterers at 1.87-1.89 Å and 2.34-2.36 Å respectively. These bond lengths were consistent with expected Se-C and Se-Se bonds lengths from literature for crystal structure data for similar substituted diphenyl diselenides. Despite possible Se-S binding identified in the XANES fitting, there was no corroborating evidence for such species from the EXAFS analysis. However, given the similar Se-S and Se-Se bond lengths, the presence of Se-S bonds may have been masked within the Fourier transform if they were only present at low concentrations.

Am-DPDS, however, was found to be reduced or have the diselenide bond cleaved inside cells and its metabolites were also able to enter nucleus. XANES fitting of treated cells showed only Se-C character, with 76-91% fit with methylselenocysteine and 9-34% fit with ι-selenomethionine. Noise levels hampered fitting of lower concentration samples, but as with the Ni-DPDS fits, all Am-DPDS fits generally produced results that were similar despite different oxidative stress conditions.

EXAFS further supported Am-DPDS's intracellular reduction by featuring two carbon backscatterers at 1.89-1.91 Å and no backscatteres at a distance consistent with Se-Se bond character within the Fourier transforms. The combination of reduction and nuclear penetration is assumed to give rise to the protective action observed for Am-DPDS against oxidative stress induced cell death.

Ebselen showed evidence of dimer formation inside cells with XANES fitting of treated SH-SY5Y cells being fit with 40-60% Ni-DPDS character, and XFM showed it to be

able to penetrate into the nucleus. XANES also showed Ebselen treated cells to have Se-S bonding character, being fit with a combined percentage of 18-26% with seleno-diglutathione and sulfoselenylcysteine characters. The lower concentration treated cell samples' spectral noise continued to hinder XANES fitting, but all spectra showed similar character. Given the lack of protective action against oxidative stress induced cell death in the MTT assays by Ebselen, the mechanism involving the dimer, although detected, may not be the GPx-like protective pathway.

Finally, the drug uptake levels were lowest for Am-DPDS, showing only a small amount was needed for protective action; this supports its GPx-like mode of action being catalytic like its parent compound DPDS. All three treatments disrupted homeostasis within the SH-SY5Y cells, as viewed through elemental fluctuations in treated cells compared to the untreated control cells. Not all elements were affected in the same fashion, with the homeostasis of signalling elements Zn and Ca being the most clearly disrupted.

3.6.2 Future Directions

The success of Am-DPDS as an antioxidant in cell based trials indicates that it is a candidate for further animal trials to confirm its protective abilities in larger scale, more complex biological systems. Ni-DPDS, while not seemingly as likely a candidate for further study due to its inactivity in cell based studies, may still show potential with different delivery systems. The cell based studies had cells pre-treated with the compounds directly into complete media, while interactions of the compounds with blood-albumin or gastric digestion would need to be investigated for applications with animal or human treatment.

Repeating the experiments in a differing brain cell model, or differentiating the SH-SY5Y blastoma cells to their neuronal phenotype, may provide a greater understanding of Ebselen's mode of action. Specifically a brain cell model where the drug shows protective action against oxidative stress induced cell death in toxicology experiments would be an appropriate system to test. Given the reported co-localisation with zinc and separation from phosphorous was not observed in the SH-SY5Y cell line, while it was in ND15 cells[86], this cell line may be a likely candidate with which to repeat the experiments. Otherwise the existing experiment could be altered by differentiating the

SH-SY5Y cells to a neuronal, rather than blastoma, phenotype and observing if this changes the outcomes for both speciation and distribution of Ebselen.

The three compounds were all being investigated as possible agents to limit the damage done to the brain during an ischaemic stroke event. One major factor that was not incorporated into the study was the effect the blood-brain barrier might have on the ability of the agent to reach their target brain cells. If the compounds were not able to cross the barrier then they would be unable to show any protective action within a living subject.

Finally, investigating Am-DPDS and its intracellular metabolites interactions with importin, the nuclear transport protein, could provide further insight into the differences in nuclear penetration between Ni-DPDS and Am-DPDS, and thus their respective protective abilities.

3.7 Acknowledgements

Access to both the SH-SY5Y cells as well as cell-culture laboratory, pivotal to the experiments, were provided by Ian Musgrave (The University of Adelaide).

X-ray fluorescence imaging for this research was carried out at the Advanced Photon Source (APS), a part of the Argonne National Labs, a U.S. Department of Energy (DOE) Office of Science User Facility operated for the DOE Office of Science by Argonne National Laboratory under Contract No. DE-AC02-06CH11357. Furthermore, beam-line scientists Barry Lai[#] and Stefan Vogt[#] were instrumental with the collection of the XFM data.

The X-ray absorption spectroscopy research was undertaken on the XAS beamline at the Australian Synchrotron, Victoria, Australia, a part of ANSTO. I thank Drs Peter Kappen, Chris Glover and Bernt Johannessen (XAS) for their assistance. I acknowledge travel funding provided by the International Synchrotron Access Program (ISAP) managed by the Australian Synchrotron and funded by the Australian Government and research funding from the Australian Research Council (DP140100176 to HHH).

[#]Advanced Photon Source, X-ray Science Division, Argonne National Laboratory, Argonne, IL 60439, USA

3.8 References

(1) Adibhatla, R. M.; Hatcher, J. F. *Antiox. Redox Signal.* **2003**, *5* (5), 647.

(2) Allen, C. L.; Bayraktutan, U. *Int. J. Stroke* **2009**, *4* (6), 461.

(3) Saeed, S. A.; Shad, K. F.; Saleem, T.; Javed, F.; Khan, M. U. *Exp. Brain. Res.* **2007**, *182* (1), 1.

(4) Carden, D. L.; Granger, D. N. *J. Pathol.* **2000**, *190* (3), 255.

(5) Adibhatla, R. M.; Hatcher, J. F. *Neurochem. Res.* **2005**, *30* (1), 15.

(6) Wood, A.; Brott, T. *N. Engl. J. Med.* **2000**, *343* (10), 710.

(7) Phan, T. G.; Wright, P. M.; Markus, R.; Howells, D. W.; Davis, S. M.; Donnan, G. A. *Clin. Exp. Pharmacol. Physiol.* **2002**, *29* (1-2), 1.

(8) Chan, P. H. *Brain Pathol.* **1994**, *4* (1), 59.

(9) Siesjö, B. K.; Agardh, C. D.; Bengtsson, F. *Cerebrovasc Brain Metab Rev* **1989**, *1* (3), 165.

(10) Elliot, W. H.; Elliot, D. C. *Biochemistry and Molecular Biology*, Third Ed.; Oxford Univ Press: New York, 1997.

(11) Zedehvakili, B. Design, Synthesis and Structure-Activity Relationships of Some Novel Thiol Peroxidase Mimics, University of Otago, Dunedin, New Zealand.

(12) Lane, N. *Oxygen: the molecule that made the world*; 2002.

(13) Shahidi, F.; Zhong, Y. *Journal of Functional Foods* **2015**.

(14) Muller, A. *Biochem. Pharmacol.* **1984**, *33* (20), 3235.

(15) Dawson, D. A.; Masayasu, H.; Graham, D. I.; Macrae, I. M. *Neurosci. Lett.* **1995**, *185* (1), 65.

(16) Yamaguchi, T.; Sano, K.; Takakura, K.; Saito, I.; Shinohara, Y.; Asano, T.; Yasuhara, H. *Stroke* **1998**, *29*, 12.

(17) Ogawa, A.; Yoshimoto, T.; Kikuchi, H.; Sano, K.; Saito, I.; Yamaguchi, T.; Yasuhara, H. *Cerebrovasc. Dis.* **1999**, *9* (2), 112.

(18) Orian, L.; Toppo, S. *Free Rad. Biol. Med.* **2014**, *66*, 65.

(19) Giles, G. I.; Giles, N. M.; Collins, C. A.; Holt, K.; Fry, F. H.; Lowden, P. A. S.; Gutowski, N. J.; Jacob, C. *Chem. Commun. (Camb.)* **2003**, No. 16, 2030.

(20) Giles, G. I.; Tasker, K. M.; Johnson, R.; Jacob, C. *Chem. Commun.* **2001**, 2490.

(21) Engman, L.; Tunek, A.; Hallberg, M.; Hallberg, A. *Chem. Bio. Interact.* **1994**,

93, 129.

(22) Sies, H. *Method. Enzymol.* **1994**, *234* (47), 476.

(23) Wendel, A.; Fausel, M.; Safayhi, H.; Tiegs, G.; Otter, R. *Biochem. Pharmacol.* **1984**, *33* (20), 3241.

(24) Sies, H. *Antioxidants in disease mechanisms and therapy*; Academic Press, 1996.

(25) Maiorino, M.; Roveri, A.; Coassin, M.; Ursini, F. *Biochem. Pharmacol.* **1998**, *37* (11), 2267.

(26) Morgenstern, R.; Cotgreave, I. A.; Engman, L. *Chem. Bio. Interact.* **1992**, *84*, 77.

(27) Sies, H. *Free Rad. Biol. Med.* **1993**, *14*, 313.

(28) Sies, H.; Masumoto, H. *Adv. Pharmacol.* **1996**, *38*, 229.

(29) Schewe, T. *Gen. Pharmac.* **1995**, *26* (6), 1153.

(30) Nogueira, C. W.; Rocha, J. B. T. *Chem. Rev.* **2004**, *104* (12), 6255.

(31) Fischer, H.; Dereu, N. *Bull. Soc. Chim. Belges* **2010**, *96* (10), 757.

(32) Cotgreave, I. A.; Morgenstern, R.; Engman, L.; Ahokas, J. *Chem. Bio. Interact.* **1992**, *84* (1), 69.

(33) Sarma, B. K.; Mugesh, G. *Journal of the American Chemical Society* **2005**, *127* (32), 11477.

(34) Zucker, P. A.; Huang, R.; Spector, A.; Wilson, S. *Journal of the American Chemical Society* **1989**, 5936.

(35) de Freitas, A. S.; Funck, V. R.; Santos Rotta, dos, M. *Brain Res. Bull.* **2009**, *79*, 77.

(36) Meotti, F. C.; Borges, V. C.; Zeni, G.; Rocha, J. B. T.; Nogueira, C. W. *Toxicol. Lett.* **2003**, *143* (1), 9.

(37) Luchese, C.; Brandão, R.; de Oliveira, R.; Nogueira, C. W. *Toxicol. Lett.* **2007**, *173*, 181.

(38) Borges, L. P.; Brandão, R.; Godoi, B.; Nogueira, C. W.; Zeni, G. *Chem. Bio. Interact.* **2008**, *171* (1), 15.

(39) Stangherlin, E. C.; Luchese, C.; Ardais, A. P.; Nogueira, C. W. *Inhal Toxicol* **2009**, *21* (10), 868.

(40) Brandão, R.; Acker, C. I.; Leite, M. R.; Barbosa, N. B. V.; Nogueira, C. W. *J Appl Toxicol* **2009**, *29* (7), 612.

(41) Ibrahim, M.; Luchese, C.; Pinton, S.; Roman, S. S.; Hassan, W.; Nogueira, C.

W.; Rocha, J. B. T. *Exp. Brain. Res.* **2011**, *63* (4), 331.

(42) Nogueira, C. W.; Quinhones, E. B.; Jung, E. A. C.; Zeni, G.; Rocha, J. B. T. *Inflamm. Res.* **2003**, *52* (2), 56.

(43) Savegnago, L.; Trevisan, M.; Alves, D.; Rocha, J. B. T.; Nogueira, C. W.; Zeni, G. *Environ. Toxicol. Pharmacol.* **2006**, *21* (1), 86.

(44) Corte, C. D.; Soares, F.; Aschner, M.; Rocha, J. *Tetrahedron* **2012**, *68*, 10437.

(45) Nogueira, C. W.; Rocha, J. *J. Braz. Chem. Soc.* **2010**, *21* (11), 2055.

(46) Posser, T.; de Paula, M. T.; Franco, J. L.; Leal, R. B.; da Rocha, J. B. T. *Arch. Toxicol.* **2011**, *85* (6), 645.

(47) Nogueira, C. W.; Meotti, F. C.; Curte, E.; Pilissão, C.; Zeni, G.; Rocha, J. B. T. *Toxicology* **2003**, *183* (1-3), 29.

(48) Battin, E. E.; Perron, N. R.; Brumaghim, J. L. *Inorg. Chem.* **2006**, *45* (2), 499.

(49) Koningsberger, D. C.; Prins, R. *Nachr. Chem. Tech. Lab.* **1988**, *36* (6), 650.

(50) Pickering, I. J.; Brown, G. E., Jr; Tokunaga, T. K. *Enviro. Sci. Technol.* **1995**, *29* (9), 2456.

(51) McRae, R.; Bagchi, P.; Sumalekshmy, S. *Chem. Rev.* **2009**, *109*, 4780.

(52) Ascone, I.; Strange, R. *J. Synchrotron Radiat.* **2009**, *16*, 413.

(53) Weekley, C. M.; Aitken, J. B.; Vogt, S.; Finney, L. A.; Paterson, D. J.; de Jonge, M. D.; Howard, D. L.; Witting, P. K.; Musgrave, I. F.; Harris, H. H. *Journal of the American Chemical Society* **2011**, *133*, 18772.

(54) Hayes, K. F.; Roe, A. L.; Brown, G. E.; Hodgson, K. O.; Leckie, J. O.; PARKS, G. A. *Science* **1987**, *238* (4828), 783.

(55) Weekley, C. M.; Aitken, J. B.; Finney, L.; Vogt, S.; Witting, P. K.; Harris, H. H. *Nutrients* **2013**, *5* (5), 1734.

(56) Ortega, R.; Devès, G.; Carmona, A. *J. R. Soc. Interface* **2009**, *6* (Suppl. 5), S649.

(57) Prange, A.; Modrow, H. *Rev Environ Sci Biotechnol* **2002**, *1* (4), 259.

(58) George, G. N.; Hedman, B.; Hodgson, K. O. *Nat. Struct. Mol. Biol.* **1998**, *5*, 645.

(59) Malinouski, M.; Kehr, S.; Finney, L.; Vogt, S.; Carlson, B. A.; Seravalli, J.; Jin, R.; Handy, D. E.; Park, T. J.; Loscalzo, J.; Hatfield, D. L.; Gladyshev, V. N. *Antiox. Redox Signal.* **2012**, *16* (3), 185.

(60) Shanu, A.; Groebler, L.; Kim, H. B.; Wood, S.; Weekley, C. M.; Aitken, J. B.; Harris, H. H.; Witting, P. K. *Antiox. Redox Signal.* **2013**, *18* (7), 756.

(61) Weekley, C. M.; Aitken, J. B.; Vogt, S.; Finney, L. A.; Paterson, D. J.; de Jonge, M. D.; Howard, D. L.; Musgrave, I. F.; Harris, H. H. *Biochemistry* **2011**, *50* (10), 1641.

(62) Mosmann, T. *J. Immunol. Methods* **1983**, *65* (1-2), 55.

(63) Denizot, F.; Lang, R. *J. Immunol. Methods* **1986**, *89*, 271.

(64) Motulsky, H. J.; Brown, R. E. *BMC Bioinformatics* **2006**, *7*, 123.

(65) Huckaba, C. E.; Keyes, F. G. *Journal of the American Chemical Society* **1948**, *70* (4), 1640.

(66) Carter, E.; Rayner, B.; McLeod, A.; Wu, L. *Mol. Biosyst.* **2010**, *6*, 1316.

(67) Weekley, C. M.; Jeong, G.; Tierney, M. E.; Hossain, F.; Maw, A. M.; Shanu, A.; Harris, H. H.; Witting, P. K. *J. Biol. Inorg. Chem.* **2014**, *19* (6), 813.

(68) Weekley, C. M.; Shanu, A.; Aitken, J. B.; Vogt, S.; Witting, P. K.; Harris, H. H. *Metallomics* **2014**, *6* (9), 1602.

(69) Aitken, J. B.; Antony, S.; Weekley, C. M.; Lai, B.; Spiccia, L.; Harris, H. H. *Metallomics* **2012**, *4* (10), 1051.

(70) McRae, R.; Lai, B.; Vogt, S.; Fahrni, C. J. *J. Struct. Bio.* **2006**, *155* (1), 22.

(71) McRae, R.; Lai, B.; Fahrni, C. J. *Metallomics* **2013**, *5* (1), 52.

(72) McRae, R. Investigating metal homeostasis in mammalian cells using high resolution imaging techniques, Georgia Institute of Technology, 2010.

(73) Vogt, S. *J. Phys. IV France* **2003**, *104*, 635.

(74) Van Espen, P. In *Handbook of X-Ray Spectrometry*; Van Grieken, R. E., Markowicz, A. A., Eds.; CRC Press, 2002; Vol. 29.

(75) Whittemore, E. R.; Loo, D. T.; Watt, J. A.; Cotman, C. W. *Neuroscience* **1995**, *67* (4), 921.

(76) Buckman, J. F.; Hernández, H.; Kress, G. J.; Votyakova, T. V.; Pal, S.; Reynolds, I. J. *J. Neurosci. Methods* **2001**, *104* (2), 165.

(77) Pendergrass, W.; Wolf, N.; Poot, M. *Cytometry Part A* **2004**, *61A*, 162.

(78) Dringen, R.; Kussmaul, L.; Hamprecht, B. *Brain Res. Brain Res. Protoc.* **1998**, *2* (3), 223.

(79) Gülden, M.; Jess, A.; Kammann, J.; Maser, E.; Seibert, H. *Free Rad. Biol. Med.* **2010**, *49* (8), 1298.

(80) Hirsch, I.; Prell, E.; Weiwad, M. *Anal. Biochem.* **2014**, *456*, 22.

(81) Whittemore, E. R.; Loo, D. T.; Cotman, C. W. *Neuroreport* **1994**, *5* (12), 1485.

(82) Lennon, S. V.; Kilfeather, S. A.; Hallett, M. B.; Campbell, A. K.; Cotter, T. G. *Clin. Cancer Res.* **1992**, *87* (3), 465.

(83) Ueda, N.; Shah, S. V. *Am. J. Physiol.* **1992**, *263* (2 Pt 2), F214.

(84) Hockenbery, D. M.; Oltvai, Z. N.; Yin, X. M.; Milliman, C. L.; Korsmeyer, S. J. *Cell* **1993**, *75* (2), 241.

(85) Kane, D. J.; Sarafian, T. A.; Anton, R.; Hahn, H.; Gralla, E. B.; Valentine, J. S.; Ord, T.; Bredesen, D. E. *Science* **1993**, *262* (5137), 1274.

(86) Aitken, J. B.; Lay, P. A.; Duong, T. T. H.; Aran, R.; Witting, P. K.; Harris, H. H.; Lai, B.; Vogt, S.; Giles, G. I. *J. Biol. Inorg. Chem.* **2012**, *17* (4), 589.

(87) Choi, B.-S.; Sapkota, K.; Kim, S.; Lee, H. J.; Choi, H.-S.; Kim, S.-J. *Neurochem. Res.* **2010**, *35* (8), 1269.

(88) Jung, C. H.; Hong, M. H.; Kim, J. H.; Lee, J. Y.; Ko, S. G.; Cho, K.; Seog, H. M. *J. Pharm. Pharmacol.* **2007**, *59* (3), 455.

(89) Masaki, H.; Okano, Y.; Sakurai, H. *Archives of dermatological research* **1998**.

(90) Baud, O.; Greene, A. E.; Li, J.; Wang, H.; Volpe, J. J.; Rosenberg, P. A. *J. Neurosci.* **2004**, *24* (7), 1531.

(91) Iwaoka, M.; Tomoda, S. *Journal of the American Chemical Society* **1994**, *116*, 2557.

(92) Marsh, R. E. *Acta Crystallogr.* **1952**, *5*, 458.

(93) Morris, G. D.; Einstein, F. *Acta Crystallogr. C Struct. Chem.* **1986**, *C42*, 1433.

(94) Shimadzu. *www.shimadzu.com*. January 2016, p 4.

(95) Zierkiewicz, W.; Wójtowicz, H.; Michalska, D. *Polyhedron* **2011**, *30*, 2466.

(96) Radatz, C. S.; Alves, D.; Schneider, P. H. *Tetrahedron* **2013**, *69*, 1316.

(97) de Freitas, A. S.; de Souza Prestes, A.; Wagner, C. *Molecules* **2010**, *15*, 7699.

(98) Rosa, R. M.; Roesler, R.; Braga, A. L.; Saffi, J.; Henriques, J. A. P. *Braz. J. Med. Biol. Res.* **2007**, *40* (10), 1287.

(99) Allen, F. H.; Kennard, O.; Watson, D. G.; Brammer, L. *J. Chem. Soc.* **1987**, S1.

(100) Jin, Q.; Lai, B.; Chen, S.; Gleber, S. C. *Microsc. Microanal. 21* **2015**, *S3* (439), 877.

(101) Berg, J. M. *Curr. Opin. Struct. Biol.* **1993**, *3*, 11.

(102) Gardner, A. M.; Xu, F. H.; Fady, C.; Jacoby, F. J.; Duffey, D. C.; Tu, Y.;

Lichtenstein, A. *Free Rad. Biol. Med.* **1997**, *22* (1-2), 73.

(103) Mattson, M. P.; Chan, S. L. *Nat Cell Biol* **2003**, *5* (12), 1041.

(104) Hajnóczky, G.; Davies, E.; Madesh, M. *Biochem. Biophys. Res. Commun.* **2003**, *304* (3), 445.

(105) Pinton, P.; Giorgi, C.; Siviero, R.; Zecchini, E.; Rizzuto, R. *Oncogene* **2008**, *27*, 6407.

(106) Pigozzi, D.; Tombal, B.; Ducret, T.; Vacher, P.; Gailly, P. *Cell Calcium* **2004**, *36* (5), 421.

CHAPTER 4. Fluorescence and XFM studies into the anticancer mode of action of the ruthenium-based anti-cancer agent NKP-1339 within A549 human lung adenocarcinoma epithelial cells.

Jason Wedding, Hugh Harris*

*School of Physical Sciences, The University of Adelaide, South Australia, 5005, Australia

4.1 Abstract

The purported anticancer mode of action of a KP1019 analogue, NKP-1339, within human lung adenocarcinoma epithelial cells (A549) was investigated using synchrotron-based X-ray fluorescence microscopy. A preliminary study showed a tentative co-localisation of NKP-1339, or its ruthenium-containing metabolites, with intracellular iron and copper. A follow-up study attempted to visualise a mitochondrial compartmentalisation of the NKP-1339 or its ruthenium-based metabolites utilising a combination of optical and synchrotron-based fluorescence microscopy. Results appeared to support that NKP-1339 was a KP1019 analogue, with prominent cellular uptake. The initially tentative co-localisation with iron was observed again, suggesting a possible role by Fenton chemistry in the anticancer action. Furthermore, X-ray fluorescence showed that the two chosen mitochondrial probes; MitoTracker DeepRed and MitoTracker Orange, perturbed homeostasis in different ways. This highlights the importance of thorough consideration of the effects of probes for future studies, and the need for careful attention to the controls to understand these probe-based perturbations.

4.2 Abbreviations

A549	human lung adenocarcinoma epithelial cells;
apoTf	apotransferrin;
GSH	glutathione;
HSA	human serum albumin;
ICP-MS	inductively coupled plasma mass spectrometry;
KP1019	trans-[tetrachlorobis(1 H-indazole)ruthenate(III)]
NAMI-A	imidazolium trans-imidazoledimethyl sulfoxide-tetrachlororuthenate;
PIPES	piperazine-N,N′-bis(2-ethanesulfonic acid);
RAPTA	ruthenium–arene complexes bearing the 1,3,5-triaza-7-phosphatricyclo-[3.3.1.1]decane ligand and a η^6-arene ligand;
VEGF	Vascular endothelial growth factor;
XFM	X-ray fluorescence microscopy

4.3 Introduction

Interest in ruthenium-based anticancer agents has increased since the completion of phase I clinical trials by NAMI-A[1-3] and KP1019[4-6] (Scheme 1), such that the study of ruthenium-based drugs is an expanding field of bioinorganic chemistry.[7,8] The history of ruthenium anticancer agents is inextricably tied to the discovery of the platinum-based anticancer agent cisplatin by Rosenberg in 1965[9].[6,10] While the biological activities of ruthenium complexes were recognised prior to the discovery of cisplatin by Dwyer in the 1950s[11,12], they were largely forgotten until the success of cisplatin.[8,13]

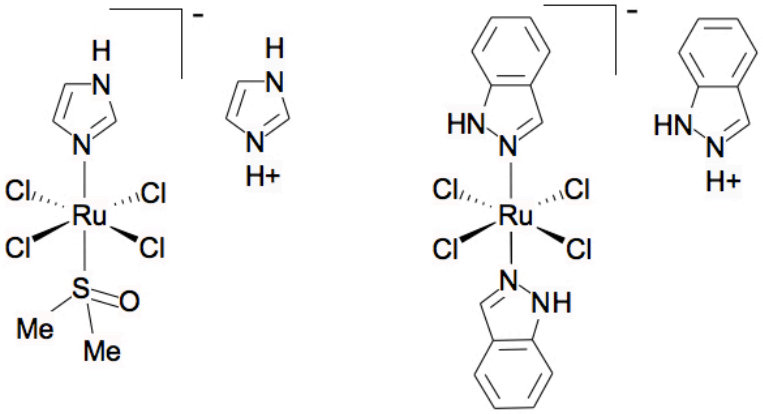

Scheme 1 – Structures of ruthenium-based anticancer agents that have been clinically investigated: NAMI-A[1-3] (left) and KP1019[4-6] (right).

4.3.1 Cisplatin

Cisplatin (Scheme 2) and its analogues are still among the most effective anticancer agents in clinical usage, often employed in the treatment of germline cancers.[6,10,14,15] Under physiological conditions cisplatin is thought to undergo intracellular aquation, exchanging the chlorido ligands with water, partial hydrolysis and subsequently binds to DNA, and other macromolecules[8,16], stimulating apoptosis.[8,17,18] Extracellular (e.g. serum albumin[8,19,20]) and intracellular (e.g. GSH[8,16,21]) protein and small molecule binding are competing, unwanted processes which limit the activity of cisplatin and lead to its harsh side effect profile.

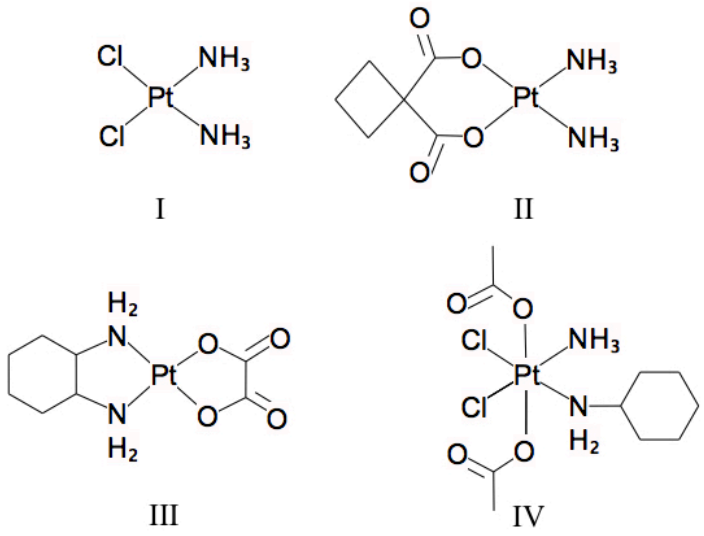

Scheme 2 – Structures of platinum-based anticancer agents: cisplatin (I), carboplatin (II), oxaliplatin (III), and satraplatin (IV).

Due to the high systematic toxicity of cisplatin, along with the propensity of tumours to develop resistance[7,10,22,23], cisplatin is commonly used in combination therapy in conjunction with other anticancer agents[24]. Toxicity towards rapidly dividing cells including hair follicles, bone marrow and gastrointestinal tract cells leads to hair loss, anaemia and neutropenia in patients.[6,25] Developing alternatives that do not suffer from these inherent side effects has been the driving force behind the development of more platinum-based drugs.[24,26-30] Ideally these alternatives would have lower toxicity, fewer problems with resistance development (acquired and intrinsic) and activity against a boarder range of tumours.[7,24,26]

Despite the extensive trialling of platinum-based analogues for similar anticancer activity, only an additional two have reached clinical use; carboplatin and oxaliplatin.[16,18,22,30,31] Carboplatin has a reduced toxicological profile, but similar spectrum of activity to cisplatin; while oxaliplatin has shown strong activity against colorectal cancer derived tumours.[10] More recently, with a differing approach of using a Pt(IV) pro-drug that is intracellularly reduced to produce toxic Pt(II) moieties, orally active satraplatin was discovered.[6,32] The lack of successful throughput of potent cisplatin analogues provided the motivation to explore the activity of other transition metal complexes.[8]

4.3.2 Ruthenium-based anticancer alternatives

Ruthenium was a strong alternative to platinum as it had a previously documented rich synthetic history, and a large range of oxidation states accessible under

biological conditions.[8,10,33,34] Having access to multiple oxidation states is significant as the oxidation state affects the activities of most metal-based anticancer agents.[6] Unlike cisplatin, which displays strong anticancer activity to primary tumours[3,7,35], ruthenium-based anticancer agents display a more complex, multi-faceted anticancer activity that cannot be explained by the model that exists for cisplatin.[3,8,36-39]

NAMI-A is one of the two most successful ruthenium-based anticancer agents and shows strong anti-metastatic activity[10,40,41], in particular against lung cancers and solid metastases.[1,42,43] NAMI-A was the first ruthenium-based anticancer agent to enter clinical trials[6,40], and is one of only two ruthenium-based compounds (alongside KP1019) to have completed phase I trials.[8,44-46] It has been shown to be effective in reducing metastasis independently of any reduction of primary tumour growth.[3,6,47] NAMI-A is a Ru^{III} pro-drug that undergoes rapid aquation and hydrolysis within minutes[8,48] losing its original ligands, which takes hours for cisplatin in aqueous solutions.[3,36]

When NAMI-A was screened for cytotoxicity against the more common cancer cell lines it showed no activity.[3,49] Instead it has been shown to be over a thousand times less toxic than cisplatin.[3] While its mechanism of action has been source of ample debate; it has been shown that the activity of NAMI-A is not related to intracellular DNA binding, instead displaying very poor cellular uptake.[3,50] Instead it interacts with actin-type proteins[3,51,52] on the cell surface or collagen within the extracellular matrix[3,42,53], which reduces invasive cancer cell mobility. It has also been shown to rapidly bind to serum proteins (HSA and apoTf), expected to assist with its transport after administration.[7,39,54-58] NAMI-A has also been shown to inhibit angiogenesis by VEGF[3,59], which is a key component for tumour development and continued growth.

Concurrent with the development of NAMI-A, Keppler and co-workers developed another Ru^{III} anticancer agent called KP1019.[8] KP1019 has shown high cytotoxicity against primary tumours[7,60], much like platinum-based anticancer agents.[7,35] Most notably, it has been shown to be effective against cisplatin-resistant colorectal tumours.[4,8,10,39] It has also been effective against primary explanted human tumours in rats.[4,10,38,61] While KP1019 was initially thought to not have any anti-metastatic activity[8,10], that has since been called into question.[39,62]

KP1019, like NAMI-A, is a pro-drug but it is more stable against aquation and hydrolysis and shows much greater cellular uptake.[8,63-65] Its activity has been posited to be due to changes in oxidation states, much like cisplatin, but there is limited direct evidence of this reduction in vivo.[8,10] Recently, the activation of KP1019 has been linked to the redox state of the tissues it is contained within, with a change in speciation in hypoxic environments observed for spheroids.[39] This intracellular reduction is thought to be by endogenous glutathione.[6] While it can be reduced by ascorbate in solution[39,54,66], Ru^{III} has been found to be the dominant oxidation state of Ru-serum adducts[7,39,54,67,68], therefore intracellular reduction is thought to direct its activity.

Transport into cells was thought to be assisted by transferrin[6,68,69], because analogues that bound less-well to transferrin exhibited less activity[6,64]. However, recently transferrin transport as a mechanism of uptake and release into the cytosol has been criticised due to inconsistencies with similar observations for transferrin-assisted gallium uptake.[3] Metals, other than iron, bind to transferrin with similar affinity and yet are not internalised.[3,70] Furthermore it has been found that the ruthenium moieties bind non-specifically to transferrin rather than at the Fe^{III}-binding sites in solution.[3,7] Finally, as with gallium, even if taken into the cell there is no evidence it is released into the cytosol, instead it would likely stay trapped within the endosomes.[3]

Instead passive diffusion has now resurged in popularity to account for the cellular uptake of KP1019 that has been observed.[7] Its ability to disrupt, whether directly or indirectly, the iron distribution in treated cells still accounts, at least in part, for its toxicity.[3,50] Due to its similar activity profile to cisplatin, DNA is the expected target for KP1019[50], however the resulting DNA lesions differ between to the two agents.[4,6,71]

More recently a large range of new ruthenium-based agents have been categorized, including organometallic arene-ruthenium complexes[6,72] and arene PTA ruthenium(II) [RAPTA-type] complexes[6]. The advantages of RAPTA-type complexes being generally greater stability in air as well as good thermodynamic stability, providing better properties for clinical usage.[6] Their activity, being potent against secondary metastasis but inactive against primary tumours, largely mirrors that of NAMI-A and so both are thought to have similar targets.[6,73] Non-orthodox approaches such as new tri-nuclear Ru-arene clusters have also been found to be

highly cytotoxic to ovarian cancer cell lines, much more so than the pre-existing tetra-clusters.[6,8,74-76]

4.3.3 NKP-1339

NKP-1339 is the more water-soluble, sodium salt of KP1019; and has completed phase I and II clinical trials.[64,77] It has shown to be potent against neuroendocrine tumours (NET)[77]; and is known to generate intracellular ROS probably by redox-induced redox cycling[78,79]; and cause apoptosis-regulated cell death via the mitochondrial pathway[64,80]. NKP-1339 has also been shown to enhance the anticancer activity of sorafenib in vitro and in vivo; as well as arresting the cell cycle in the G2/M phase.[81]

4.3.4 Experimental aims

This experiment aims to investigate the intracellular fates of NKP-1339 by using X-ray fluorescence microscopy (XFM) to probe its mechanism of anticancer action. This follows the success of Aitken et. al.[50] who used XFM to investigate the cellular fates of NAMI-A and KP1019 to confirm the lack of cellular uptake of NAMI-A and the DNA targeting of KP1019. Synchrotron techniques have become a leading tool for the determination of speciation and distribution of heavy metals in biological environments.[7,82]

XFM allows for the non-destructive, i.e. no need for pre-imaging chemical digestion, mapping of trace element distribution in biological samples at the cellular scale.[83,84] Targeted cells are scanned through the X-ray beam, with the resultant fluorescence collected at discreet points to produce pixels. The spectrum at each point is then fitted and calibrated to produce elemental maps for each excited element. The excitation required to produce ruthenium K-line fluorescence is significantly higher than that necessary to excite other biologically relevant elements such as Se, P, S, Ca, Zn, and Fe. As such, to image ruthenium in cells in addition to the lighter elements, two scans for each cell, one at a higher 22 keV for ruthenium excitation and one at a lower energy 10 keV to allow sufficient sensitivity for the other biologically relevant elements, must be collected and collated. Ruthenium is not an endogenous element, and so any ruthenium detected results from the ruthenium-agent administration.

XFM has been used, in addition to the study by Aitken et. al.[50], to monitor the intracellular distribution of ruthenium as well as platinum post anticancer agent

administration.[85-88] XFM has also been used to monitor distribution and speciation within biological tissues[39,88], as well as to determine ruthenium- and platinum-protein interactions from electrophoresis gel analyses[85,89-91]. XFM can provide information about the role of transferrin[58], potentially the role of reduction in the mechanism of action[10], and examine how the biochemistry of the treated cell changes due to the drugs effects[92,93].[8]

4.4 Materials & Methodology

4.4.1 Materials

4.4.1.1 Cell culture solutions and reagents

Dulbecco's Modified Eagle's Medium (DMEM; Gibco 11995-065) was supplemented with foetal bovine serum (FCS, Bovogen Biologicals SFBS), non-essential amino acid solution (NEAA; Sigma Life Sciences M7145), penicillin-streptomycin solution (Pen-Strep; 10,000 U mL-1 penicillin and 10,000 µg mL-1 streptomycin; Gibco 15140-122), L-Glutamine (2 mM) and trypsin-EDTA (Gibco BRL 20 mL) were kept at 253 K for long-term storage and 277 K for short-term storage. Subculture media was DMEM with a 5% FCS, 1% NEAA, Pen-Strep, L-Glu supplementation, while treatment media had only 1% NEAA, Pen-Strep and L-Glu supplementation. Dimethyl sulfoxide (DMSO; CAS 67-68-5) was purchased from Chem-Supply (DA013-500M).

4.4.1.2 NKP-1339 treatment solutions

NKP-1339 (acquired from Niiki Pharma) treatment solutions were prepared as mandated by Niiki Pharma. A 200 mM dark brown colour stock solution was made through the addition of 500 µL of 100% dimethyl sulfoxide (DMSO) to the 50 mg of compound. The stock solution was then aliquoted into micro-centrifuge tubes for single use and stored at -20 °C. At time of treatment, a frozen aliquot was quickly thawed in water bath (30 ^{o}C) and used immediately. The 200 mM stock solution was intermittently vortexed over 5-10 seconds to assure a uniform solution and then diluted 2,000x using serum-free subculture media to yield a 100 µM NKP-1339 (0.05% DMSO) treatment solution.

4.4.1.3 MitoTracker fluorescence probes treatment solutions

MitoTracker Orange CMTMRos (M-7510) and MitoTracker Deep Red FM (M22426) were sourced from Life Technologies, a brand of Thermo Fisher Scientific. MitoTracker Deep Red and MitroTracker Orange treatment solutions were prepared by dissolving the respective compounds (50 µg) in DMSO to produce 1 mM solutions. These were then diluted to the necessary treatment concentrations of 10 nM (0.001% DMSO) using serum-free subculture media.

4.4.1.4 Cell fixation solutions

Paraformaldehyde (Sigma Aldrich, CAS 68476-52-8, 95%) was dissolved in phosphate buffered saline (PBS) to prepare a 10% w/v solution. The pH was adjusted to 7.4 using 0.1 M NaOH and 0.1 M HCl with the aid of a pH meter. Then a subsequent 1% w/v paraformaldehyde solution was prepared by diluting with PBS buffer solution. Piperazine-N,N'-bis(2-ethanesulfonic acid) (PIPES) sodium salt (Calbiochem, CAS 5625-37-6) and sucrose (AnalaR, CAS 57-50-1) were dissolved in MilliQ water to give a 20 mM PIPES/200 mM sucrose solution of pH 7.2.

4.4.2 Methodology

4.4.2.1 Cell Culture

A549 human lung adenocarcinoma epithelial cells originally purchased from the American Tissue Culture Collection. Cells were cultured as monolayers in complete Dulbecco's Modified Eagle's Medium (DMEM) supplemented with foetal bovine serum (2% v/v), L-glutamine (2 mM), antibiotic-antimyotic mixture (100 mg mL^{-1} penicillin and 100 U mL^{-1} streptomycin) and nonessential amino acids (100 U mL^{-1}) at 310 K in a 5% CO_2-humidified incubator and were subcultured every 3-7 days.

4.4.2.2 X-ray fluorescence imaging of unlabelled single cells (Advanced Photon Source)

4.4.2.2.1 Sample Preparation

Cells used in XFM imaging were grown on 1.5 × 1.5 mm^2 × 500 nm silicon nitride windows (Silson, UK) in 6-well plates as described previously.[94-98] In short, the plates were seeded at 1.8×10^5 cells/well in complete DMEM and were incubated at 310 K in a 5% CO_2-humidified incubator for 24 h prior to treatment. Cells were treated with 100 μM NKP-1339 for 1 h or 4 h; or 0.05% DMSO (in media) for 4 h as a vehicle-alone control. At the end of the treatment time the medium was removed and the cells were fixed with 1% paraformaldehyde solution (pH 7.2) for 20 min at room temperature, before being washed with a 20 mM PIPES/ 200 mM sucrose buffer solution (pH 7.2) thrice.

4.4.2.2.2 Data Collection

XFM elemental distribution maps of single cells were recorded on beamline 2-ID-D at the Advanced Photon Source (APS), Argonne National Laboratory, Illinois, USA.

At the APS, the beam was tuned to an incident energy of 10.0 keV using a Si(111) double crystal monochromator for most elements and 22.0 keV for the collection of ruthenium data, and was focused to a diameter of 0.75 μm using a "high-flux" zone plate. A single element silicon drift energy dispersive detector (Vortex EX, SII Nano-technology, Northridge, CA), at 90^{o} to the incident beam, was used to collect the fluorescence signal for 0.5 s per spatial point from samples under a He atmosphere.

Four to eight individual cells per sample were selected and located using an optical microscope (Leica DMRXE). Cells were subsequently relocated in the beamline by correlating the light microscope coordinates with those determined from the X-ray transmission image of the window as viewed on a CCD camera. Whole cells were raster scanned using a 25 nm accuracy Newport sample positioning stage. Low resolution scans with a step size of 5 μm and a dwell time of 2 s were used to accurately locate the cells before obtaining high-resolution scans with a step size of 0.75 μm and a dwell time of 0.5 s.

4.4.2.2.3 Data Analysis

The fluorescence spectrum at each spatial point was fit to Gaussians, modified by the addition of a step function and a tailing function to describe mostly incomplete charge collection and other detector artefacts.[95,96] The integrated fluorescence spectra extracted from these regions were also fit with modified Gaussians to determine average elemental area densities (in units of μg cm^{-2}). Quantification was performed by comparison to the corresponding measurements on the thin-film standards NBS-1832 and NBS-1833 from the National Bureau of Standards (Gaithersburg, MD). The analysis was performed using MAPS software.[94,95,97,98]

Statistical analysis of quantified elemental content was carried out by calculating the mean, standard deviation and standard error of the mean for each element separately; then unpaired, two-tailed t-tests on the raw data were carried out assuming a Gaussian distribution and run with 95% confidence interval.

4.4.2.3 X-ray fluorescence imaging of fluorescence-labelled single cells (Advanced Photon Source)

4.4.2.3.1 Sample Preparation

Cells used in XFM imaging were grown, likewise, on 1.5 × 1.5 mm^2 × 500 nm silicon

nitride windows (Silson, UK) in 6-well plates as described previously. [94,97,98] In short, the plates were seeded at 3.2×10^5 cells/well in complete DMEM and were incubated at 310 K in a 5% CO_2-humidified incubator for 24 h prior to treatment. Cells were treated with 100 µM NKP-1339 for 1 h or 4h; or 0.05% DMSO (in media) for 4 h as a vehicle-alone control. At the end of the treatment time the growth media was removed and replaced with fresh growth media containing either 100 nM MitoTracker Deep Red or MitroTracker Orange for 1 hr. Finally, the fluorescence probe solutions were removed and the cells were fixed with 1% paraformaldehyde solution (pH 7.2), before being washed with a 20 mM PIPES/ 200 mM sucrose buffer solution (pH 7.2) thrice.

4.4.2.3.2 Data Collection

4.4.2.3.2.1 Fluorescence-Probe Labelled Imaging

Fluorescence images for 240 x 240 μm^2 areas of the windows were collected using a spectral scanning confocal microscope (Leica TCS SP5) at Adelaide Microscopy. Regions of low cell density were targeted and 4-6 areas were imaged per window. The sample windows were loaded cell-side down onto the microscope stage and an aqueous immersion was used with a 63x water objective. Excitation wavelengths, from an Argon and HeNe laser, of 514 and 633 nm were used for MitoTracker Orange and MitoTracker Deep Red respectively with emission collection ranges of 540-700 and 640-800 nm respectively. Images were collected with a 32 times line average at 1024 x 1024 pixel format with a scanning speed of 400 Hz.

4.4.2.3.2.2 X-ray Fluorescence Imaging

The same methodology as outlines in section 3.4.2.2.2 was employed with the following addition.

The entire window was imaged using an optical microscope (Leica DMRXE), then the areas that were previously imaged using the spectral scanning confocal microscope (Leica TCS SP5) were identified. Despite collecting multiple fluorescence images per window, due to the difficulty of finding these small areas within the larger window, only one area's individual cells were then used for the X-ray fluorescence imaging.

4.4.2.3.3 Data Analysis

4.4.2.3.3.1 X-ray Fluorescence Image Analysis

The same methodology outlined in section 3.4.2.2.3 was employed to analyse this data set.

4.5 Results & Discussion

4.5.1 NKP-1339 Exploratory Study

The preliminary study of the intracellular distribution of ruthenium within A549 cells following NKP-1339 treatment by XFM yielded results consistent with KP1019-like activity. Within the control cells (Figure 4.1) no ruthenium was observed, as expected, as ruthenium is not an endogenous element.

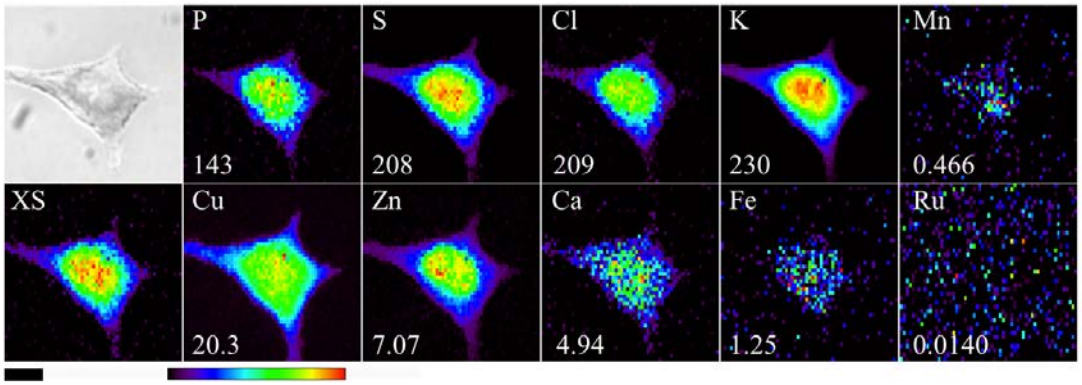

Figure 4.1 – Optical micrographs (top left), scattered X-ray (XS) and XFM elemental distribution maps of a A549 cell treated with 0.05% DMSO as a vehicle-only control. The maximal elemental area density (quantified from standards and expressed in micrograms per square centimetre) is given in the bottom corner of each map. The black bar under the maps represents 10 μm.

Cellular uptake of ruthenium was observed in the cells treated with NKP-1339 (Figure 4.2), regardless of the treatment duration. The ruthenium was observed in localised clusters, in addition to a lower basal intracellular distribution. These ruthenium-rich clusters visually existed alongside a weak co-localisation with a subset of regions of high intracellular copper and iron content (Figure 4.2, red circles).

The secondary co-localisation with iron was not as common as the co-localisations with copper (Figure 4.2, top), and could be observed to be due to a co-localisation between copper and iron instead of a distinct co-localisation between iron and ruthenium. The distribution of ruthenium within the cells was markedly different to that observed of KP1019 within SH-SY5Y cells where the ruthenium was mainly located within the nucleus, along with a lower cytoplasmic concentration.[50]

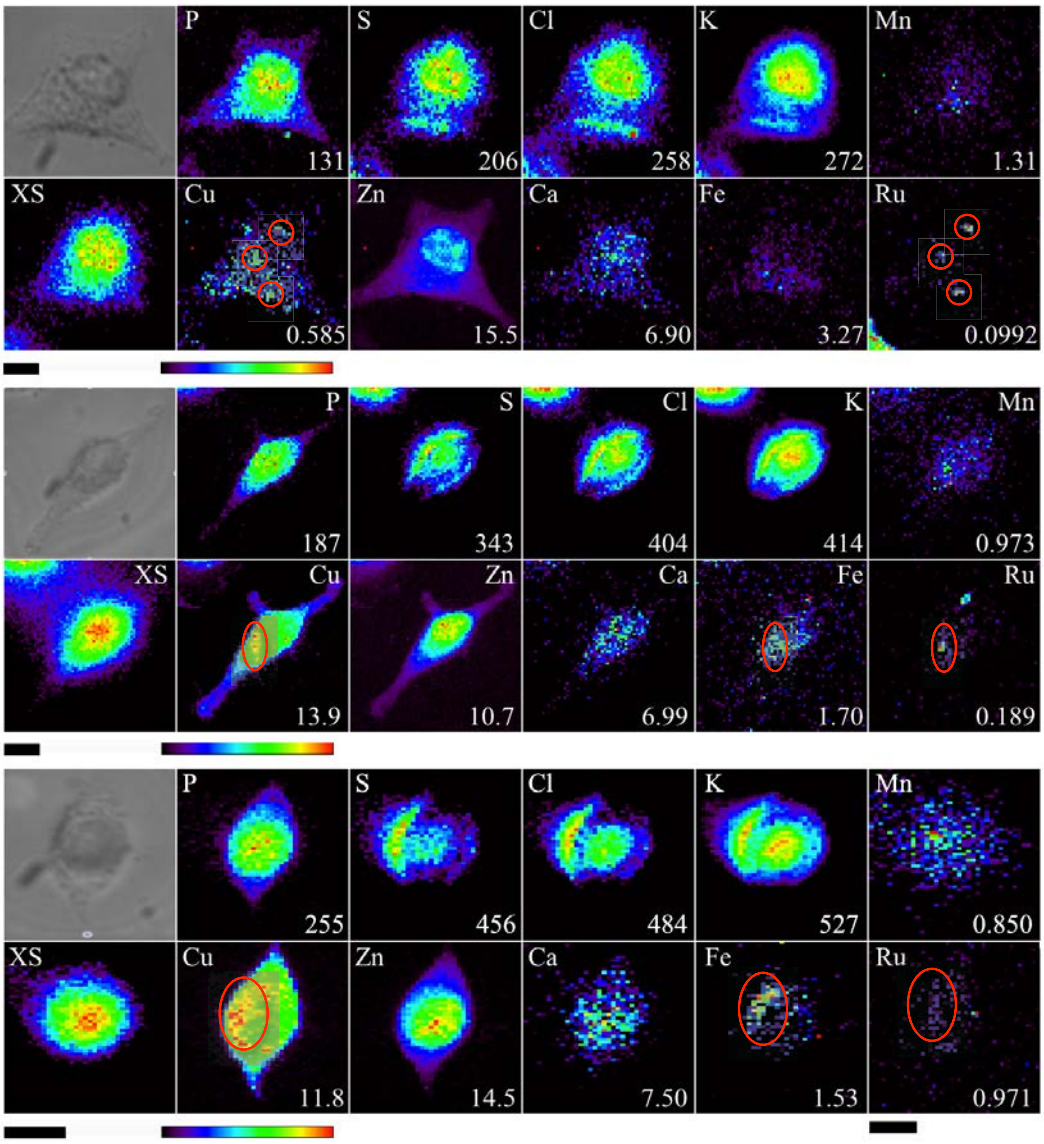

Figure 4.2 – Optical micrographs (top left), scattered X-ray (XS) and XFM elemental distribution maps of A549 cells treated with NKP-1339 for 1 hour (top) or 4 hours (middle, bottom). Possible co-localisations between ruthenium and copper and iron are denoted with a red ring. The maxima elemental area densities (quantified with standards and expressed in micrograms per square centimetre) are given in the bottom corner of each map. The black bar under the maps represents 10 μm.

Given that the two differing excitation energies were required the recording of XFM data for ruthenium and the other biologically relevant elements, accurate co-localisation plots were not possible with this data set as the higher energy maps did not retain sufficient distribution information to correlate with the lower atomic mass elements (Figure 4.3). While some elements, such as zinc and potassium, retained some distribution information in the maps resulting from the higher excitation

energy; others, including chloride and calcium, saw a significant drop in signal. Iron and copper saw the greatest loss in detail at the higher energy with a complete loss of signal into the background noise.

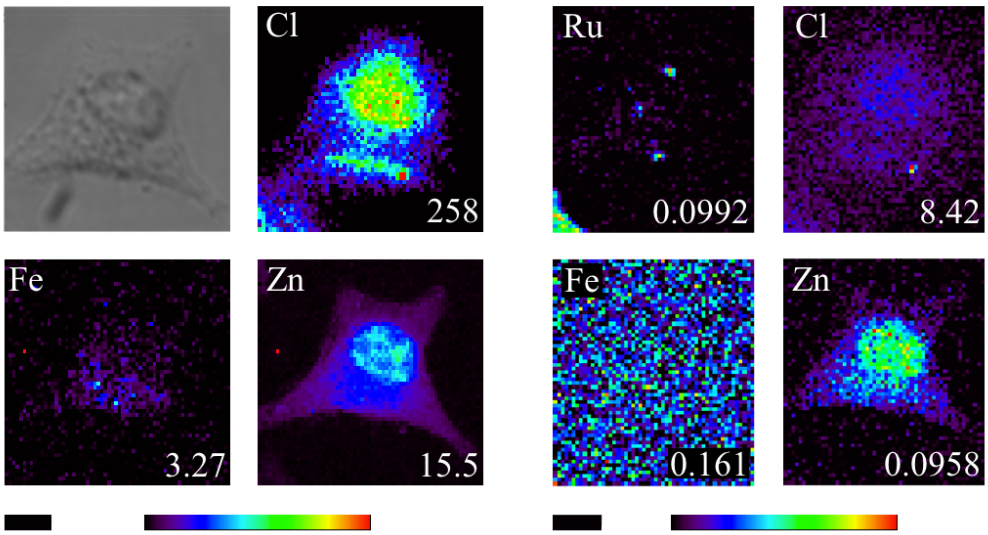

Figure 4.3 – Optical and XFM maps resulting from the lower 10 keV excitation energy (left) and the higher 22 keV excitation energy (right) showcasing a loss in elemental distribution information as the excitation energy was increased. The maxima elemental area densities (quantified from standards and expressed in micrograms per square centimetre) are given in the bottom corner of each map. The black bar under the maps represents 10 µm.

Treatment with the NKP-1339 was observed to significantly perturb homeostasis with differences between control cells and treated cells in most biologically relevant elements (Figure 4.4). However, issues with the washing of the windows caused significant halos in the S, Cl, and K images and so the significance of the differences cannot be solely attributed to the NKP-1339 for these elements.

Despite this, there is still evidence of homeostasis disruption in the results for elements copper, calcium and zinc; all of which should be relatively unaffected by the incomplete washing process due the growth media not containing large amounts of these elements. Copper, interestingly, unlike calcium and zinc levels that were elevated compared to the control cells, instead showed a drastic decrease in content due to NKP-1339 treatment at 1 hour.

This change then reversed such that levels were insignificantly different to the control levels by 4 hours, perhaps indicating the A549 cells have the ability to recover with

time despite the NKP-1339 uptake. This decrease in copper content did not follow that observed for KP1019 in SH-SY5Y cells, where the elemental density of copper increased due to the treatment with the Ru-containing drug.[50] Thereby highlighting a potential difference in intracellular behaviour between NKP-1339 and its close analogue KP1019.

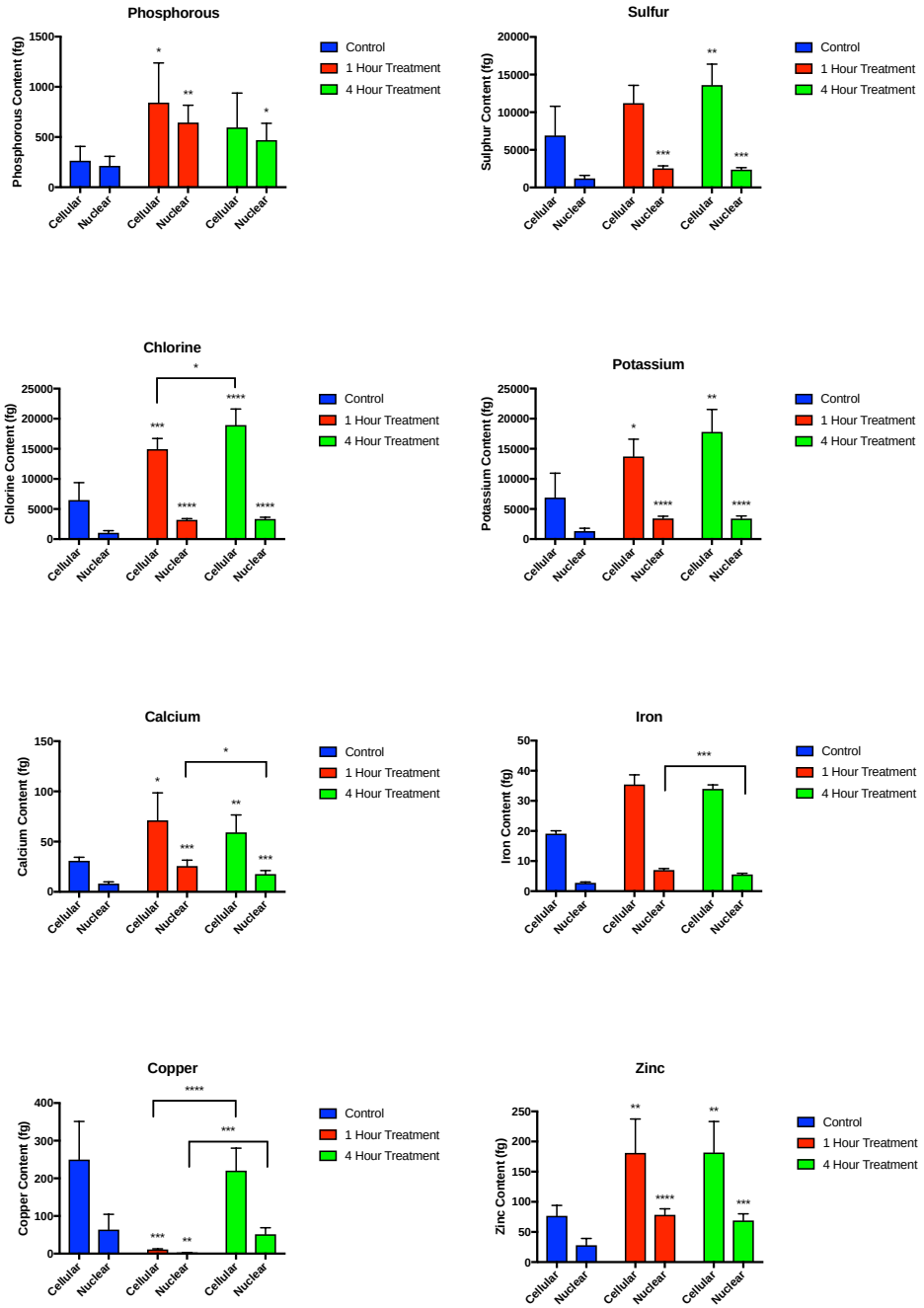

Figure 4.4 – Intracellular content of biologically relevant elements within A549 cells treated with NKP-1339 as quantified by XFM studies for both the cell as a whole and the nuclear sub-fraction. * Represents $p<0.05$, ** $p<0.01$, *** $p<0.001$, **** $p<0.0001$.

The nuclear content for most elements remained largely constant regardless of the treatment conditions (Table 4.1). With only three exceptions (Ca, Zn, Ru), the percentage of each element contained within the nucleus only varied by at most 5% between the control, 1 hour and 4 hour treated cells. Even with the exceptions, the greatest difference was only 9.5% for calcium. Calcium is a key cellular messenger, and so its variation may be due to the mobilisation of calcium ions in response to the introduction of NKP-1339. For both the 1 and 4-hour treated cells showed elevated nuclear content of calcium, possibly indicating apoptosis signalling within the treated cells.

Table 4.1 – Nuclear content of A549 cells treated with NKP-1339, as percentages of the total cellular content for each element. Errors are based on the standard error in the means of the intracellular content data.

Element	Control	1 Hour Treatment	4 Hour Treatment
P	80 ± 35	77 ± 25	79 ± 30
S	18 ± 7	23 ± 3	17 ± 2
Cl	16 ± 6	21 ± 2	18 ± 2
K	19 ± 8	25 ± 4	19 ± 3
Ca	26 ± 4	36 ± 10	30 ± 6
Fe	15 ± 1	20 ± 1	16.36 ± 0.04
Cu	26 ± 12	21 ± 3	23 ± 6
Zn	37 ± 10	43 ± 8	38 ± 7
Ru	22 ± 7	22 ± 5	30 ± 7

Zinc showed an increased nuclear content for the 1-hour time-course, however its increase was only 6.8% over the control. One weakness of the 2D XFM imaging is that cells are inherently 3D structures, and as such there are volumes of cytosol both above and below the nucleus within the cell and these volumes cannot be

differentiated from the true nuclear volume. This significant variation in the zinc fraction may be indicative of this, rather than indicating a mobilisation of zinc into the nucleus of the 1-hour treated cells.

Finally ruthenium showed a gradually increasing nuclear content, and while the aforementioned weakness of XFM imaging for zinc still applies, this may indicate a gradual migration of NKP-1339 or its Ru-containing metabolites into the nucleus. This has marked similarities with the findings of Aitken et. al. with KP1019 in SH-SY5Y cells where they believed KP1019 has a complex uptake system which featured both uptake by transferrin, as well as a passive uptake mechanism.[50] Another study by Pongratz[69] posited that iron needed to be bound to transferrin in addition to the passive uptake mechanism to successfully deliver ruthenium into the nucleus, which could explain the observed delay in nuclear uptake.

It should be noted that while a nuclear fraction for the quantified ruthenium content for the control cells was possible, the corresponding integrated XFM spectra showed no Ru K_α peak despite one being fitted (Figure 4.5). Thus the 1.7 ± 0.3 and 7.6 ± 1.2 fg of nuclear and cellular ruthenium content for the control cells the 21.8% nuclear percentage was based upon should be treated as a measure of the noise rather than an actual ruthenium fluorescence signal for the control cells.

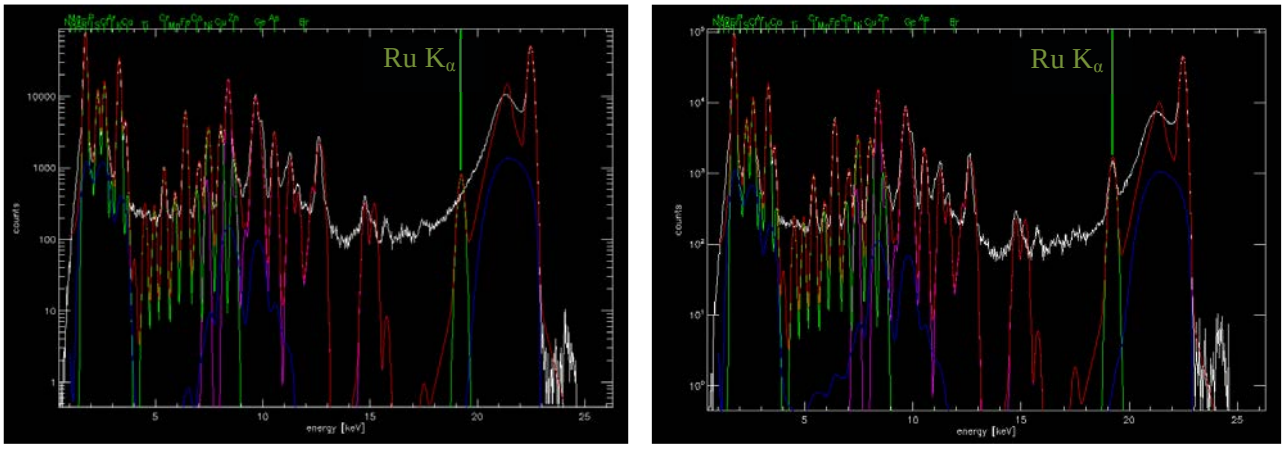

Figure 4.5 – Integrated XFM fitted spectrum for a control A549 cell (left) showing no ruthenium K_α peak within the experimental spectrum (white line) despite one being fit to the data (green peak), in contrast to an integrated XFM spectrum for a 4-hour, NKP-1339 treated A549 cell (right).

The cellular content of ruthenium within the control and treated cells showed a logical progression with ruthenium content increasing with duration of treatment with

NKP-1339 (Figure 4.6). It was observed that while the average ruthenium content, and thus drug uptake, within the cells was higher at 4 hours, there was no significant difference between the 1 and 4 hour time-courses for the cells overall. This is in line with previous work that showed that cellular uptake of NKP-1339 was mostly complete within the first hour after treatment.[80] There was, however, a significant increase in the nuclear ruthenium content between the 1 and 4-hour time-courses; indicating while uptake may have slowed the intracellular ruthenium distribution is still in flux 4 hours after treatment. The 22-30% ruthenium nuclear content was in line with ICP-MS studies of KP1019 that found nuclear contents at a wide range of percentages. The range of ruthenium nuclear contents of 20%[99], 25%[80], and 55%[69] within A2780, KB-3-1 and SW480 cells was ascribed to differences in drug metabolism elicited by the differing cell lines.

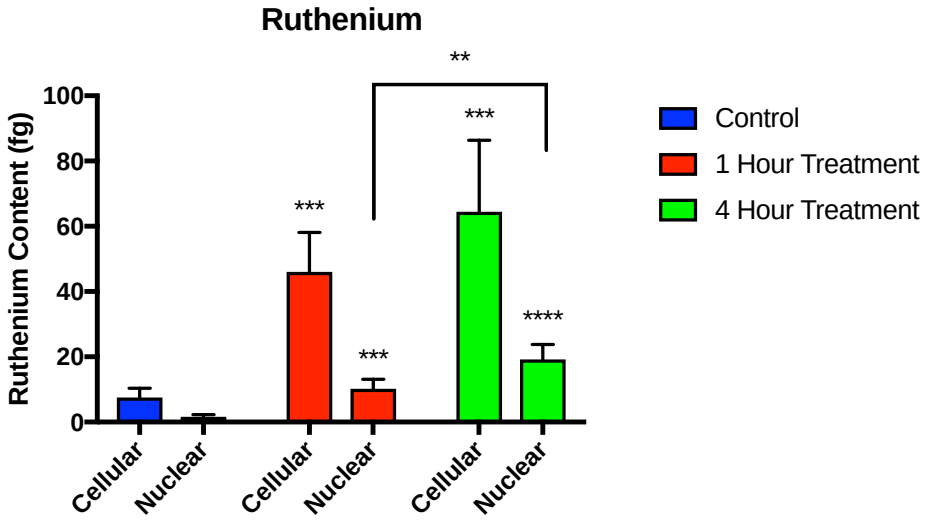

Figure 4.6 – Intracellular content of ruthenium within A549 cells treated with NKP-1339 as quantified by XFM studies for both the cell as a whole and the nuclear sub-fraction. * Represents $p<0.05$, ** $p<0.01$, *** $p<0.001$, **** $p<0.0001$.

Due to the large amounts of time required to image a single cell, sometimes exceeding 1 hour, only limited numbers (4-5 cells) can be imaged for each treatment. In order to verify the overall higher drug uptake at 4 hours a greater number of cells would need to be imaged for each time-course to get a more statistically significant result.

Furthermore, the highly localised distributions of ruthenium could be due to cellular localisation, not within the nucleus, but instead within a cytoplasmic organelle such

as the mitochondria. Such organelles, while not able to be resolved by XFM directly, could be first labelled and imaged with a fluorescent probe prior to XFM imaging. By collating the XFM and fluorescence data the cellular localisations of NKP-1339 or its metabolites could be further explored.

4.5.2 NKP-1339 Experiments with Organelle Staining

Follow up experiments aimed to investigate the intracellular distribution of ruthenium within A549 cells following NKP-1339 treatment with additional mitochondrial staining. Within the control cells (Figure 4.7) once again no ruthenium was observed.

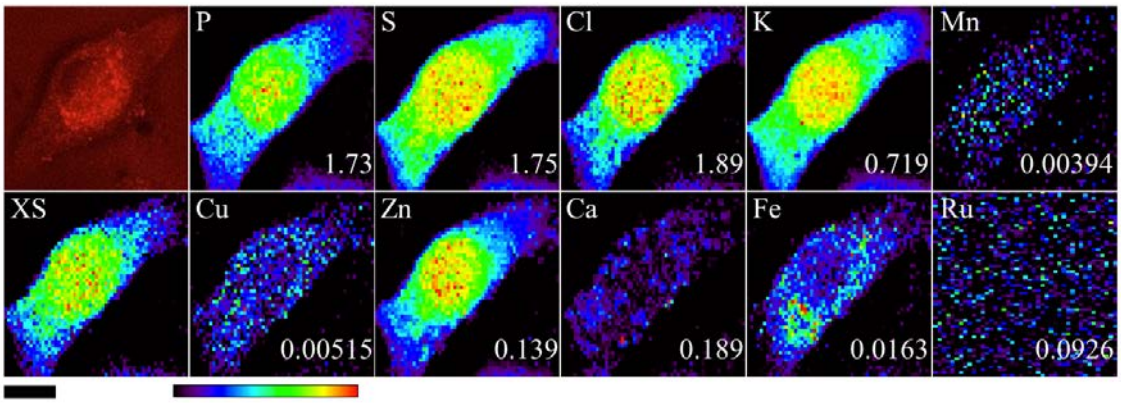

Figure 4.7 – Optical fluorescence image (top left), scattered X-ray (XS) and XFM elemental distribution maps of an A549 control cell (treated with 0.05% DMSO as a vehicle-only control) that had mitochondrial staining with MitoTracker DeepRed. The maximal elemental area densities (quantified from standards and expressed in micrograms per square centimetre) are given in the bottom corner of each map. The scale bar represents 10 μm.

Two different stains were used MitoTracker DeepRed and MitoTracker Orange, however the controls for MitoTracker Orange (i.e. treated with the fluorophore but not NKP-1339) were damaged in transit to the synchrotron and so could not be imaged. To prevent the halos observed in the preliminary study the windows were not just immersed in the PIPES/sucrose buffer solutions, instead they were gently oscillated within the buffer solution to ensure more complete washing.

Within this study a strong co-localisation was observed between intracellular ruthenium and iron throughout all NKP-1339 treated cells (Figure 4.8, 4.9). This co-localisation was much more apparent as there appeared to be greater cellular uptake of the ruthenium during this study compared to the preliminary study. With the ruthenium content after 1 and 4-hour treatments with NKP-1339 being 194 ± 30 and

486 ± 70 fg compared to the 46 ± 5 and 64 ± 8 fg respectively of the preliminary study.

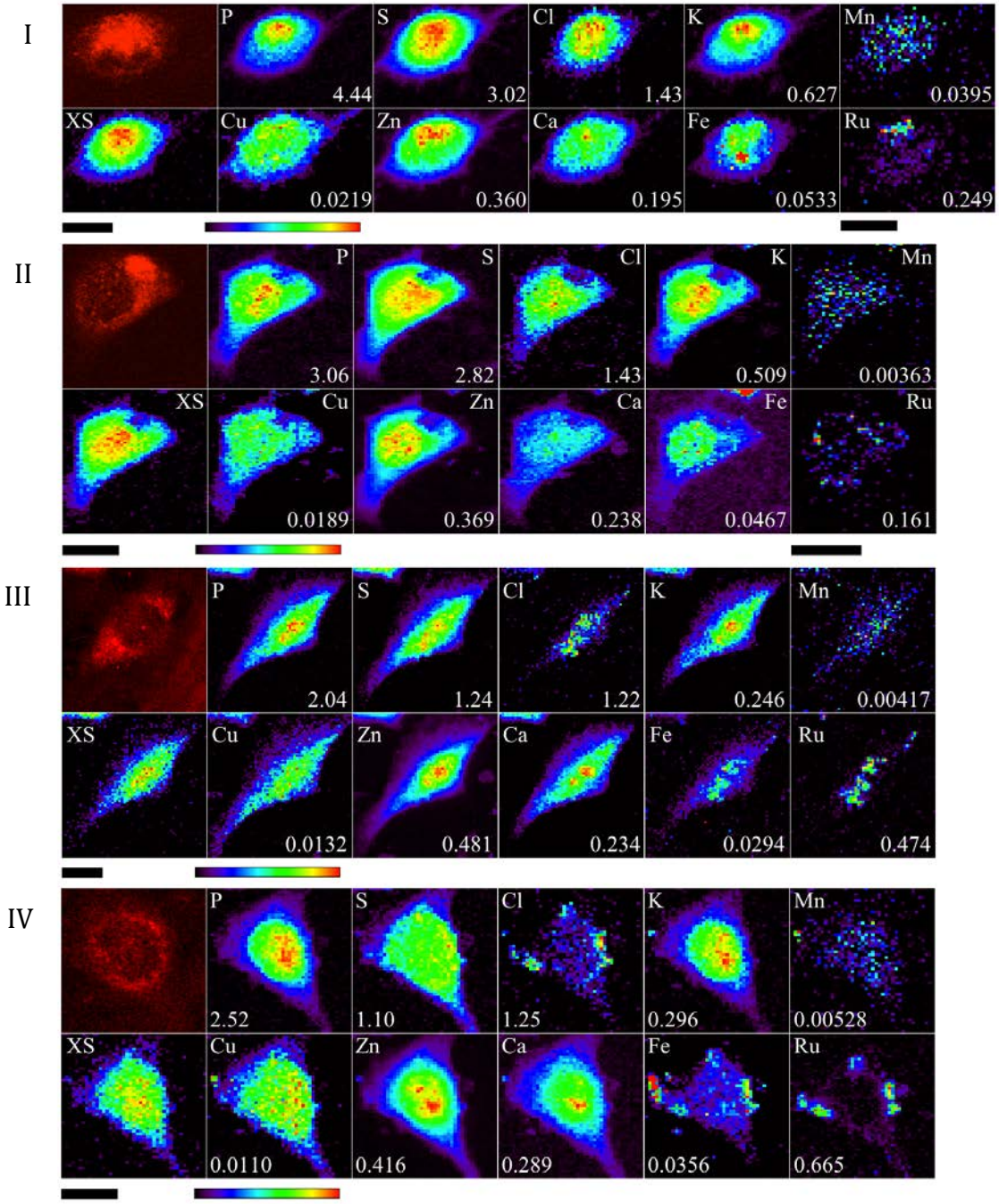

Figure 4.8 – Optical fluorescence images (top left), scattered X-ray (XS) and XFM elemental distribution maps of A549 cells treated with NKP-1339 for 1 hour (I, II) or 4 hours (III, IV), after mitochondrial staining with MitoTracker DeepRed. The maxima elemental area densities (quantified from standards and expressed in micrograms per square centimetre) are given in the bottom corner of each map. The black bar under the maps represents 10 μm.

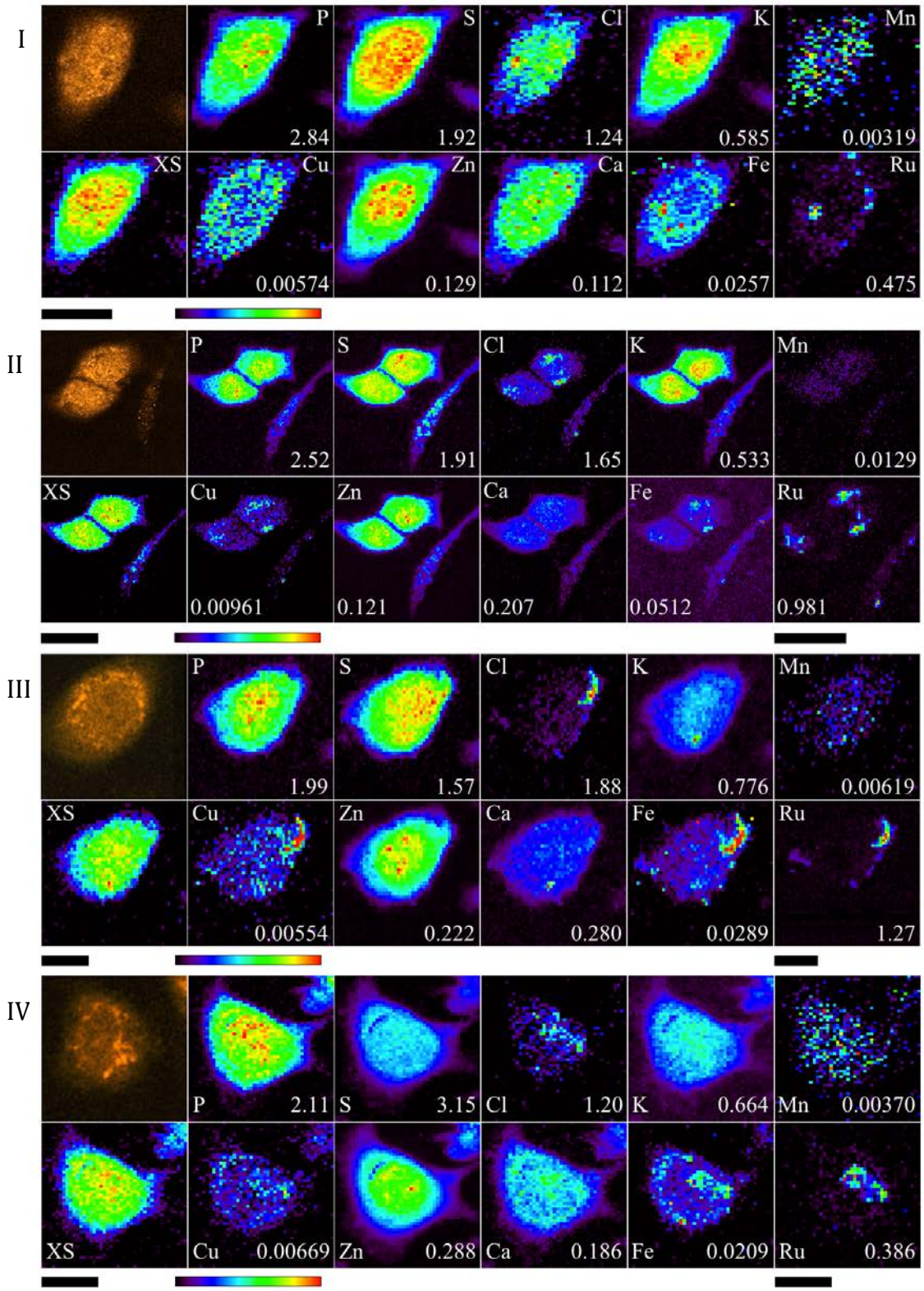

Figure 4.9 – Optical fluorescence images (top left), scattered X-ray (XS) and XFM elemental distribution maps of A549 cells treated with NKP-1339 for 1 hour (I, II) or 4 hours (III, IV), after mitochondrial staining with MitoTracker Orange. The maxima elemental area densities (quantified from standards and expressed in micrograms per square centimetre) are given in the bottom corner of each map. The black bar under the maps represents 10 μm.

A co-localisation with copper was once again observed as in the preliminary study, present in the images for the cells stained with MitoTracker Orange (Figure 4.8 – II, III, IV), while not as readily apparent in those stained with MitoTracker DeepRed. In addition, unlike with the preliminary study where the elemental halos made the chlorine images less useful, there was both a visual co-localisation between ruthenium and chlorine (Figure 4.10), and a quantitative co-localisation observed (Figure 4.11).

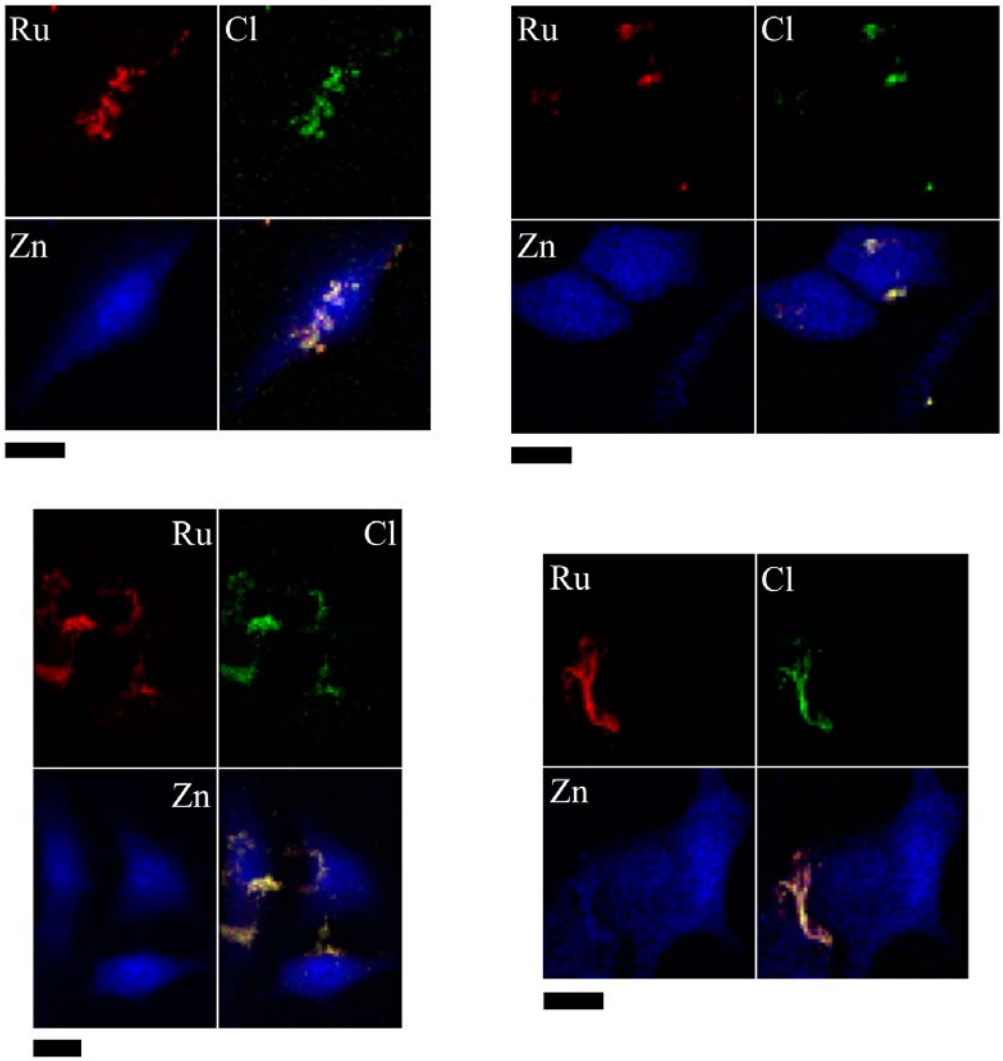

Figure 4.10 – Co-localisation plots (bottom right) between ruthenium (red) and chlorine (green), displayed along with zinc (blue) which was used to show the general cell shape for: (I), (II) A549 cells treated with NKP-1339 for 4 hours after mitochondrial staining with MitoTracker DeepRed; (III), (IV) A549 cells treated with NKP-1339 for 1 hour after mitochondrial staining with MitoTracker Orange. The black bar under the maps represents 10 μm.

The co-localisations (Figure 4.10) were clearly visible, and a strong positive correlation between the concentrations of ruthenium and chlorine for each pixel of the elemental maps (Figure 4.11), in combination these showcase the strong co-localisation between the two elements.

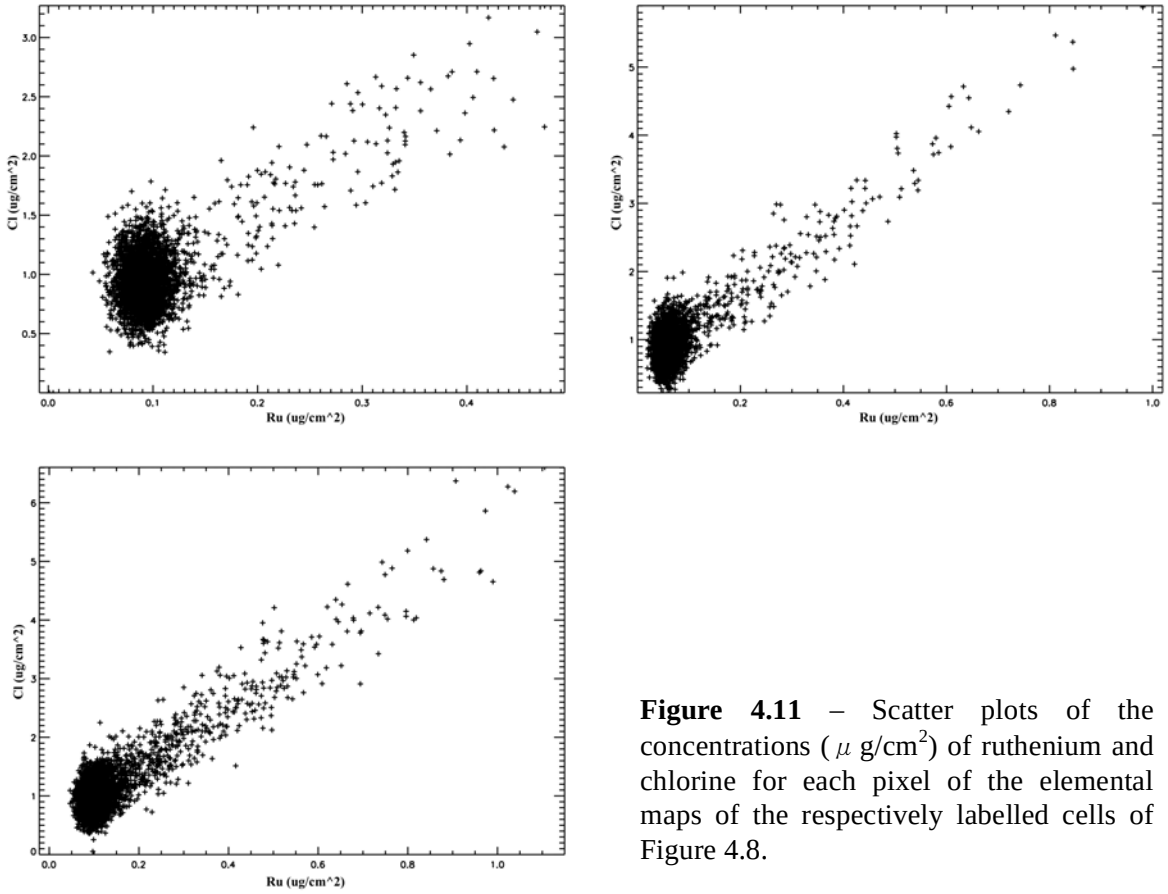

Figure 4.11 – Scatter plots of the concentrations (μ g/cm^2) of ruthenium and chlorine for each pixel of the elemental maps of the respectively labelled cells of Figure 4.8.

These comparison plots were possible as the elemental distribution information from the lower excitation energy maps was preserved in the higher excitation energy XFM maps (Figure 4.12). This allowed for the higher energy maps for Cl, Fe, Zn and Ru to be utilised for co-localisation plots without concerns for the differing scaling and alignment issues from the preliminary study.

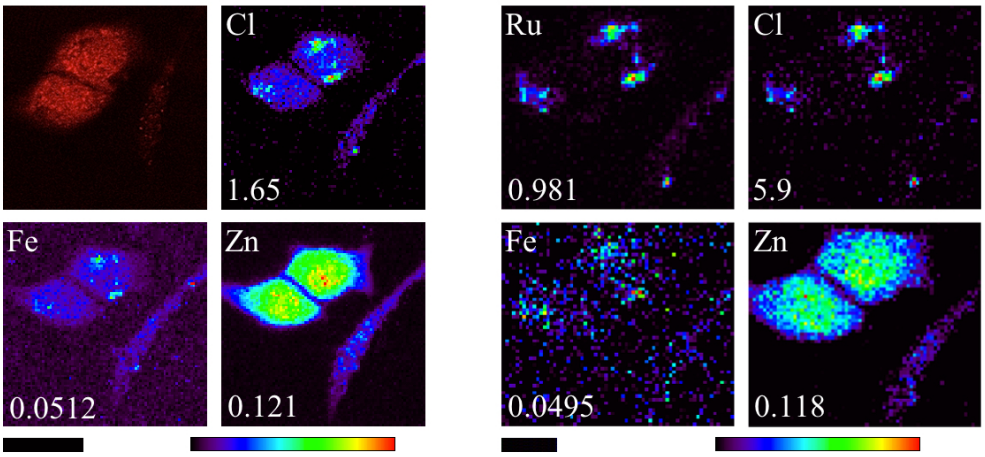

Figure 4.12 – Optical fluorescence and XFM maps resulting from the lower 10 keV excitation energy (left) and the higher 22 keV excitation energy (right) showcasing a greater preservation in elemental distribution information as the excitation energy was increased. The maxima elemental area densities (quantified from standards and expressed in micrograms per square centimetre) are given in the bottom corner of each map. The black bar under the maps represents 10 µm.

Chlorido ligands exist within the structure of NKP-1339, and thus this co-localisation would suggest that the aquation and hydrolysis steps common to both NAMI-A and KP1019 are resisted to some extent by NKP-1339. This could help to prevent side effects, as it would mean the compound is more likely to reach the target sites intact.

Unlike in the preliminary study, this study showed a strong co-localisation with iron in all 4-hour treatment images. This was independent of the mitochondrial stain employed, and resulted in a strong co-localisation between iron and chlorine (Figure 4.13).

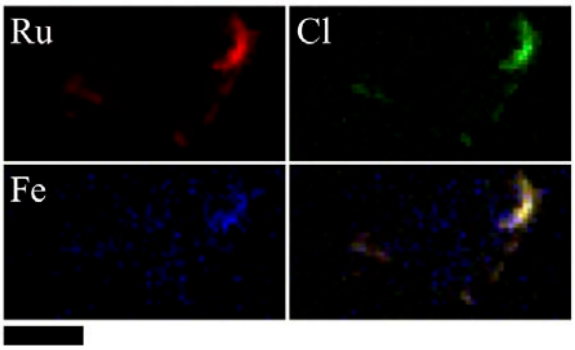

Figure 4.13 – Co-localisations plots (bottom right) between ruthenium (red), chloride (green), and iron (blue) for an A549 cell treated with NKP-1339 for 4 hours (III, IV), after mitochondrial staining with MitoTracker Orange. The black bar under the maps represents 10 µm.

While it was sometimes present (Figure 4.9, II), the majority of 1-hour treated cells did not show a strong co-localisation with iron. The iron-ruthenium co-localisations largely mirrored those found for KP1019 treated SH-SY5Y cells[50], where the regions were proximal to the nuclear envelope (Figure 4.8, IV; Figure 4.9, II, III).

In terms of the mode of action, it is known that cellular gallium uptake due to transferrin binding into endosomes perturbs intracellular iron distribution and ultimately causes the starvation of intracellular, free iron.[40] This could mean that the co-localisation of ruthenium and iron observed for NKP-1339 treated cells within this study could point to an anticancer activity based on interactions with iron. Whether NKP-1339 sequesters iron within the iron uptake endosomes like gallium, or simply binds intracellular, free iron, or is involved in Fenton chemistry, is not possible to ascertain with this data.

As seen in the preliminary study the ruthenium distribution does not follow the cell thickness, instead it has a distinct, punctate distribution above a lower cytosol distribution. Generally the distribution showed nuclear envelope exclusion for the ruthenium, suggesting that DNA is not the primary target of NKP-1339. Occasionally there were highly localised areas of ruthenium that appeared to overlap with the nuclear envelope (Figure 4.8, III), making it uncertain if the clusters are inside the cell cytosol region above and below the nucleus, or on the outside of the cells mimicking NAMI-A activity. Given there are no clear extracellular clusters of ruthenium observed (on cell edges), it is more likely the clumps observed are in the cytosol above and below the nucleus. This is further strengthened by the co-localisation with iron, an intracellular element.

The results of the mitochondrial staining were largely inconclusive. While some cells seemed to show a visual co-localisation of the probe fluorescence and the ruthenium distribution (Figure 4.8 I, Figure 4.9 IV), it was not consistent throughout all the images. A549 cells did not have a high contrast between the fluorescence of the mitochondria in the cytosol and the nuclear envelope, instead having generally high fluorescence throughout the cell. Nor did many of the cells display strongly asymmetrical or suitably irregular mitochondrial distributions (Figure 4.9 I, III), once again making judgements of mitochondrial uptake of NKP-1339 difficult to ascertain. Furthermore, if only a subset of mitochondria take up and are affected by NKP-1339 administration, this would be very difficult to visualise.

Attempts to utilise inductively coupled plasma mass spectrometry (ICP-MS) on cytosolic and mitochondrial lysates to determine if there was NKP-1339 uptake were ultimately also inconclusive due to ICP-MS sensitivity, and a lack of access to adequate amounts of the drug to treat the large volumes of cells needed to produce viable volumes of mitochondrial lysates to subsequently analyse.

The perturbations in biological elemental content were quantified (Figure 4.14).

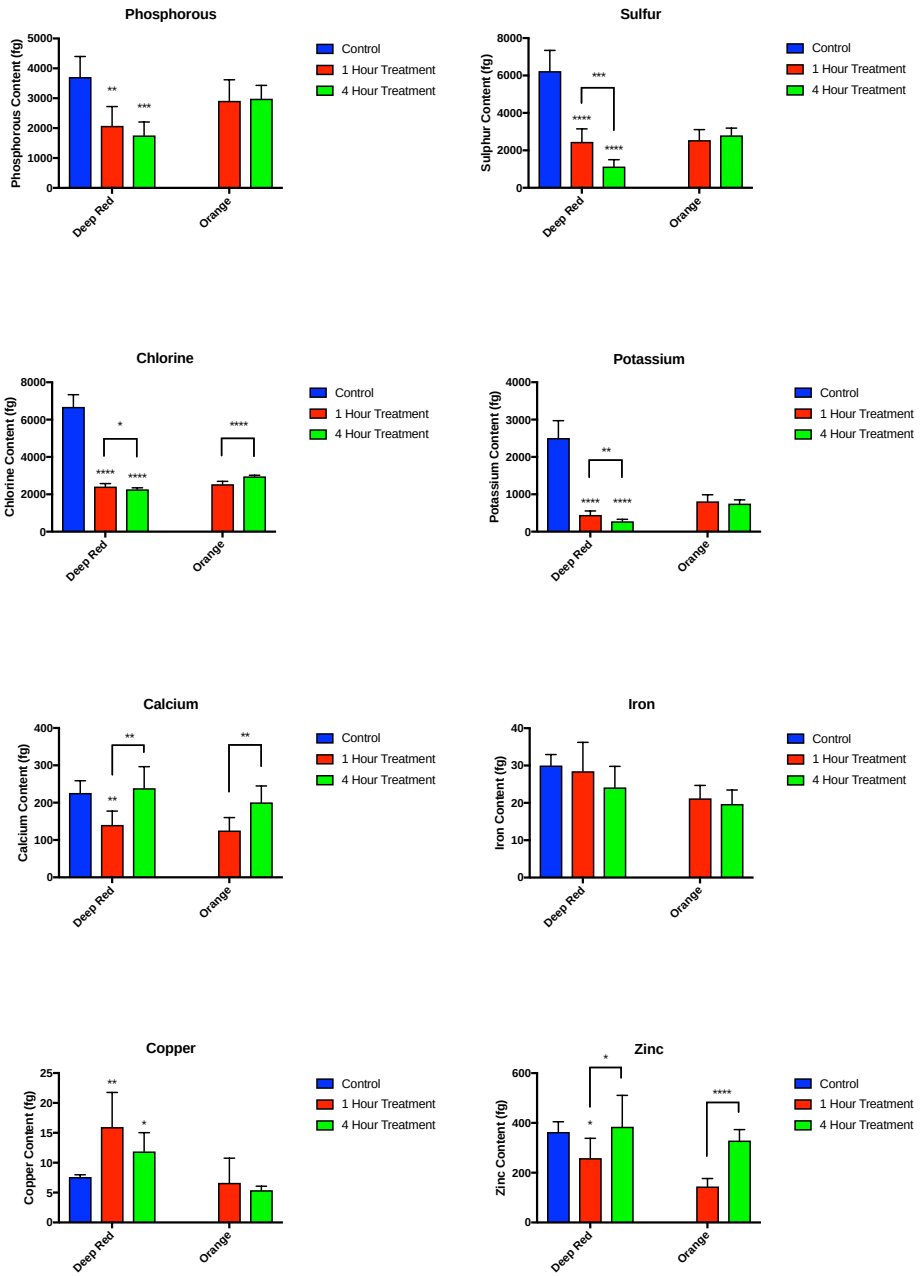

Figure 4.14 – Intracellular content of biologically relevant elements within A549 cells treated with NKP-1339, after mitochondrial staining with MitoTracker DeepRed or MitoTracker Orange, as quantified by XFM studies. * Represents $p<0.05$, ** $p<0.01$, *** $p<0.001$, **** $p<0.0001$.

The addition of the mitochondrial probe to the experimental conditions was observed to elicit different perturbations (Figure 4.14) to the biological elements than just administration of NKP-1339 as in the preliminary study (Figure 4.4).

In the preliminary study most biological elements had their intracellular levels increased, with the exception of copper levels. However, with the introduction of the mitochondrial probe, there was instead an observed suppression to the biological elements P, S, Cl, and K. This may have been due to not only the addition of the mitochondrial probe, but also the modified washing techniques that resulted in the removal of the contributions of the S, Cl and K halos that were observed in the preliminary study.

Intracellular calcium levels were supressed at the 1-hour time-course, but had recovered by the 4-hour mark, a trend that was mirrored by intracellular zinc levels. Iron, in this follow up study showed no marked changes due to NKP-1339 treatments. Finally, in this follow up study copper levels were all elevated due to NKP-1339 treatment compared to the MitoTracker DeepRed controls.

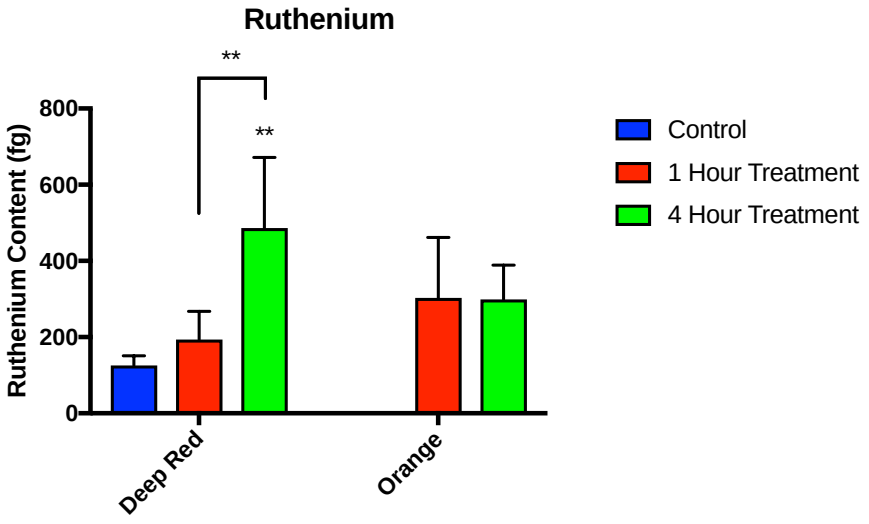

Figure 4.15 – Intracellular content of ruthenium within A549 cells treated with NKP-1339, after mitochondrial staining agent MitoTracker DeepRed or MitoTracker Orange, as quantified by XFM studies. * Represents $p<0.05$, ** $p<0.01$, *** $p<0.001$.

Unlike in the preliminary study, the quantified ruthenium content provided a range of findings (Figure 4.15). Firstly, while no control cells stained with MitoTracker Orange cells were available, there was no significant difference in ruthenium content

between the 1 and 4-hour NKP-1339 treatment time-courses. However there was a significant difference between the two time-courses for the MitoTracker DeepRed stained cells. Thus, no definitive determination as to whether uptake has been completed after 1-hour, which was not conclusive from the preliminary study, can be made due to the conflicting nature of the results between the two stains.

Furthermore, despite the elemental maps for the control cells showing no discernable ruthenium content, the quantified data produced a significant greater content for the MitoTracker DeepRed stained control cells than from the preliminary study (7.6 ± 1.2 fg). It was determined during the fitting that the data set had a higher inelastic scatter peak than the data for the preliminary study, which meant that significant ruthenium content was fit. This was an irrevocable difference between the two studies, preventing any direct comparisons of quantified content levels, instead limiting the findings to dealing with comparisons of observed trends within the studies individually.

In a repeat of the preliminary study, contrary to the integrated XFM spectra showing no ruthenium K_α peak like the treated cells, a significant amount was quantified (130 ± 30 fg) for the control cells (Figure 4.16). Once again the content quantified for the control cell can thus be treated as a measure of noise within the ruthenium fitting.

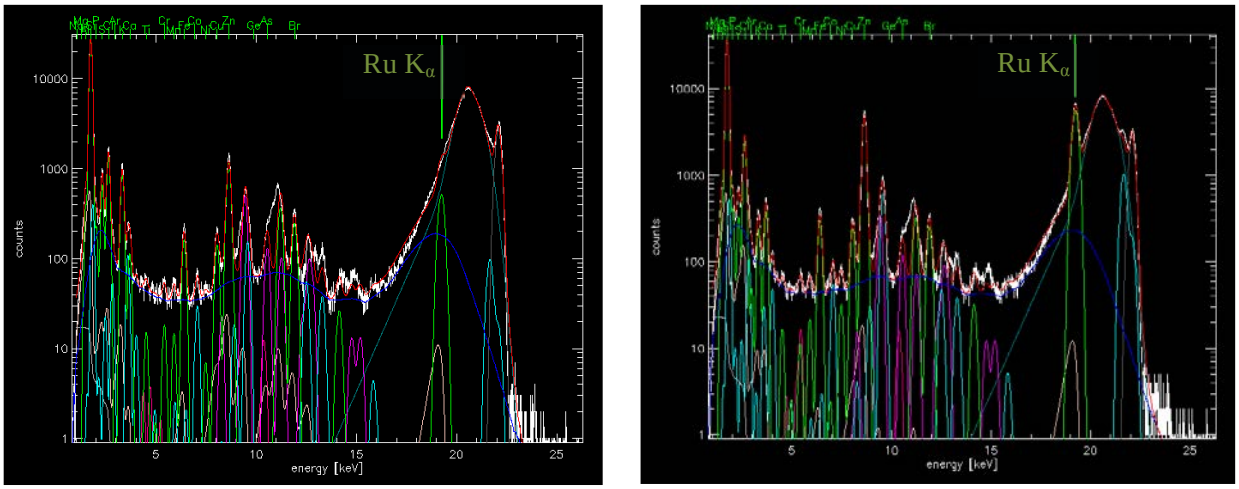

Figure 4.16 – Integrated XFM fitted spectrum for a MitoTracker tagged control A549 cell (left) showing no ruthenium K_α peak within the experimental spectrum (white line) despite one being fit to the data (green peak), in contrast to an integrated XFM spectrum for a MitoTracker tagged 4-hour, NKP-1339 treated A549 cell (right).

Ultimately, should more NKP-1339 become available to complete further studies, the

results show that particular attention needs to be paid towards the choice of mitochondrial stain. Each stain appears to have perturbed the sulfur and potassium homeostasis of A549 cells differently (Figure 4.14), and this would need to be factored into any further research involving these stains both separately and together. Had the MitoTracker Orange control cells not been damaged in transit and thus analysed, a more direct comparison would be possible and the different effects on the homeostasis of each element could be observed without the additional influence of the NKP-1339.

4.6 - Conclusions and Future Directions

Future study is required to gain greater insight into the mechanism of action of the ruthenium-based anticancer agent NKP-1339. These preliminary studies show that the drug is internalised by cancer cells, in a similar fashion to its parent compound KP1019. Unlike studies into its parent compound[50], there is no nuclear localisation of the drug, however, pointing to DNA not being its primary target. Instead it appears to collect within the cytosol in highly localised distributions, as well as a much lower cytosol-wide distribution.

Despite this difference, analogous co-localisations between iron and ruthenium proximal to the nuclear envelope were observed. This was not unprecedented given current consensus regarding the role of transferrin with ruthenium transport. It is possible that the perturbation of iron homeostasis within NKP-1339 treated cells contributes to its anticancer activity.

To gain a better understanding of the nature of its co-localisation with iron, a pH-sensitive endosome fluorescence probe could be used instead of MitoTrackers. This would provide an indication of whether the ruthenium is being taken in, but being trapped with iron, within the endosomes, thereby starving the cell of iron.

While versatile, A549 cells did not result in a suitably asymmetrical or irregular mitochondrial distribution to investigate mitochondrial uptake. Instead a range of other cell lines, preferably with larger nuclear envelopes or more irregular cellular morphologies, should be trialled to find a cell line with a reliably unique mitochondrial distribution. This would allow for the same experiment to be run yielding more informative results. Furthermore, if more NKP-1339 could be attained in large enough volumes, then ICP-MS could be once again trialled on cellular lysates. This would aid in determining if there is any mitochondrial uptake of NKP-1339.

XFM is most commonly used in conjunction with XANES analysis, which provides information about speciation, rather than spatial distribution. This would be important in ascertaining the oxidation state and localised environment of the ruthenium within the cells, and would help confirm NKP-1339's apparent resistance to ligand exchange. It has been previously utilised to observe ruthenium moieties that result from the pro-drug treatment of NAMI-A and KP1019 in cells and solution.[7,8,39,57]

4.7 Acknowledgments

Access to both the A549 cells as well as cell-culture laboratory, pivotal to the experiments, were provided by Ian Musgrave (The University of Adelaide).

Synchrotron-based portions of this research were carried out at the Advanced Photon Source (APS), a part of the Argonne National Labs, a U.S. Department of Energy (DOE) Office of Science User Facility operated for the DOE Office of Science by Argonne National Laboratory under Contract No. DE-AC02-06CH11357. Furthermore, beam-line scientists Barry Lai[#] and Stefan Vogt[#] were instrumental with the collection of the XFM data as well as providing assistance with subsequent data processing.

[#]Advanced Photon Source, X-ray Science Division, Argonne National Laboratory, Argonne, IL 60439, USA

4.8 References

(1) Rademaker-Lakhai, J. M. *Clin. Cancer Res.* **2004**, *10* (11), 3717.

(2) Leijen, S.; Burgers, S. A.; Baas, P.; Pluim, D.; Tibben, M.; van Werkhoven, E.; Alessio, E.; Sava, G.; Beijnen, J. H.; Schellens, J. H. M. *Invest. New Drugs* **2015**, *33* (1), 201.

(3) Alessio, E. *Eur. J. Inorg. Chem.* **2017**, *12*, 1549.

(4) Hartinger, C.; Zorbas-Seifried, S.; Jakupec, M.; Kynast, B.; Zorbas, H.; Keppler, Bernhard K. *J. Inorg. Biochem.* **2006**, *100*, 891.

(5) Jakupec, M. A.; Arion, V. B.; Kapitza, S.; Reisner, E.; Eichinger, A.; Pongratz, M.; Marian, B.; Graf von Keyserlingk, N.; Keppler, B. K. *Int. J. Clin. Pharmacol. Ther.* **2005**, *43* (12), 595.

(6) Han Ang, W.; Dyson, P. J. *Eur. J. Inorg. Chem.* **2006**, *2006* (20), 4003.

(7) Levina, A.; Aitken, J. B.; Gwee, Y. Y.; Lim, Z. J.; Liu, M.; Singharay, A. M.; Wong, P. F.; Lay, P. A. *Eur. Chem. J.* **2013**, *19* (11), 3609.

(8) Levina, A.; Mitra, A.; Lay, P. A. *Metallomics* **2009**, *1* (6), 458.

(9) Rosenberg, B.; VanCamp, L.; Trosko, J. E.; Mansour, V. H. *Nature* **1969**, *222* (5191), 385.

(10) Reisner, E.; Arion, V. B.; Keppler, B. K.; Pombeiro, A. *Inorg. Chim. Acta* **2008**, 1569.

(11) Dwyer, F. P.; Gyarfas, E. C.; Rogers, W. P.; Koch, J. H. *Nature* **1952**, *170*, 190.

(12) Dwyer, F. P.; Mayhew, E.; Roe, E. M. F.; Shulman, A. *Br. J. Cancer* **1965**, *19* (1), 195.

(13) Meggers, E. *Curr. Opin. Chem. Biol.* **2007**, *11* (3), 287.

(14) Boulikas, T.; Vougiouka, M. *Oncol. Rep.* **2003**, *10* (6), 1663.

(15) Pasini, A.; Zunino, F. *Angew. Chem. Int. Ed. Eng.* **1987**, *26* (7), 615.

(16) Alderden, R. A.; Hall, M. D.; Hambley, T. W. *J. Chem. Ed.* **2006**, *83* (5), 728.

(17) Reedijk, B. J. *Platin. Met. Rev.* **2008**, *52* (1), 2.

(18) Reedijk, J. *Eur. J. Inorg. Chem.* **2009**, *10*, 1303.

(19) Reedijk, J. *Macromol. Symp.* **2008**, *270* (1), 193.

(20) Morris, T. T.; Ruan, Y.; Lewis, V. A.; Narendran, A.; Gailer, J. *Metallomics* **2014**, *6*, 2034.

(21) Peacock, A. F. A.; Sadler, P. J. *Chem. Asian J.* **2008**, *3* (11), 1890.
(22) Wong, E.; Giandomenico, C. M. *Chem. Rev.* **1999**, *99* (9), 2451.
(23) Galanski, M.; Jakupec, M. A.; Keppler, B. K. *Curr. Med. Chem.* **2005**, *12* (18), 2075.
(24) Fricker, S. P. *Dalton Trans.* **2007**, *43*, 4903.
(25) Kay, P. *Semin. Oncol. Nurs.* **2006**, *22* (1 Suppl 1), 1.
(26) Jakupec, M. A.; Galanski, M.; Arion, V. B.; Hartinger, C. G.; Keppler, B. K. *Dalton Trans.* **2008**, *2*, 183.
(27) Vouillamoz-Lorenz, S.; Buclin, T.; Lejeune, F.; Bauer, J.; Leyvraz, S.; Decosterd, L. A. *Anticancer Res.* **2003**, *23* (3C), 2757.
(28) Clarke, M. J.; Zhu, F.; Frasca, D. R. *Chem. Rev.* **1999**, *99* (9), 2511.
(29) Zhang, C. X.; Lippard, S. J. *Curr. Opin. Chem. Biol.* **2003**, *7* (4), 481.
(30) Galanski, M.; Arion, V. B.; Jakupec, M. A.; Keppler, B. K. *Curr. Pharm. Des.* **2003**, *9* (25), 2078.
(31) Wang, D.; Lippard, S. J. *Nat. Rev. Drug Discov.* **2005**, *4* (4), 307.
(32) Hall, M. D.; Mellor, H. R.; Callaghan, R.; Hambley, T. W. *J. Med. Chem.* **2007**, *50* (15), 3403.
(33) Clarke, M. J. *Coord. Chem. Rev.* **2003**, *236*, 209.
(34) Allardyce, C. S.; Dorcier, A.; Scolaro, C.; Dyson, P. J. *Appl. Organomet. Chem.* **2005**, *19* (1), 1.
(35) Bruijnincx, P. C. A.; Sadler, P. J. *Curr. Opin. Chem. Biol.* **2008**, *12* (2), 197.
(36) Gianferrara, T.; Bratsos, I.; Iengo, E.; Milani, B.; Ostrić, A.; Spagnul, C.; Zangrando, E.; Alessio, E. *Dalton Trans.* **2009**, *48*, 10742.
(37) Pessoa, J. C.; Tomaz, I. *Curr. Med. Chem.* **2010**, *17* (31), 3701.
(38) Ang, W. H.; Casini, A.; Sava, G.; Dyson, P. J. *J. Organomet. Chem.* **2011**, *696*, 989.
(39) Gransbury, G. K.; Kappen, P.; Glover, C. J.; Hughes, J. N.; Levina, A.; Lay, P. A.; Musgrave, I. F.; Harris, H. H. *Metallomics* **2016**, *8* (8), 762.
(40) Alessio, E.; Mestroni, G.; Bergamo, A.; Sava, G. *Curr. Top. Med. Chem.* **2004**, *4* (15), 1525.
(41) Sava, G.; Pacor, S.; Mestroni, G.; Alessio, E. *Clin. Exp. Metastasis* **1992**, *10* (4), 273.
(42) Sava, G.; Zorzet, S.; Turrin, C.; Vita, F.; Soranzo, M.; Zabucchi, G.; Cocchietto, M.; Bergamo, A.; DiGiovine, S.; Pezzoni, G.; Sartor, L.; Garbisa,

S. *Clin. Cancer Res.* **2003**, *9* (5), 1898.

(43) Sava, G.; Clerici, K.; Capozzi, I.; Cocchietto, M.; Gagliardi, R.; Alessio, E.; Mestroni, G.; Perbellini, A. *Anticancer Drugs* **1999**, *10* (1), 129.

(44) Bratsos, I.; Jedner, S.; Gianferrara, T.; Alessio, E. *Chimia* **2007**, *61* (11), 692.

(45) Bergamo, A.; Sava, G. *Dalton Trans.* **2007**, No. 13, 1267.

(46) Sava, G.; Capozzi, I.; Clerici, K.; Gagliardi, G.; Alessio, E.; Mestroni, G. *Clin. Exp. Metastasis* **1998**, *16* (4), 371.

(47) Cocchietto, M.; Zorzet, S.; Sorc, A.; Sava, G. *Invest. New Drugs* **2003**, *21* (1), 55.

(48) Bacac, M.; Hotze, A. C. G.; van der Schilden, K.; Haasnoot, J. G.; Pacor, S.; Alessio, E.; Sava, G.; Reedijk, J. *J. Inorg. Biochem.* **2004**, *98* (2), 402.

(49) Bergamo, A.; Sava, G. *Chem. Soc. Rev.* **2015**, *44* (24), 8818.

(50) Aitken, J. B.; Antony, S.; Weekley, C. M.; Lai, B.; Spiccia, L.; Harris, H. H. *Metallomics* **2012**, *4* (10), 1051.

(51) Gava, B.; Zorzet, S.; Spessotto, P.; Cocchietto, M.; Sava, G. *J. Pharmacol. Exp. Ther.* **2006**, *317* (1), 284.

(52) Sava, G.; Frausin, F.; Cocchietto, M.; Vita, F.; Podda, E. *European Journal of Cancer* **2004**, *40*, 1383.

(53) Casarsa, C.; Mischis, M. T.; Sava, G. *J. Inorg. Biochem.* **2004**.

(54) Webb, M. I.; Walsby, C. J. *Dalton Trans.* **2011**, *40* (6), 1322.

(55) Cetinbas, N.; Webb, M. I.; Dubland, J. A.; Walsby, C. J. *J. Bio. Inorg. Chem.* **2010**, *15* (2), 131.

(56) Levina, A.; Lay, P. A. *Inorg. Chem. Front.* **2014**.

(57) Liu, M.; Lim, Z. J.; Gwee, Y. Y.; Levina, A.; Lay, P. A. *Angew. Chem. Int. Ed.* **2010**, *49* (9), 1661.

(58) Hartinger, C. G.; Jakupec, M. A.; Zorbas Seifried, S.; Groessl, M.; Egger, A.; Berger, W.; Zorbas, H.; Dyson, P. J.; Keppler, B. K. *Chem. Biodivers.* **2008**, *5* (10), 2140.

(59) Morbidelli, L.; Donnini, S.; Filippi, S.; Messori, L.; Piccioli, F.; Orioli, P.; Sava, G.; Ziche, M. *Br. J. Cancer* **2003**, *88* (9), 1484.

(60) Lipponer, K. G.; Vogel, E.; Keppler, B. K. *Met.-Based Drugs* **1996**, *3* (5), 243.

(61) Berger, M. R.; Garzon, F. T.; Keppler, B. K.; Schmähl, D. *Anticancer Res.* **1989**, *9* (3), 761.

(62) Bergamo, A.; Masi, A.; Jakupec, M. A.; Keppler, B. K.; Sava, G. *Met.-Based Drugs* **2009**, *2009*, 681270.

(63) Groessl, M.; Reisner, E.; Hartinger, C. G.; Eichinger, R.; Semenova, O.; Timerbaev, A. R.; Jakupec, M. A.; Arion, V. B.; Keppler, B. K. *J. Med. Chem.* **2007**, *50* (9), 2185.

(64) Kapitza, S.; Pongratz, M.; Jakupec, M. A.; Heffeter, P.; Berger, W.; Lackinger, L.; Keppler, B. K.; Marian, B. *J. Cancer Res. Clin. Oncol.* **2005**, *131* (2), 101.

(65) Vargiu, A. V.; Robertazzi, A.; Magistrato, A.; Ruggerone, P.; Carloni, P. *J. Phys. Chem. B* **2008**, *112* (14), 4401.

(66) Brindell, M.; Piotrowska, D.; Shoukry, A. A.; Stochel, G.; van Eldik, R. *J. Biol. Inorg. Chem.* **2007**, *12* (6), 809.

(67) Ascone, I.; Messori, L.; Casini, A.; Gabbiani, C.; Balerna, A.; Dell'Unto, F.; Castellano, A. C. *Inorg. Chem.* **2008**, *47* (19), 8629.

(68) Piccioli, F.; Sabatini, S.; Messori, L.; Orioli, P.; Hartinger, C. G.; Keppler, B. K. *J. Inorg. Biochem.* **2004**, *98* (6), 1135.

(69) Pongratz, M.; Schluga, P.; Jakupec, M. A.; Arion, V. B.; Hartinger, C. G.; Allmaier, G. N.; Keppler, B. K. *J. Anal. At. Spectrom.* **2004**, *19* (1), 46.

(70) Sun, H.; Li, H.; Sadler, P. J. *Chem. Rev.* **1999**, *99* (9), 2817.

(71) Malina, J.; Novakova, O.; Keppler, B. K.; Alessio, E.; Brabec, V. *J. Biol. Inorg. Chem.* **2001**, *6* (4), 435.

(72) Gopal, Y.; Konuru, N.; Kondapi, A. K. *Arch. Biochem. Biophys.* **2002**, *401*, 53.

(73) Dyson, P. J.; Sava, G. *Dalton Trans.* **2006**, No. 16, 1929.

(74) Allardyce, C. S.; Dyson, P. J. *J. Cluster Sci.* **2001**, *12* (4), 563.

(75) Rosenberg, E.; Spada, F.; Sugden, K.; Martin, B. *J. Organomet. Chem.* **2003**, *668*, 51.

(76) Therrien, B.; Ang, W. H.; Chérioux, F.; Vieille-Petit, L.; Juillerat-Jeanneret, L.; Süss-Fink, G.; Dyson, P. J. *J. Cluster Sci.* **2007**, *18* (3), 741.

(77) Dickson, N. R.; Jones, S. F.; Burris, H. A.; Ramanathan, R. K.; Weiss, G. J.; Infante, J. R.; Bendell, J. C.; McCulloch, W.; Hoff, Von, D. D. *JOURNAL OF CLINICAL ONCOLOGY* **2011**, *{29}* ({15, S}).

(78) Kapitza, S.; Jakupec, M. A.; Uhl, M.; Keppler, B. K.; Marian, B. *Cancer Letters* **2005**, *226* (2), 115.

(79) Jungwirth, U.; Kowol, C. R.; Keppler, B. K.; Hartinger, C. G.; Berger, W.; Heffeter, P. *Antiox. Redox Signal.* **2011**, *{15}* ({4}), {1085.

(80) Heffeter, P.; Boeck, K.; Atil, B.; Hoda, M. A. R.; Koerner, W.; Bartel, C.; Jungwirth, U.; Keppler, B. K.; Micksche, M.; Berger, W.; Koellensperger, G. *J. Bio. Inorg. Chem.* **2010**, *15* (5), 737.

(81) Heffeter, P.; Atil, B.; Kryeziu, K.; Groza, D.; Koellensperger, G.; Körner, W.; Jungwirth, U.; Mohr, T.; Keppler, Bernhard K; Berger, W. *European Journal of Cancer* **2013**, *49*, 3366.

(82) Penner-Hahn, J. E. *Coord. Chem. Rev.* **2005**, *249*, 161.

(83) Ortega, R.; Devès, G.; Carmona, A. *J. R. Soc. Interface* **2009**, *6* (Suppl. 5), S649.

(84) Pushie, M. J.; Pickering, I. J.; Korbas, M.; Hackett, M. J. *Chem. Rev.* **2014**, *114*, 8499.

(85) Paunesku, T.; Vogt, S.; Maser, J.; Lai, B. *J. Cell. Biochem.* **2006**, *99*, 1489.

(86) Hall, M. D.; Alderden, R. A.; Zhang, M.; Beale, P. J.; Cai, Z.; Lai, B.; Stampfl, A. P. J.; Hambley, T. W. *J. Struct. Bio.* **2006**, *155* (1), 38.

(87) Hall, M. D.; Dillon, C. T.; Zhang, M.; Beale, P.; Cai, Z.; Lai, B.; Stampfl, A. P. J.; Hambley, T. W. *J. Bio. Inorg. Chem.* **2003**, *8* (7), 726.

(88) Alderden, R. A.; Mellor, H. R.; Modok, S.; Hall, M. D.; Sutton, S. R.; Newville, M. G.; Callaghan, R.; Hambley, T. W. *Journal of the American Chemical Society* **2007**, *129* (44), 13400.

(89) Finney, L.; Chishti, Y.; Khare, T.; Giometti, C.; Levina, A.; Lay, P. A.; Vogt, S. *ACS Chem. Biol.* **2010**, *5* (6), 577.

(90) Ascone, I.; Fourme, R.; Hasnain, S.; Hodgson, K. *J. Synchrotron Radiat.* **2005**, *12* (Pt 1), 1.

(91) Verbi, F. M.; Arruda, S. C. C.; Rodriguez, A. P. M.; Pérez, C. A.; Arruda, M. A. Z. *J. Biochem. Biophys. Methods* **2005**, *62* (2), 97.

(92) Aitken, J. B.; Carter, E. A.; Eastgate, H.; Hackett, M. J.; Harris, H. H.; Levina, A.; Lee, Y. C.; Chen, C. I.; Lai, B.; Vogt, S.; Lay, P. A. *Radiat. Phys. Chem.* **2010**, *79*, 176.

(93) Carter, E. A.; Tam, K. K.; Armstrong, R. S.; Lay, P. A. *Biophys. Rev.* **2009**, *1* (2), 95.

(94) Weekley, C. M.; Aitken, J. B.; Vogt, S.; Finney, L. A.; Paterson, D. J.; de Jonge, M. D.; Howard, D. L.; Witting, P. K.; Musgrave, I. F.; Harris, H. H.

Journal of the American Chemical Society **2011**, *133*, 18772.

(95) Vogt, S. *J. Phys. IV France* **2003**, *104*, 635.

(96) Van Espen, P. In *Handbook of X-Ray Spectrometry*; Van Grieken, R. E., Markowicz, A. A., Eds.; CRC Press, 2002; Vol. 29.

(97) Weekley, C. M.; Aitken, J. B.; Vogt, S.; Finney, L. A.; Paterson, D. J.; de Jonge, M. D.; Howard, D. L.; Musgrave, I. F.; Harris, H. H. *Biochemistry* **2011**, *50* (10), 1641.

(98) Carter, E.; Rayner, B.; McLeod, A.; Wu, L. *Mol. Biosyst.* **2010**, *6*, 1316.

(99) Groessl, M.; Zava, O.; Dyson, P. J. *Metallomics* **2011**, *3* (6), 591.

Chapter 5. Summary of outcomes and future directions

This thesis presented a selection of examples where synchrotron-based spectroscopic techniques were used to explore the cellular metallome, focusing on perturbations due to treatment with therapeutic and diagnostic agents. A broad range of cellular models, differing biometal-containing agents as well as combinations with standard laboratory techniques were used to highlight both the unique capabilities of synchrotron-based techniques in addition to their potential to complement pre-existing established techniques.

The biometals of interest were characterized and visualised by X-ray absorption spectroscopy (XAS) and X-ray fluorescence microscopy (XFM) within cellular samples directly. From this data, in addition to the disruptions to the cellular metallome, mode of action information was also obtained for the luminescent rhenium probe and the neuroprotective selenium-based agent.

Firstly, the intracellular fate of a luminescent rhenium(I) tricarbonyl tetrazolato complex probe within 22Rv1 human prostate epithelial carcinoma cells was explored. It was demonstrated that the cellular distribution of the luminescent imaging agent could be determined by monitoring the luminescence from the compound using optical microscopy and then correlated with the cellular distributions of rhenium and iodine contained in the species within the same samples as measured using micro-probe X-ray fluorescence imaging.

Quantitation of cellular elemental contents arising from integrated XRF signals showed that the homeostasis of some biological elements was disrupted by treatment with the Re-I probe and that this may be used to identify subtle impacts of imaging agents on cellular homeostasis. The XRF imaging study also indicated that the distributions of rhenium and iodine were very similar, which indicated that the complex remained intact in the cells after uptake.

A combination of XAS and XFM was employed to investigate the neuroprotective action purported for diphenyl diselenide. This was achieved by treating SH-SY5Y human neurocarcinoma epithelial cells with more water soluble diphenyl diselenide analogues; bis(2-aminodiphenyl)diselenide and bis(2-nitrodiphenyl)diselenide. The XAS and XFM results were then compared to those for the known stroke-mitigation drug Ebselen. Of the two analogues only bis(2-aminodiphenyl)diselenide was

observed to delay oxidative-stress induced cell death in cytotoxicity assays.

The distinct chemistries of the related compounds were traced by the changes in selenium speciation in bulk pellets of treated SH-SY5Y cells detected by X-ray absorption spectroscopy. Further, bis(2-aminophenyl)diselenide, like the known stroke mitigation agent Ebselen, was observed by XFM to penetrate into the nucleus of SH-SY5Y cells while bis(2-nitrophenyl)diselenide was observed to be excluded from the nuclear region. The differences in activity were thus attributed to the varied speciation and localisations of the drugs, or their metabolites, as detected by XAS and XFM.

From these two studies it can be seen that the advantageous, simultaneous collection of metallome and mode of action information can provide a pathway to exploring neurological diseases and disorders, the production of better therapeutic agents, and could be used diagnostically in medicine.

Finally, the anticancer action of NKP-1339, a KP1019 analogue, within A549 human lung adenocarcinoma epithelial cells was investigated. Initially a co-localisation of NKP-1339, or its ruthenium-containing metabolites, with intracellular iron and copper was observed. Subsequent attempts to visualise a mitochondrial compartmentalisation of the NKP-1339 or its ruthenium-based metabolites utilising a combination of optical and synchrotron-based fluorescence microscopy were unsuccessful.

Results appeared to support that NKP-1339 was a KP1019 analogue, with prominent cellular uptake. Furthermore, XFM showed that the two chosen mitochondrial probes; MitoTracker DeepRed and MitoTracker Orange, perturbed homeostasis in different ways. Thereby highlighting the importance of thorough consideration of the effects of probes for future studies, and the need for careful attention towards the controls to understand these probe-based perturbations.

The studies into the Re-I probe and diphenyl diselenide analogues showcased the power of synchrotron-based spectroscopic techniques yielding mode-of-action information as well as visualising the effects of the biometal-containing agents on the intracellular metallome. The study into NKP-1339, while largely unsuccessful, did provide similar information related to the perturbation of the intracellular metallome while not yielding conclusive mode-of-action information.

While access to beam-time at synchrotron facilities remains a limiting factor, it is

expected that the successes of synchrotron-based techniques within the realm of metallomics will aid in standardising the usage of such techniques. However, while the ability to work with and image biometals in hydrated samples is powerful, there is a need to understand the effects of the radiation damage during imaging as well as other limitations of XAS and XFM.

Appendix I – Other Publications

Statement of Authorship

Title of Paper	Simultaneous observation of the metabolism of cisplatin and NAMI-A in human plasma in vitro by SEC-ICP-MS.
Publication Status	☑ Published ☐ Accepted for Publication ☐ Submitted for Publication ☐ Unpublished and Unsubmitted work written in manuscript style
Publication Details	Sooriyaarachchi, M. Wedding, J. L., Harris, H. H., Gailer, J., Simultaneous observation of the metabolism of cisplatin and NAMI-A in human plasma in vitro by SEC-ICP-MS, Journal of Biological Inorganic Chemistry (JBIC) 19 6 (2014), 1049-1053, DOI:10.1007/s00775-014-1102-0

Principal Author

Name of Principal Author (Candidate)	Jason L. Wedding
Contribution to the Paper	Synthesised and characterised NAMI-A for experimentation and assisted with interpretation of data and the development of the manuscript prior to publication.
Overall percentage (%)	25%
Certification:	This paper reports on original research I conducted during the period of my Higher Degree by Research candidature and is not subject to any obligations or contractual agreements with a third party that would constrain its inclusion in this thesis. I am the primary author of this paper.
Signature	[redacted] Date 11/2/2019,

Co-Author Contributions

By signing the Statement of Authorship, each author certifies that:

i. the candidate's stated contribution to the publication is accurate (as detailed above);
ii. permission is granted for the candidate in include the publication in the thesis; and
iii. the sum of all co-author contributions is equal to 100% less the candidate's stated contribution.

Name of Co-Author	Melani Sooriyaarachchi
Contribution to the Paper	contributed to experiment design, carried out analytical experimentation, analysed and interpreted data and contributed to writing and revising manuscript.
Signature	[redacted] Date 18th Jan 2019

Name of Co-Author	Hugh H. Harris
Contribution to the Paper	Supervised the work, assisted with the conception, writing and revision of the manuscript.
Signature	[redacted] Date 11/2/2019

Name of Co-Author	Jurgen Gailer		
Contribution to the Paper	Supervised the work, assisted with the conception, writing and revision of the manuscript, and acted as a corresponding author.		
Signature		Date	18 JAN 2019

J Biol Inorg Chem (2014) 19:1049–1053
DOI 10.1007/s00775-014-1102-0

REPORT

Simultaneous observation of the metabolism of cisplatin and NAMI-A in human plasma in vitro by SEC-ICP-AES

Melani Sooriyaarachchi · Jason L. Wedding · Hugh H. Harris · Jürgen Gailer

Received: 9 August 2013 / Accepted: 21 December 2013 / Published online: 24 January 2014

Abstract Single drug-based cancer therapies are frequently associated with the development of drug resistance. To overcome this problem, combination therapy with two or more anticancer drugs is a promising strategy, but clinical studies are logistically challenging and costly. Intermediary in vitro studies, however, can provide critical insight to decide whether one should proceed to in vivo studies. To this end, cisplatin and the Ru-based anticancer drug NAMI-A were added to human plasma and the size distribution of Pt-containing and Ru-containing entities was determined over a 2 h period. The results revealed a dramatically different rate of plasma protein binding for each drug and/or their hydrolysis products. Both drugs bound to the same apparent plasma proteins, but crucially they did not adversely affect each other's metabolism. Therefore, combination therapy of patients with these metallodrugs should be further assessed in clinical studies in order to systematically develop an effective combination therapy protocol to prevent the resurgence of cancer.

Keywords Cisplatin · NAMI-A · Combination therapy · Plasma · Size-exclusion chromatography

Electronic supplementary material The online version of this article (doi:10.1007/s00775-014-1102-0) contains supplementary material, which is available to authorized users.

M. Sooriyaarachchi · J. Gailer (✉)
Department of Chemistry,
University of Calgary,
2500 University Drive NW, Calgary, AB T2N 1N4, Canada
e-mail: jgailer@ucalgary.ca

J. L. Wedding · H. H. Harris
School of Chemistry and Physics,
The University of Adelaide,
Adelaide, SA 5005, Australia

Although cisplatin (Fig. 1a) is one of the most widely used Pt-based anticancer drugs [1], the Ru-based drug imidazolium *trans*-(dimethyl sulfoxide)(imidazole)tetrachlororuthen(III)ate (also referred to as "new antitumor metastasis inhibitor A" or NAMI-A; Fig. 1b) has only recently entered clinical trials [2, 3]. A major problem that is frequently encountered during cancer treatment with a single drug is the development of resistance [4, 5]. The coadministration of two drugs that target different biochemical pathways has considerable potential to circumvent drug resistance. In addition, combination therapy can also assist in increasing the effectiveness of treatment. Indeed, the treatment of tumor-implanted mice with cisplatin and NAMI-A was twice as effective as treatment with either drug alone [6]. Given that cisplatin and NAMI-A are each administered intravenously to patients (single drug-based therapy) and target different molecular pathways [2, 7, 8], potential problems that may arise during combination therapy are an increased risk to patients or a reduced efficacy compared with when each drug is given alone [9]. Since cisplatin and NAMI-A each interact with plasma proteins [10, 11] and because these interactions critically determine which molecular form of the drug reaches the tumor [12, 13], it is important to assess whether these metal-based drugs may mutually affect their plasma protein binding, thereby reducing their overall efficacy. To this end, it has been reported that combination therapy with the anticancer drugs vincristine and doxorubicin can result in antagonistic effects [14]. Although the competitive plasma protein binding of cisplatin and NAMI-A has been studied in vitro using polyacrylamide gel electrophoresis and laser ablation inductively coupled plasma mass spectrometry (LA-ICP-MS), human serum albumin (HSA) depleted and diluted human plasma was used [6]. In that study, these drugs were added simultaneously and plasma

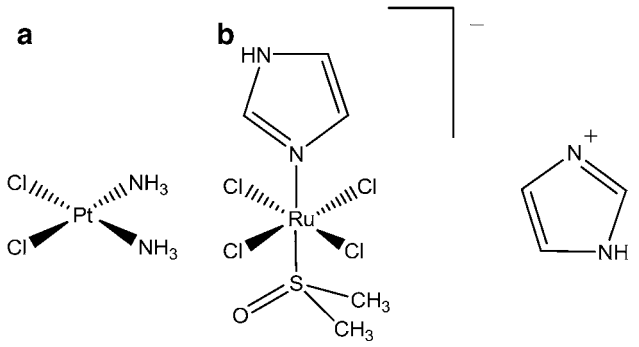

Fig. 1 Molecular structures of **a** cisplatin and **b** new antitumor metastasis inhibitor A (NAMI-A)

was analyzed only 24 h after incubation [6]. Both drugs appeared to bind to the same plasma proteins, and cisplatin did not affect the binding of NAMI-A or vice versa [6]. Considering that combination therapy appears to be a promising strategy to treat cancer patients [10], it is important to probe the effect of different orders of addition of these drugs on the dynamics of their biotransformation immediately after their additions to undiluted human plasma. The results of such an investigation could provide guidance prior to assessing this particular drug combination in clinical studies.

We added therapeutically relevant equimolar doses of cisplatin and NAMI-A to plasma from a healthy human volunteer and analyzed the mixture with a bioanalytical method which can rapidly determine the size distribution of multiple metal species (see electronic supplementary material) [15, 16]. This method is based on the injection of plasma onto a size-exclusion chromatography (SEC) column to separate the plasma proteins. Simultaneous on-line detection of the metal entities in the column effluent is achieved with an inductively coupled plasma atomic emission spectrometer (ICP-AES) [17]. Analysis of plasma by SEC–ICP-AES provides unique insight as it can simultaneously detect the hydrolysis and protein binding of different metal-based drugs as well as their effect on endogenous plasma metalloproteins. Since this method allows the rapid and direct analysis of plasma (in less than 40 min) using phosphate-buffered saline (PBS) as the mobile phase (pH 7.4), it can be ideally applied to visualize dynamic bioinorganic processes which involve metals [15, 18]. To this end, SEC–ICP-AES was used to investigate the metabolism of cisplatin and NAMI-A in human plasma over a 2 h period. Importantly, this approach takes into account the effect that endogenous chloride and carbonate in plasma have on the biotransformation of these complexes.

Cisplatin was added to human plasma (final concentration 130 μM [19]) and the mixture obtained was incubated at 37 °C. The Pt distribution was determined 15 and 65 min later (control experiment), and the results were comparable to those obtained previously [20]. Then, equimolar doses of cisplatin and NAMI-A were added to plasma: cisplatin was added first, followed by NAMI-A (experimental set 1), or cisplatin and NAMI-A were added simultaneously (experimental set 2), or NAMI-A was added first, followed by cisplatin (experimental set 3). The addition of cisplatin and NAMI-A resulted in total peak areas which were identical to those in the respective control experiment (total area for all experiments, Pt 7,479 ± 121, Ru 17,420 ± 438). No effect of the addition of either cisplatin or NAMI-A on the plasma distribution of Cu, Fe, Zn, Ca, or Mg was observed (data not shown). In experimental set 1, plasma was incubated with cisplatin for 1 h and then for an additional 10 min after the addition of NAMI-A. The results (Fig. 2, panel a, solid pink line) revealed that 36.9 % of total Pt was protein-bound (pink-shaded area in Fig. 2), whereas 63.1 % eluted in the form of cisplatin and cisplatin hydrolysis products (these will be collectively referred to as low molecular weight—LMW—Pt species). When this mixture was analyzed again 50 min later (i.e., 1 h after addition of NAMI-A; Fig. 2, panel a, dashed pink line), the protein-bound Pt fraction had increased to 52.1 %, whereas the LMW Pt fraction had decreased to 47.9 %. In experimental set 2, the mixture obtained was analyzed after incubation for 10 min (Fig. 2, panel a, solid red line) and 1 h (Fig. 2, panel a, dashed red line). The results from the 10-min time point revealed a protein-bound Pt fraction of 6.2 % and an LMW Pt fraction of 93.8 %. At the 1-h time point, the protein-bound Pt fraction had increased (30.1 %) and the LMW Pt fraction had decreased (69.9 %). Experimental set 3 involved spiking plasma with NAMI-A, incubation for 1 h, spiking this mixture with cisplatin, a further 10 min incubation, and then analysis. The observed protein-bound Pt fraction was 6.0 % and the LMW Pt fraction was 94.0 % (Fig. 2, panel a, solid brown line). The results obtained at the 1-h time point (Fig. 2, panel a, dashed brown line) revealed that 27.8 % of total Pt was protein-bound, whereas only 72.2 % remained as LMW Pt species.

When plasma was spiked with NAMI-A only and analyzed 10 min and 1 h later, the Ru distribution was essentially the same as that observed for all three experimental sets (Fig. 2, panel a). Although approximately 92.5 % of Ru was protein-bound (to the same apparent plasma proteins as cisplatin; Fig. 2, panel a), approximately 7.5 % eluted as one apparent LMW Ru species. NAMI-A-derived Ru species are known to have a high affinity for plasma proteins, such as HSA [7, 21, 22] and transferrin [22]. The minor decrease in the intensity of the single LMW Ru species between 10 min and 1 h (retention time t_r ~1,240 s; Fig. 2, panel b) can be rationalized in terms of its binding to plasma proteins. Since these results cannot be attributed to the reduction of Ru(III) [7, 23, 24],

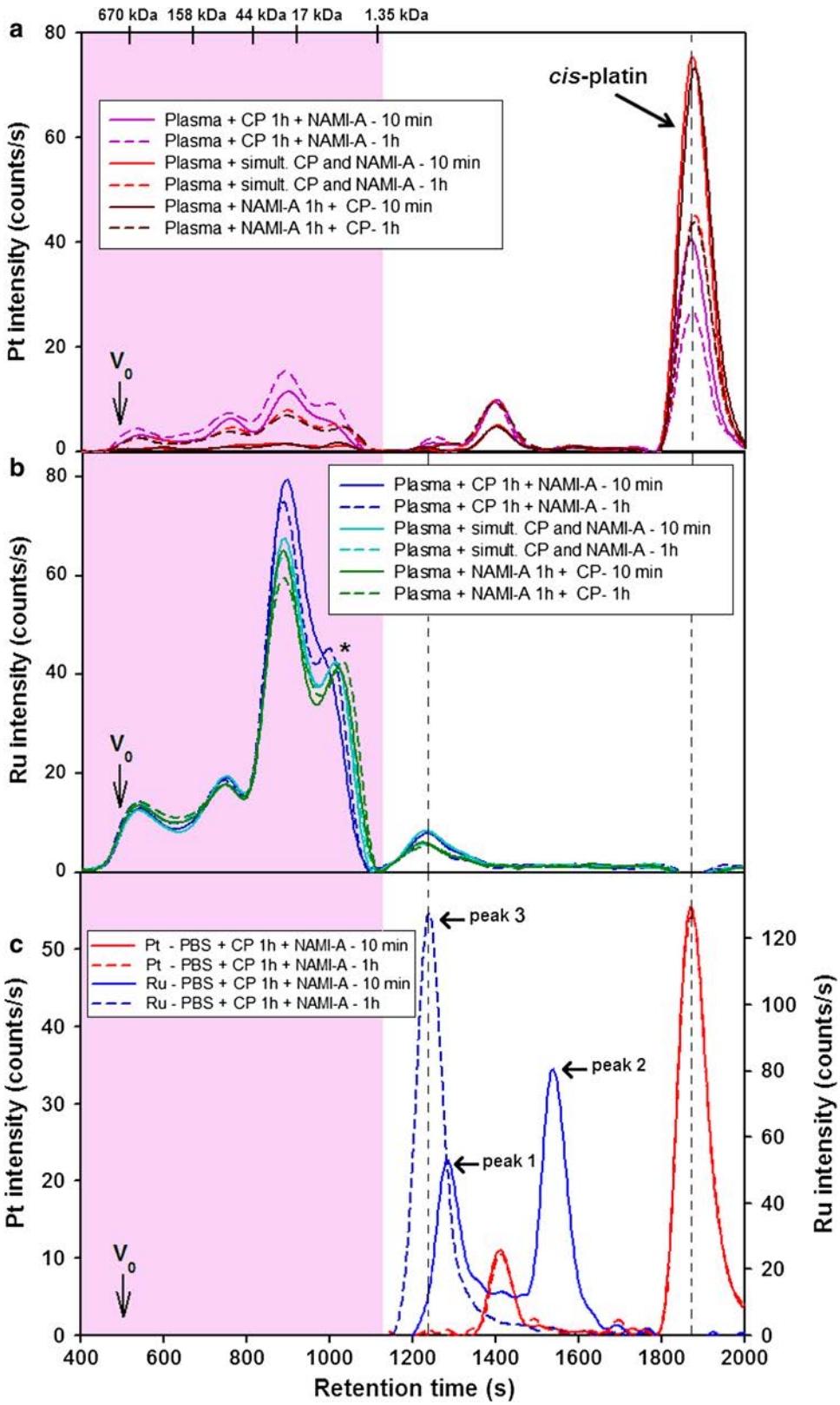

Fig. 2 Representative size-exclusion chromatography—inductively coupled plasma atomic emission spectrometry (SEC-ICP-AES) derived Pt-specific (**a**) and Ru-specific (**b**) chromatograms obtained after the addition of cisplatin (CP) and NAMI-A in different sequences to human plasma and to phosphate-buffered saline (PBS-buffer) (**c**), 10 min and 1 h after incubation at 37 °C. Equimolar plasma concentrations of CP or NAMI-A were used (130 μM). The stationary phase was a Superdex 200 10/300 GL (30 × 1.0 cm inner diameter, 13 μm particle size) SEC column at 22 °C, the mobile phase was PBS (0.15 M, pH 7.4), the flow rate was 1.0 mL/min, the injection volume was 500 μL, and ICP-AES detection at 214.423 nm (Pt) and 240.272 nm (Ru). The retention times of the molecular markers are depicted on top. The *pink-shaded area* indicates the protein-bound fraction. The shoulder (*asterisk*) on the peak that gradually developed was caused by a 2-mm gap that formed on the column head owing to the viscosity of human plasma, similarly to previous observations [30]. (*simult.* simultaneous)

our findings demonstrate that the binding of NAMI-A derived hydrolysis products to plasma proteins is essentially complete within 10 min and is not influenced by cisplatin, whatsoever. The fact that each drug-derived metal species appeared to bind to the same plasma proteins can be rationalized in terms of their different binding sites

on the same plasma proteins [8, 25, 26], which in turn may be attributed to the different Lewis acidities of Pt(II) and Ru(III) [2, 23]. The HSA concentration in plasma was approximately 660 μM and the transferrin concentration was approximately 35 μM. Since the concentration of pharmacologically relevant doses of each drug added to plasma was 130 μM (260 μM in total), the excess of HSA precludes a competitive interaction of these drugs for protein binding sites as a mechanism of action. One may envision, however, that in principle these two metal-based drugs may be metabolized in plasma (which contains approximately 103 mM chloride [27]) to species that form a halide-bridged complex with Pt and Ru similar to a synthetic complex that has been reported previously [28]. Therefore, our studies represent an in vitro approach to better understand the interplay between drug metabolism and drug transport to elucidate drug–drug interactions [29] before more expensive in vivo studies with patients are initiated [30].

To rationalize the results that were obtained with plasma, cisplatin was added to PBS-buffer, the mixture was incubated for 1 h, and then NAMI-A was added. Subsequent analysis 10 min and 1 h later revealed that a large fraction of Pt (Fig. 2, panel c) was present as the parent drug (see the dotted line pertaining to cisplatin in Fig. 2) and that a Pt-containing hydrolysis product was detected in both PBS-buffer and plasma [18]. The Ru-specific chromatogram that was obtained at the 10 min time point revealed two peaks (peak 1, $t_r \sim 1{,}284$ s, and peak 2, $t_r \sim 1{,}537$ s; Fig. 2, panel c) which were not observed in plasma (Fig. 2, panel b). We tentatively assign peak 2 as NAMI-A and peak 1 as a primary hydrolysis product (comparatively much less intense Ru peaks were also detected in between). At the 1 h time point, only one Ru peak (peak 3, $t_r \sim 1{,}240$ s) was detected, and this had a retention time similar to that of the LMW Ru peak in plasma (see the dotted line pertaining to Ru species in Fig. 2). On the basis of the shorter retention time of this peak compared with Ru peak 1 (observed at the 10 min time point), peak 3 likely corresponds to a secondary hydrolysis product of NAMI-A. These results are in accord with previous observations where NAMI-A underwent stepwise hydrolysis via ligand exchange of Cl^- and/or dimethyl sulfoxide with water molecules [7, 21].

The results that were obtained with PBS-buffer are useful to interpret the results obtained after both metal-based drugs had been added to plasma. The Pt results corresponding to the LMW elution range were qualitatively similar between plasma and PBS-buffer (Fig. 2, panel a vs panel c), suggesting a closely related solution chemistry. With regard to NAMI-A, essentially all Ru was protein-bound within 10 min regardless of the presence of cisplatin and the order of addition. In contrast to cisplatin, only one residual LMW Ru peak was observed in plasma, whereas more than three Ru peaks were observed in PBS-buffer (of these, peak 3 was also present in plasma). The fact that Ru peak 2 (and potentially peak 1) was not detected in plasma implies that the protein binding of NAMI-A-derived Ru species is essentially complete within 10 min, whereas cisplatin hydrolyses in plasma at a comparatively slower rate. The data that were obtained 10 min and 1 h after incubation revealed that the fraction of Ru which eluted as peak 3 was still present in plasma within 2 h of addition of NAMI-A, indicating that this Ru species does not bind to proteins, whereas the Ru species corresponding to peaks 1 and 2 appear to bind. This implies that an equilibrium partitioning of LMW Ru species and protein-bound fractions is established rather rapidly. In addition, the presence of Ru peak 3 in plasma at 10 min and its absence in the PBS-buffer experiment at the corresponding time point indicate that its generation is enhanced by a component of plasma that is not present in PBS-buffer.

Conclusions

Using a metallomics tool allowed us to simultaneously observe the metabolic fate of two metal-based anticancer drugs, namely, cisplatin and NAMI-A, after their addition to human plasma in vitro. A previous investigation with these particular metal-based drugs and using tumor-implanted mice as a model clearly demonstrated that combination therapy is effective (approximately 60 % decrease in lung metastasis) compared to when each drug is administered alone (approximately 30 % decrease in lung metastasis) [6]. The in vitro results of that investigation revealed no adverse effect of one drug on the plasma protein binding of the other 24 h after both metal-based drugs had been simultaneously added to HSA-depleted and diluted human plasma [6]. Using a recently developed metallomics approach, we extended these studies using whole human plasma to assess the effect of the order of addition of cisplatin and NAMI-A on their mutual metabolism and plasma protein binding over a 2 h period. In addition, we complemented these experiments with studies using PBS-buffer. No mutual perturbation of the metabolism of these metal-based drugs was detected in plasma (Fig. 2, panels a and b) regardless of their order of addition. The results obtained with PBS-buffer provided critical insight to rationalize the dynamic solution chemistry of cisplatin and NAMI-A in plasma. Taken together, these data along with the demonstrated efficacy of this anticancer drug combination in mice [6] support clinical studies to further explore combination therapy with these metal-based drugs.

Acknowledgments M.S. is a Fellow of the Canadian Institutes of Health Research Training Grant in Health Research Using Synchrotron Techniques (CIHR-THRUST). Isolde Seiden Long is gratefully

acknowledged for assisting with the analysis of the plasma sample for HSA and transferrin concentrations. This work was supported in part by the Australian Research Council (DP0985807-QEII and DP0984722 to H.H.H.). We thank Aviva Levina and two anonymous reviewers for helpful discussions.

References

1. Wang D, Lippard S (2005) Nat Rev Drug Discov 4:307–320
2. Page S (2012) Educ Chem 49:26–29
3. Rademaker-Lakhai JM, Bongard D, Pluim D, Beijnen JH, Schellens JHM (2004) Clin Cancer Res 10:3717–3727
4. Kondagunta GV, Bacik J, Donadio A, Bajorin D, Marion S, Sheinfeld J, Bosl GJ, Motzer RJ (2005) J Clin Oncol 23:6549–6555
5. Soulié P, Garrino C, Bensmaïne MA, Bekradda M, Brain E, Di Palma M, Goupil A, Misset JL, Cvitkovic E (1999) J Cancer Res Clin 125:707–711
6. Khalaila I, Bergamo A, Bussy F, Sava G, Dyson PJ (2006) Int J Oncol 29:261–268
7. Webb MI, Walsby CJ (2011) Dalton Trans 40:1322–1331
8. Levina A, Mitra A, Lay PA (2009) Metallomics 1:458–470
9. Vallner JJ (1977) J Pharm Sci 66:447–465
10. Kaiser J (2011) Science 331:1542–1545
11. Martínez E, Milinkovic A, de Lazzari E, Ravasi G, José LB, Larrousse M, Mallolas J, García F, Miró JM, Gatell JM (2004) Lancet 364:65–67
12. Casini A, Reedijk J (2012) Chem Sci 3:3135–3144
13. Timerbaev AR, Hartinger CG, Aleksenko SS, Keppler BK (2006) Chem Rev 106:2224–2248
14. Abraham SA, McKenzie C, Masin D, Ng R, Harasym TO, Mayer LD, Bally MB (2004) Clin Can Res 10:728–738
15. Jahromi EZ, Gailer J (2012) Metallomics 4:995–1003
16. Sooriyaarachchi M, Gailer J (2010) Dalton Trans 39:7466–7473
17. Manley SA, Byrns S, Lyon AW, Brown P, Gailer J (2009) J Biol Inorg Chem 14:61–74
18. Sooriyaarachchi M, Narendran A, Gailer J (2011) Metallomics 3:49–55
19. Go RS, Adjei AA (1999) J Clin Oncol 17:409–409
20. Sooriyaarachchi M, Narendran A, Gailer J (2012) Metallomics 4:960–967
21. Brindell M, Stawoska I, Supel J, Skoczowski A, Stochel G, van Eldik R (2008) J Biol Inorg Chem 13:909–918
22. Bergamo A, Messori L, Piccioli F, Cocchietto M, Sava G (2003) Invest New Drugs 21:401–411
23. Levina A, Aitken JB, Gwee1 YY, Lim ZJ, Liu M, Singharay AM, Wong PF, Lay PA (2013) Chem Eur J 19:3609–3619
24. Hummer AA, Heffeter P, Berger W, Filipits M, Batchelor D, Büchel GE, Jakupec MA, Keppler BK, Rompel A (2013) J Med Chem 56:1182–1196
25. Ivanov AI, Christodoulou J, Parkinson JA, Barnham KJ, Tucker A, Woodrow J, Sadler PJ (1998) J Biol Inorg Chem 273:14721–14730
26. Liu M, Lim ZJ, Gwee YY, Levina A, Lay PA (2010) Angew Chem Int Ed 49:1661–1664
27. Sherman S, Lippard S (1987) Chem Rev 87:1153–1181
28. Severin K, Polborn K, Beck W (1995) Inorg Chim Acta 240:339–346
29. König J, Müller F, Fromm MF (2013) Pharmacol Rev 65:944–966
30. Tuncel S, Dumoulin F, Gailer J, Sooriyaarachchi M, Atilla D, Durmuş M, Bouchu D, Savoie H, Boyle RW, Ahsen V (2011) Dalton Trans 40:4067–4079
31. Mestroni G, Alessio E, Sava G (1998) Patent application WO 1998/000431 A1